國 立 交 通 大 學

機 械 工 程 學 系

碩 士 論 文

垂直圓柱容器中空氣經由多孔板衝擊至一加熱圓盤之

混合對流渦流結構之研究

Experimental Study of Mixed Convective Vortex Flow in an Air Flow Moving through a Showerhead and Impinging onto a Heated Disk in a Vertical Cylindrical Chamber

研 究 生 : 汪 書 磊

指 導 老 師: 林 清 發 博 士

中 華 民 國 九 十 八 年 六 月

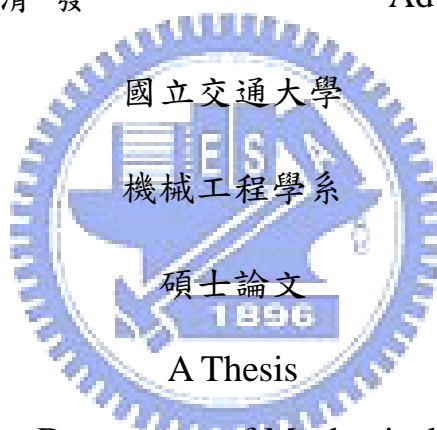垂直圓柱容器中空氣經由多孔板衝擊至一加熱圓盤之混和

對流渦流結構之研究

Experimental Study of Mixed Convective Vortex Flow in an Air Flow

Moving through a showerhead and Impinging onto a Heated Disk in

a Vertical Cylindrical Chamber

研 究 生：汪 書 磊　　　　　　Student：Shu-Lei Wang

指導教授：林 清 發　　　　　　Advisor：Tsing-Fa Lin

國 立 交 通 大 學

機 械 工 程 學 系

碩 士 論 文

A Thesis

Submitted to Department of Mechanical Engineering

Collage of Engineering

National Chiao Tung University

In Partial Fulfillment of the Requirements

For the degree of

Master of Science

In

Mechanical Engineering

June 2009

Hsinchu, Taiwan, Republic of China

中 華 民 國 九 十 八 年 六 月

誌　謝

　　時光飛逝，回首在新竹這兩年來的點點滴滴，交大這充滿學術氣息的環境下似乎讓我在知識上成長茁壯許多。本論文之所以可以順利完成，首先要感謝的是指導老師　林清發教授嚴謹及殷切的指導，使學生能培養出獨立思考、釐清並自行解決問題的能力；更在學生撰寫論文時，不辭辛勞逐字斧正文稿，在此獻上最高謝意。在研究所期間，要特別感謝張文瑞、謝汎鈞及廖永明學長在實驗設備設計、架設上的協助指導，並且在生活及課業上給予建議，使我受益匪淺，謝謝您們。

　　文慶、譯徵這群不只是求學中的同學，更是生活上的好朋友。研究所之所以能在緊湊忙碌又充滿歡樂中的氣氛中度過，即是靠這些同學兼好友的夥伴們相互協助幫忙，令我永生難忘。另外也要感謝　建安、象麟、宏嘉、書豪、俊州等一群努力的學長學弟幫忙及合作，希望你們能繼續保持實驗室優良傳統，並帶著實驗室進步。

　　最後更要感謝父母及家人對於我無怨無悔付出及支持，使我可以無後顧之憂的專注於研究，並且可無憂無慮過求學生活。並特別要感謝室友瑞毅、好友古必、佳芳、邱哥、蘇哥、蛙王、老王、穎志、阿軒、阿棒、文錚、胖子、陳老師、長青的陪伴，生活最精采的部分是你們陪我渡過，不管在課業上或生活上的關心與支持使我有勇氣面對一切的困難挑戰。能與你們相處是我這輩子最大的幸福。

最後，僅以本文獻給我所關心的人和所有關心我的人。

<div align="right">

書磊 謹致

2009/6/27　于風城交大

</div>

垂直圓柱容器中空氣經由多孔板衝擊至一加熱圓盤

之混合對流渦流結構之研究

研究生：汪 書 磊　　　　指導老師：林 清 發 博士

國立交通大學　　機械工程學系

摘　　要

　　本篇論文利用實驗流場觀測方法探討在垂直圓柱容器中空氣經由多孔板衝擊至一加熱圓盤穩態及非穩態渦流結構之流場特性進行研究。主要的目的是藉由多孔氣流的效應來降低在圓柱中因慣性力所造成的渦流結構，並闡釋多孔板放入入口處所造成的效應對於穩態及暫態過程中熱浮力驅動之渦流結構之影響以及探討慣性力渦流結構出現的機制。另外，熱浮力所造成的不穩定現象也一併討論說明。本實驗研究之操作範圍分別是：噴流至圓盤的距離 20～40 mm，多孔板的直徑固定為 76.2 mm，流量變化 0～5.0 slpm，加熱圓盤與入口冷空氣間的溫度差範圍 0～25.0℃，整體的噴流雷諾數變化為 0～89，所相對的噴流雷諾數變化為 0～28，相對於雷利數 0～150,325。

　　從流場可視化可以很清楚地發現慣性力所造成的第一類和第二類渦流結構均有被抑制並且出現的機制也延後發生，原因是多孔板所造成的效果。當 ΔT ≠ 0 時，慣性力所造成的第二類渦流並無出現且熱浮力所驅動的渦流結構會一直存在流場中。另外，針對不同高度(H = 20.0, 30.0 及 40.0mm)我們分別定義出四種型態的流譜型態：(1) 理想流譜，(2) 熱浮力所主導的流譜，(3) 慣性力所主導的流譜以及(4) 慣性力和熱浮力共同主導的流譜，並且界定不穩定的流場型態以及出現的範圍。其中，理想流譜僅出現在完全沒有加熱的情況且低流量。

除此之外，本研究還比較有和沒有加裝多孔板對於流場型態有多大的影響。從相關的流場圖分析結果得知，加裝多孔板確實能夠有效地抑制慣性力所產生的渦流結構在圓柱型腔體內出現。最後，我們將流場轉變以及熱浮力造成不穩定性的範圍以實驗結果做分析，求得經驗公式。

Experimental Study of Mixed Convective Vortex Flow in an Air Flow Moving through a showerhead and Impinging onto a Heated Disk in a Vertical Cylindrical Chamber

Student: Shu-Lei Wang   **Advisor: Prof. Tsing-Fa Lin**

Department of Mechanical Engineering

National Chiao Tung University

ABSTRACT

An experimental flow visualization is carried out in the present study to investigate how the installation of a showerhead at the jet injection nozzle affects the vortex flow resulting from multiple air jets impinging onto a heated horizontal circular disk confined in a vertical cylindrical chamber. The study is motivated by the fact that the multiple air jets of small cross section are less likely to induce inertia-driven vortex flow. Particular attention is paid to examining the effects of the showerhead installation on the characteristics of steady and time-dependent buoyancy-driven vortex flows. Besides, the onset of the inertia-driven vortex flow and the instability of the buoyancy-driven vortex flow will be inspected. In the present experiment three jet-disk separation distances are considered with H = 20.0, 30.0, and 40.0 mm for a fixed injection nozzle diameter (D_n = 76.2 mm). The jet flow rate is varied from 0 to 5.0 slpm (standard liter per minute) for the overall jet Reynolds number Re_n ranging from 0 to 89 and the jet Reynolds number Re_j ranging from 0 to
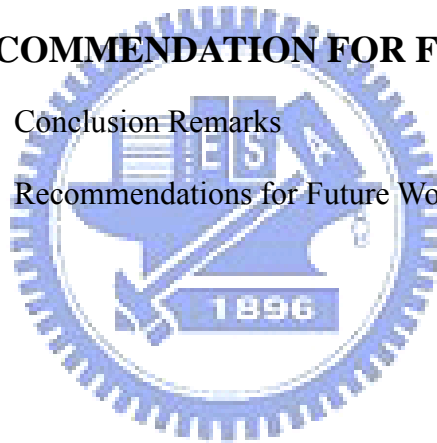
28. The temperature difference between the disk and the air injected into the chamber is varied from 0 to 25.0℃ for the Rayleigh number Ra ranging from 0 to 150,325.

The results from the flow visualization clearly show the significant effects of the showerhead on the critical Re_j for the onset of the primary and secondary inertia-driven rolls. Specifically, the onsets of the inertia-driven rolls are delayed to higher Re_j through the installation of the showerhead. Besides, the secondary inertia-driven roll does not appear in the chamber with $\Delta T \neq 0$ for $HD_n = 0.26$ to 0.52. Moreover, we identify four different types of vortex flow (plug flow, buoyancy-driven vortex flow, inertia-driven vortex flow, and mixed flow) and delineate temporal state of the flow when HD_n is varied from 0.26 to 0.52. Flow regime maps are presented. The plug flow only occurs at lower Re_j for the disk unheated (Ra = 0). The buoyancy roll always appears for $HD_n = 0.39$ and 0.52 even at a small ΔT of 1℃. Besides, we compared the vortex flows in the chamber with and without the showerhead installation. The result shows that the showerhead installation at the injection nozzle can effectively suppress the inertia-driven vortex rolls. Finally, empirical correlations are proposed for the boundaries separating the buoyancy-driven and mixed vortex flows and for the onset conditions of the vortex flow instabilities for HD_n.

TABLE OF CONTENTS

LIST OF TABLES

LIST OF FIGURES

NONMENCLATURE

D_j	Average diameter of holes in showerhead (mm)
D_n	Diameter of jet at the large showerhead exit (mm)
D_w	Diameter of disk (mm)
Gr	Grashof number, $g\beta\Delta TH^3/\nu^2$
g	Gravitational acceleration (m/s^2)
H	Jet-to-disk separation distance (mm)
HD_n	Ratio of the jet-disk separation distance to the jet diameter, H/ D_n
N	The number of the holes in the showerhead
Q_j	The total jet flow rate (Standard Liter per Minute, slpm)
r,θ,z	Dimensional coordinates in cylindrical coordinate system
R,Θ,Z	Dimensionless coordinates $r/R_c, \theta/360°, z/H$
Ra	Rayleigh number, $g\beta\Delta TH^3/\alpha\nu$
R_c	Radius of cylindrical chamber (mm)
Re_n	Overall jet Reynolds number, $V_n D_n/\nu$
Re_j	Jet Reynolds number, $V_j D_j/\nu$
T_a	Ambient Temperature (℃)
T_h	Temperature of the heated disk (℃)
T_j	Temperature of jet at the large showerhead exit (℃)
t	Time (sec)
V_n	the average inlet speed of the air flow without the showerhead installation (m/s)
V_j	the average speed of the air jets at the holes in the showerhead (m/s)

Greek symbols

α   Thermal diffusivity (m^2/s)

β   Thermal expansion coefficient (1/K)

ΔT   Temperature difference between the heated disk and the air injected

               into the chamber (℃)

ν   Kinematic viscosity (m^2/s)

ρ Density (kg/m^3)

μ   Dynamic viscosity (kg/ms)

k   Thermal conductivity (W/m℃)

CHAPTER 1

IMTRODUCTION

1.1 Motivation of the study

Due to their superior heat transfer capability, impinging jets have been found in many technological applications such as heating, cooling, and drying of surfaces. For example, they are employed in paper and textile industries, electronics cooling of portable computers [1] and turbine blades, drying of veneer, thermal treatment of materials, etc. In steel or gas turbine industries impinging jets are often used to cool down the products after rolling. In some circumstances drying rate may be increased by an order of magnitude compared to contact drying. In laser or plasma cutting processes, the application of jet impingement cooling can reduce thermal deformation of products. Recently, impinging jets are widely employed in MOCVD (Metal Organic Chemical Vapor Deposition) growth of thin crystal films for solar cells [2].

It is well known that in the MOCVD processes the jet is no longer at a high speed. At low jet speed the buoyancy generated by the heated wafer can be relatively high compared with the jet inertia and the buoyancy driven flow recirculations tend to appear [3]. Particularly, the flow recirculations in MOCVD processing chamber have detrimental effects on the film properties. In order to obtain high quality solar cells, the flow in the growth processes of the thin films needs to be stable and does not contain any vortices. Thus the understanding and suppression of the inertia- and buoyancy-driven flow recirculations, which are normally in the form of vortex rolls, in the impinging jet flow are rather important in the thin crystal film growth. Apparently, these vortex structures in the MOCVD reactor are mainly affected by the jet inertia, the buoyancy force due to the heated wafer, and pressure gradient

1

associated with the disk rotation, along with the geometry of the chamber including the nozzle diameter, nozzle-to-wafer distance, wafer and chamber diameters. According to the prevailing flow patterns, Biber et al. [4] identified three distinct flow regimes in the vertical MOCVD processing chamber: (1) plug flow, where the gas flows smoothly over the substrate without any recirculation in the chamber, (2) buoyancy-induced flow, where the buoyancy force associated with the heated substrate induces upward flow and recirculation of the gas, and (3) rotation-induced flow, where a toroidal vortex forms near the chamber wall close to the upper disk surface (Fig. 1.1). Obviously, the plug flow is preferred in the growth of thin crystal film for solar cells in a vertical MOCVD reactor.

Attention is paid in the present study to exploring the possible vortex flow structures in a vertical MOCVD processing chamber. More specifically, the possible suppression of the vortex flow by placing a showerhead at the jet injection nozzle will be investigated.
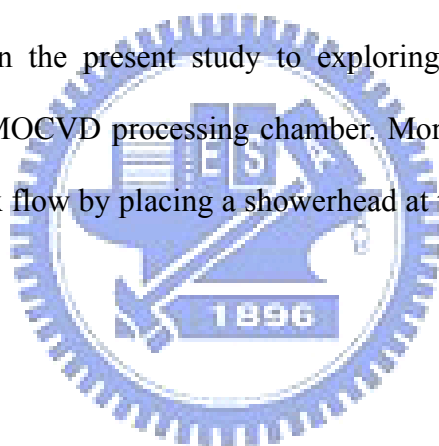
1.2 Literature Review

Interest in exploring the characteristics of the flow and heat transfer associated with impinging jet applies to different kinds of domain in the past through experimental measurement and numerical simulation. Particularly, most of the studies focus on quantifying the highly efficient heat transfer associated with the high speed impinging jets impacted on the heated plate and the jets considered possess a much higher inertia force than the buoyancy force generated by the temperature nonuniformity in the flow. According to the flow characteristics of a free jet, McNaughton and Sinclair [5] proposed four main types of jet in their experimental

2

study and classified the jet by its Reynolds number Re_j: (1) the dissipated-laminar jet for $Re_j < 300$, (2) fully laminar jet for $300 < Re_j < 1000$, (3) semi-turbulent jet for $1000 < Re_j < 3000$, and (4) fully turbulent jet for $Re_j > 3000$. Moreover, the flow structure of a jet impinging onto a surface can be subdivided into three characteristic regions according to Incropera [6] shown in Fig 1.2.: (1) the free jet region, (2) the impingement flow region, and (3) the wall jet region. In the free jet region, the shear-driven interaction of the exiting jet and ambient produces entrainment of mass, momentum, and energy. Near the injection nozzle the jet flow mainly moves in the axial direction and is not affected to a noticeable degree by the presence of the impingement surface. The impingement zone is characterized by a stagnation region and the turning of the jet to the radial direction, which affects transition of the wall jet further downstream. The wall jet region is in the downstream of the stagnation region but near the target plate in which the transverse velocity rises rapidly to a maximum near the wall and then falls at greater distance from the wall. More complete information on various aspects of the flow and heat transfer associated with the impinging jets can be found from the critical reviews by Polat et al. [7], Jambunathan et al. [8], and Viskanta [9].

In order to explore the detailed vortex flow structure, Behbahani et al. [10] visualized the coherent structure in an impinging circular air jet. Later Popiel and Trass [11] observed the detailed flow behavior of turbulent free and impinging round jets, showing the toroidal vortex initiation, vortex pairing, and fluid entrainment processes. They pointed out that the development of these large-scale vortex structures considerably enhanced the entrainment rate and mixing processes. Fitzgerald and Garimella [12] and Morris et al. [13 & 14] used numerical simulation and flow visualization to investigate the vortex flow characteristics for a liquid

impinging jet, which were found to be influenced by the jet Reynolds number Re_j and jet-disk separation distance H. The center of the inertia driven vortex roll was found to move away from jet axis at increasing Re_j and H. Recently, the vortex flow structures resulting from a low speed gas jet impinging onto a heated horizontal disk confined in a vertical cylindrical chamber at low Re_j were visualized by Hsieh et al. [15]. They showed that the gas flow recirculation was typically in the form of three circular vortex rolls including a primary vortex roll around the jet, a secondary vortex roll in the middle region and a buoyancy-induced vortex roll in the outer zone of the chamber. The inner and middle vortex rolls are respectively driven by the jet inertia and the viscous shear due to the nonuniform velocity distribution in the jet and are stronger and bigger at a high Re_j. The secondary inertia-driven vortex roll only appears at certain high Re_j and is much smaller and weaker than the primary inertia-driven vortex roll. The buoyancy driven outer vortex roll results from the temperature difference between the heated disk and inlet gas and is important at high buoyancy-to-inertia ratio. In addition to the appearance of vortices, the effects of the jet Reynolds number and jet-disk separation distance on the locations of the centers of the primary and secondary vortex rolls were investigated by Law and Masliyah [16]. Details on the size and locations of the inertia-driven primary and secondary vortex rolls affected by the jet Reynolds and Richardson numbers for a laminar confined slot-jet were examined by Sahoo and Sharif [17]. Moreover, the effects of the jet-disk separation distance on the vortex flow patterns were investigated by Hsieh and Lin [18] for $HD_j \leq 3$ where $HD_j = H/D_j$. They reported the data for the size and onset of the inertia- and buoyancy-driven vortex rolls affected by HD_j. Moreover, the critical condition for the onset of the inertia-driven time dependent flow for the unheated disk was also provided.

4

For a confined laminar slot impinging jet the critical jet Reynolds number for the onset of unsteady flow was numerically shown to be between 585 and 610 by Chiriac and Ortega [19]. Santen et al. [20 & 21] indicated that the onset of thermal instability became earlier at increasing buoyancy-to-inertia ratio. As the buoyancy-to-inertia ratio exceeds certain critical level, the buoyancy-driven secondary flow is so strong to cause the flow transition from a steady to an unsteady state. Chung and Luo [22] suggested that unsteady heat transfer at an impinging jet was strongly dependent on the vortex dynamics. Moreover, a laminar impinging jet with small pulsation at the outlet of the jet was numerically simulated by Poh et al. [23]. They showed that in a periodic cycle the large vortice appearing in the minimum velocity state was broken into two smaller vortices when the flow was accelerated sinusodially to arrive at the maximum velocity state, after which the two vortices merged again when the flow was decelerated back to the minimum velocity state. Hsieh et al. [24] and Law and Masliyah [25] found that the impinging jet flow structure was significantly influenced by the chamber geometry. Specifically, Hsieh et al.[24] revealed that inclining the chamber top could effectively suppress the buoyancy-induced vortex flow at low buoyancy-to-inertia ratios and the unsteady vortex flow oscillation could be completely stabilized even at high buoyancy-to-inertia ratios.

Heat transfer in the turbulent impinging jet was numerically predicted by Colucci and Viskanta [26], Gao and Ewing [27], and Narayanan et al. [28]. Colucci and Viskanta [26] reported the effects of a hyperbolic nozzle outlet on the local heat transfer. The numerical prediction from Gao and Ewing [27] revealed that the upper plate confinement did not exhibit noticeable effect on the heat transfer for the ratio of the jet-disk separation distance to the jet diameter greater than 1. Angioletti et al. [29] conducted an experiment to examine transitional unconfined impinging jets for 1,000

$<$ Re_j $<$ 4,000. Their results showed that the local heat transfer was strongly influenced by the impinging jet structures. Specifically, the maximum heat transfer coefficient offset was noted to result from the induced large-scale toroidal vortices on the plate. Furthermore, heat transfer in a confined impinging slot jet covering the laminar and turbulent regimes was studied by Park et al. [30]. Lin [31] provided the measured data for the heat transfer coefficient varied with the jet Reynolds number and the jet-disk separation distance in the laminar and transitional impinging jets.

Flow structure and heat transfer in an array of multiple impinging jets have received considerable attention in the past [32-37]. The interference between the adjacent jets and the upwash-fountain flow may become significant in certain ranges of the jet-jet spacing and jet-plate separation distance. Normally, these effects are small for a short jet-to-plate distance [32 & 37]. Besides, the convective heat transfer from the plate to the jet can be more uniform by a suitable choice of the parameters associated with the jet array.

Recently, chemical vapor deposition (CVD) has become the most widely used method to deposit thin crystal film. It have been known that the desirable features of the CVD processes include thickness uniformity, high deposition rate, control over the stoichiometry of the deposited material, and sharp interface. Thus flow in CVD chamber must be free from any vortex structure to avoid destroying the thin film uniformity. For this reason, it is important to suppress vortex flow in the CVD chamber. It is well known that in CVD processes the buoyancy-driven vortex flow can be suppressed by increasing the inlet flow rate, rotating the susceptor, reducing the chamber pressure and modifying the reactor shape. Hsieh [38] indicates that the centrifugal force of a rotating disk can reduce the bouyancy effect. Santen et al. [39 & 40] numerically examined the symmetry breaking of the flow owing to the

6

buoyancy effects in cold-wall stagnation flow CVD reactors and indicated that for the aspect ratio (height/diameter) of the reactor larger than one, stable non-axisymmetric flows could occur. Relatively high flow speed and/or rotation rate of the wafer were noted to be able to suppress the asymmetric flows. They also proposed that the symmetry-breaking of the flow can be suppressed by reducing the aspect ratio of the reactor. Soong et al. [41] presented the effects of gas flow, rotation of susceptor and natural convection on flow patterns in a model MOCVD reactor and found that the chaotic flow at a high buoyancy-to-inertia ratio could be stabilized by the susceptor rotation. They [42] further located the boundaries for the three flow regimes: buoyancy-, inertia- and rotation-dominated flows. Vanka and his colleagues [43-45] conducted a series of computational studies to explain the effects of the reactor pressure, substrate rotation rate, inlet flow rate, and reactor thermal boundary conditions on the flow in impinging jet CVD reactor. The buoyancy force is opposed by the inlet jet momentum and the force owing to substrate rotation. They were able to create a uniform mass transfer rate over the wafer. Fotiadis et al.[46 & 47] examined the effects of the operating parameters, reactor geometry, heat transfer characteristics on the flow patterns and deposition rate uniformity by using detailed transport models for vertical MOCVD reactors. They observed two types of recirculation cells in the vertical reactors: (1) natural convection cells driven by unstable density gradients due to large temperature gradients and (2) cells due to flow separation associated with sudden expansion in the flow cross-sectional area. The results demonstrated that natural convection effects could be reduced and thus the uniformity could be improved by increasing the inlet flow rate, rotating the susceptor, reducing the pressure, inverting the reactor, shortening the distance between inlet and susceptor, introducing baffles, and reshaping the reactor wall. To procure optimal

7

design of MOCVD reactor, Gadgil [48 & 49] installed a capillary plug inlet which not only removes the toroid, but acts as an ideal gas distributor and creates an axially umiform velocity profile. Phillips et al. [50] probed into effect of showerhead configuration on plasma enhanced chemical vapor deposition (PECVD) by three showerhead geometries: radial – the holes are arranged in a radial array, square – the pitches of the holes are all equal, and asymmetrical – the holes does not have regular arrangement. They found that the radial showerhead could provide the most homogeneous crystal film.

1.3 Objective and Scope of Present Study

The above literature review clearly reveals that some vortex rolls can be induced by the inertia and buoyancy forces in a mixed convective low speed gas jet impinging onto a heated wafer confined in a vertical MOCVD chamber. These vortex rolls become unsteady at high buoyancy-to-inertia ratios. The presence of these stable and unstable vortex rolls is detrimental to the thin film growth from MOCVD processes and is obviously unwelcome. In the present study we intend to explore the possible suppression of the inertia-driven vortex rolls by placing a showerhead at the gas injection nozzle to force the inlet gas flow to become multiple jets of small diameter and the inertia-driven vortex rolls are expected to have less chance to appear. Experimental flow visualization will be conducted to observe the vortex flow in a model processing chamber for growth of thin crystal film for solar cells for various jet flow rates, temperature differences between the wafer and inlet gas flow, and jet-disk separation distances. Attention will be focused on the vortex flow pattern affected by the installation of the showerhead.
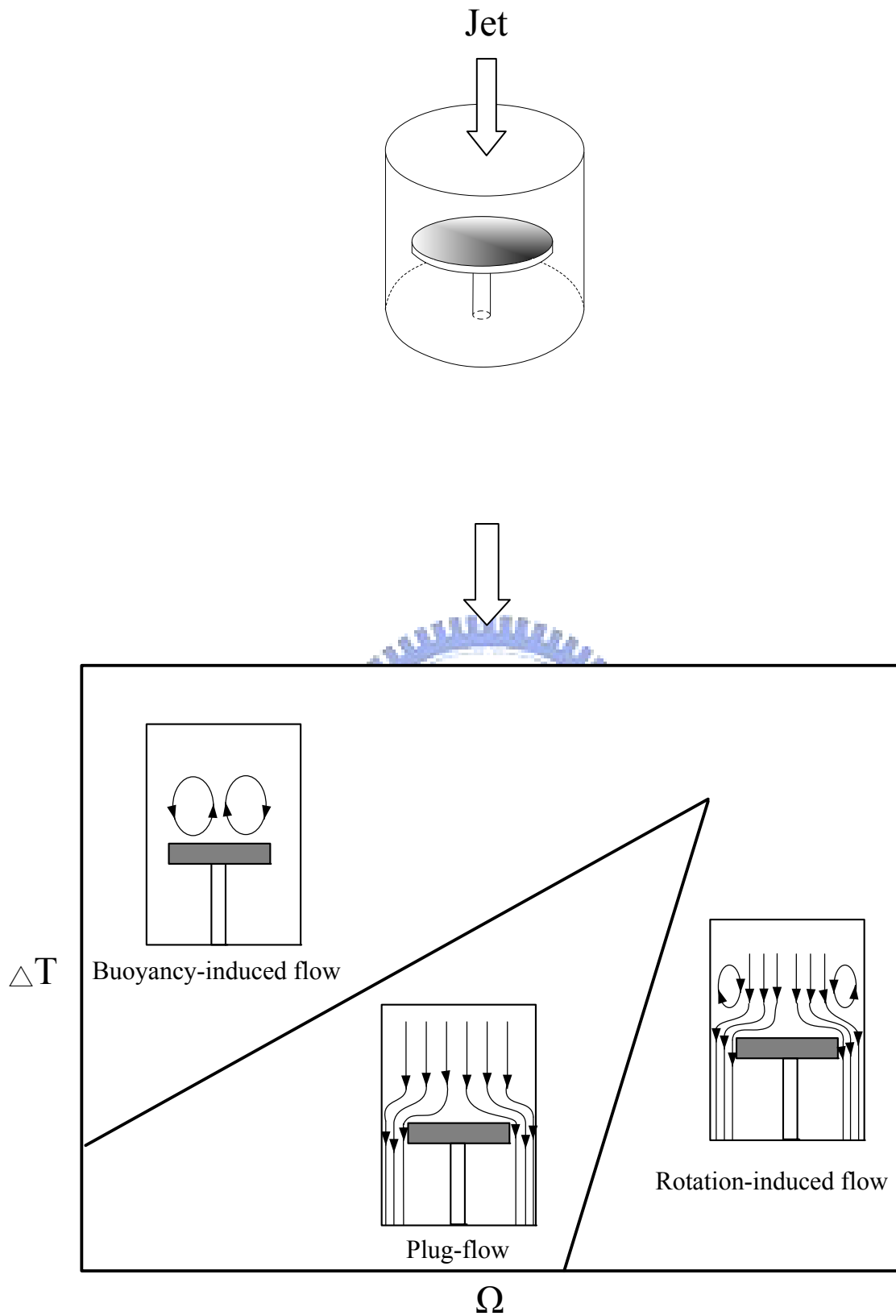
Fig. 1.1   Schematic of the flow patterns in a confined impinging jet depicting the

plug-flow, buoyancy-induced flow and rotation-induced flow.

D$_j$

Nozzle

Potential core

H

Free jet region

Stagnation region

Wall jet region
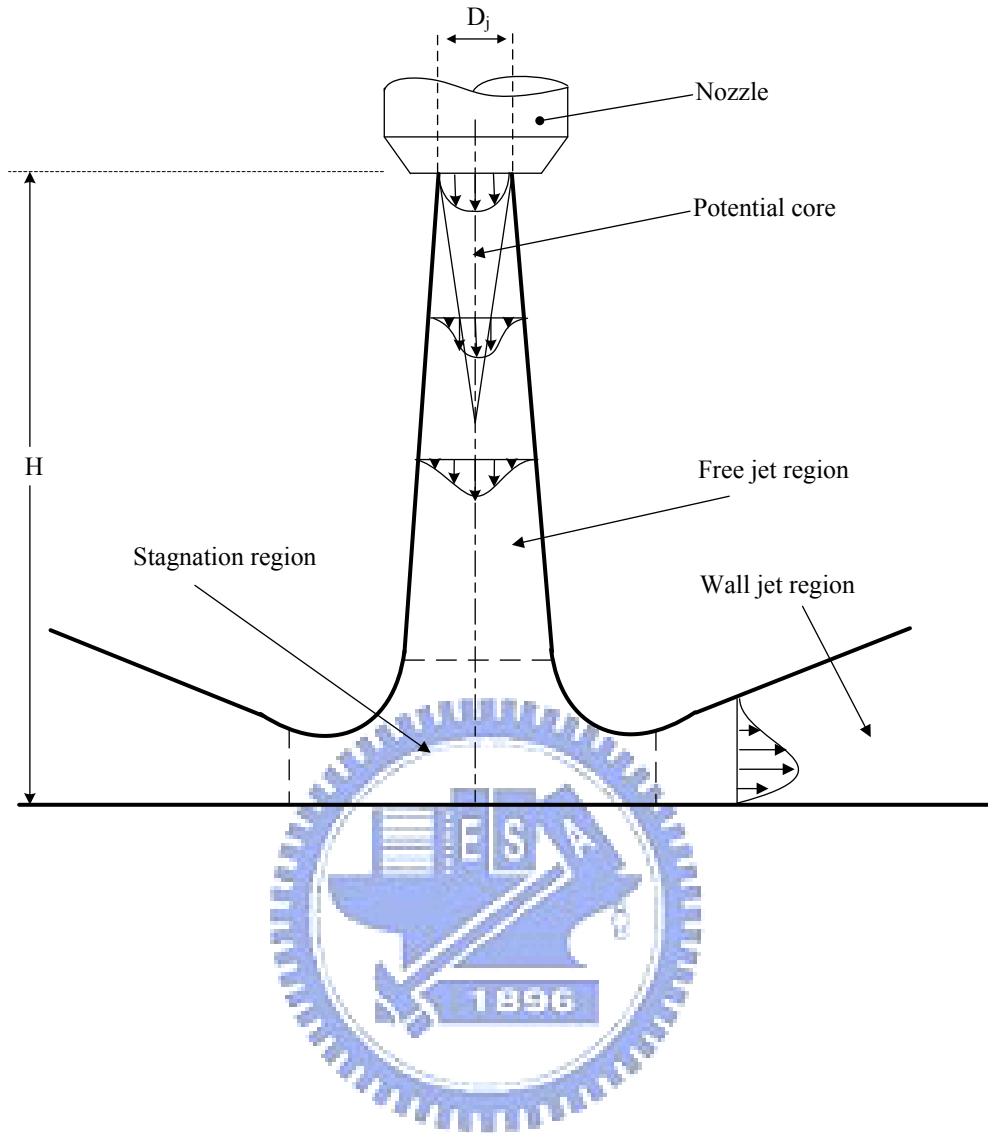
Fig. 1.2   Flow regions associated with a circular jet impinging onto a flat plate.

CHAPTER 2

EXPERIMENTAL APPARATUS AND PROCEDURES

In order to conduct the experiment at reasonably low cost, we use air as the working fluid to replace the inert gases normally employed in real MOCVD processes. In view of the similar thermodynamic and thermophysical properties for various gases, the results obtained here are still applicable to the MOCVD systems. The experimental apparatus and procedures used in the present study to examine how the installation of a showerhead at the injection nozzle affects the characteristics of the mixed convective vortex flow resulting from a gas jet impinging onto a horizontal heated disk confined in a vertical cylindrical chamber are modified slightly from that established in our previous study [15].
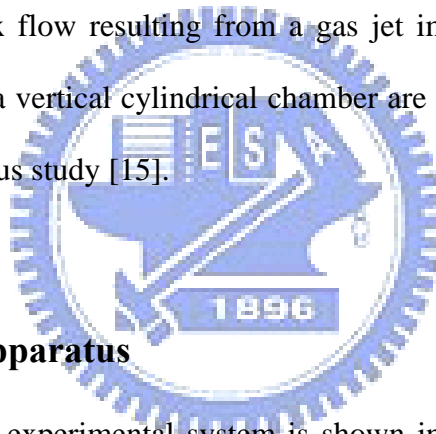
2.1 Experimental Apparatus

A schematic of the experimental system is shown in Fig. 2.1. The test section includes a circular disk held horizontally in a vertical cylindrical chamber with the gas injected vertically downward through a showerhead into the chamber. Note that for clear illustration the plots in Fig. 2.1 are not directly proportional to the actual dimensions of the apparatus. The present experimental system consists of four major parts: (1) gas injection unit, (2) processing chamber, (3) heating unit, and (4) flow visualization unit. The major parts are briefly described in the following.

Processing chamber: The processing chamber schematically shown by the top view and side view in Fig. 2.2, which is made of 6.0-mm thick quartz glass to allow

for the observation of the flow pattern in the chamber, is cylindrical and has a diameter of 291.0 mm. The distance between the chamber top and bottom is 200.0 mm. The chamber top is made of an 15-mm thick acrylic plate and the showerhead contains 490 circular holes all having the same diameter d_j of 0.5 mm and a pitch of 3.0 mm (Fig. 2.3). These holes form concentric rings and the showerhead has a diameter of 3-inch. To facilitate the flow visualization, air is injected vertically downward through the showerhead into the cylindrical chamber and impinges directly onto the heated disk. The air flows first over the heated disk, then moves through the annular section of the chamber, and finally leaves the chamber via twenty circular outlets of 12.7 mm in diameter opened at the bottom of the chamber. The outside surface of the chamber is thermally well insulated to reduce the heat loss from the processing chamber during the experiment. More specifically, the entire chamber is insulated with a superlon insulator of 10.0-mm thick. The insulator can be opened during the flow visualization experiment.
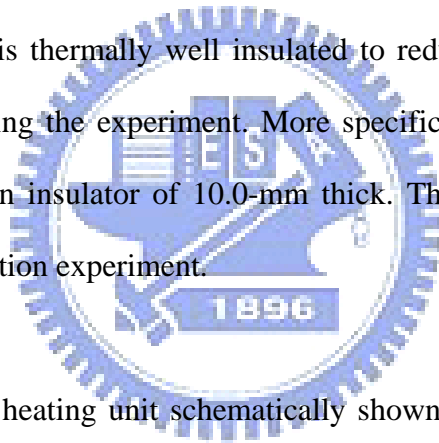
Heating unit: The heating unit schematically shown in Fig. 2.4 is designed to maintain the circular disk at the preset uniform temperature during the experiment. It is composed of 8-inch circular bakelite plate of 10.0-mm thick with a copper disk of 2-inch in diameter imbedded in its central portion. The copper disk is 11.0-mm thick and is placed on a thin heater of the same diameter which is heated by D.C. power supplies. The bakelite-copper plate and the heater are then placed on another bakelite disk. Note that the upper bakelite and copper disk surfaces must be at the exactly same horizontal level to avoid the wall jet flow to experience any step change between the surfaces. A proper control of the currents transferred from the power supplies to the heating coils leads to a nearly uniform copper disk temperature with a maximum deviation of 0.1℃ across the disk. The temperature of the copper disk at

selected detection points is measured by four T-type thermocouples inserted into the disk by the small holes drilled on the backside of the disk. The locations of the detection points in the disk are 1-mm below the upper surface of the disk and are indicated in Fig. 2.5.

Gas injection unit: The gas injection unit consists of a 2 HP air compressor, a flow meter, a smoke generator, filters, a pressure regulator, connection pipes, a diffuser of 357-mm long, and a 3-inch showerhead. In the experiments, the air is drawn from the ambient by the compressor and sent into a 300-liter and 100-psi high-pressure air tank and is filtered to remove moisture and tiny particles. The installation of the high-pressure air tank intends to suppress the fluctuation of the air flow and to extend the life of the compressor. The gas flow rate from the air tank is controlled by the mass flow meter and then, the air is mixed with smoke tracers in the smoke generator. Before injected into the processing chamber, the gas moves vertically downward into the diffuser and crosses the showerhead which is coaxial with the processing chamber. Finally, the small-diameter multiple air jets from the showerhead impinges directly onto the horizontal heated copper disk. In the present study, the diffuser is thermally well insulated by a superlon insulation layer of 16.0-mm thick to prevent heat loss from the air flow. The distance between the lower surface of the showerhead and the upper surface of the heated disk is varied from 20.0 to 40.0 mm. The air temperature at the inlet of the diffuser is measured by a T-type thermocouple. The measured value is considered as the temperature of the air injected into the processing chamber in view of the good thermal insulation over the diffuser.

Visualization unit: A smoke-tracer flow visualization technique is employed to observe the flow patterns resulting from the jet impinging onto a heated disk in the

cylindrical chamber. The smoke is produced from burning incense prepared from sandalwood. The smoke is mixed uniformly in the smoke generator and is carried out by the inlet air and is sent into the cylindrical chamber. The gas flow pattern in the chamber is illuminated by the vertical and horizontal plane light sheets produced by passing parallel lights from an overhead projector through adjustable knife edges. The experimental system is located in a darkroom to improve the contrast of the flow photos. The time variations of the flow pattern from the side views are recorded by the Sony digital video camera DCR-PC330.

2.2 Experimental Procedures

The experimental parameters included in the present study are the jet-disk separation distance, temperature difference between jet and disk, and jet flow rate. The temperature difference between jet and disk and jet flow rate are respectively varied from 0 to 25.0℃ and 0 to 5.0 slpm (standard liter per minute) for the jet-disk separation distance varying from 20.0 to 40.0 mm. The experiment starts with the air at the ambient temperature T_a compressed first into a smoke generator through the showerhead, and then injected into the cylindrical chamber. The air then moves over the heated copper disk and finally leaves the processing chamber. Meanwhile the temperature of the disk and the air flow rate is controlled at the preset levels. The temporal changes of the flow patterns in the chamber are photographed from the side view by the Sony digital video camera DCR-PC330 for various jet-disk separation distances, gas flow rates, and temperature differences between the disk and inlet air.
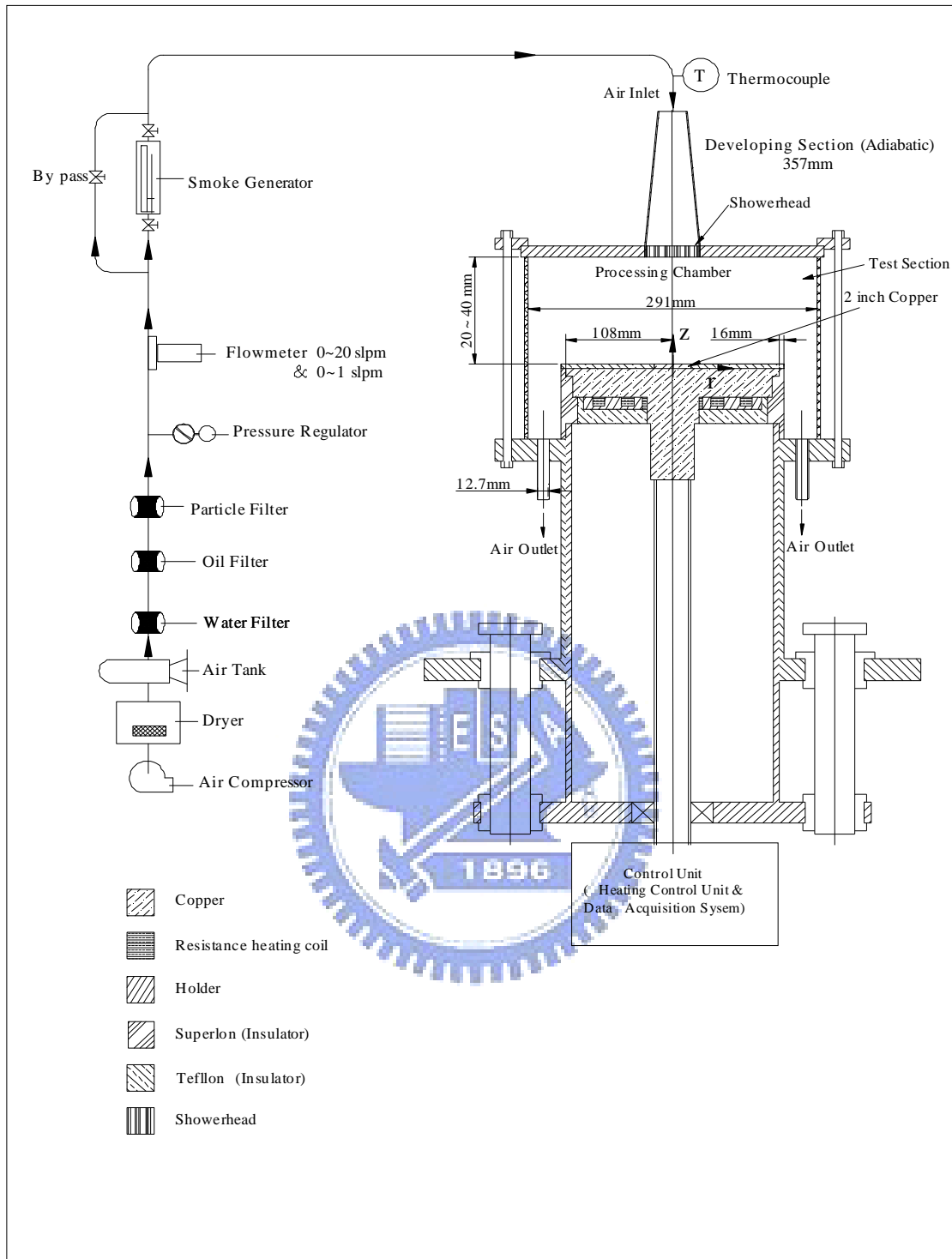
Fig. 2.1   Schematic diagram of the experimental apparatus.
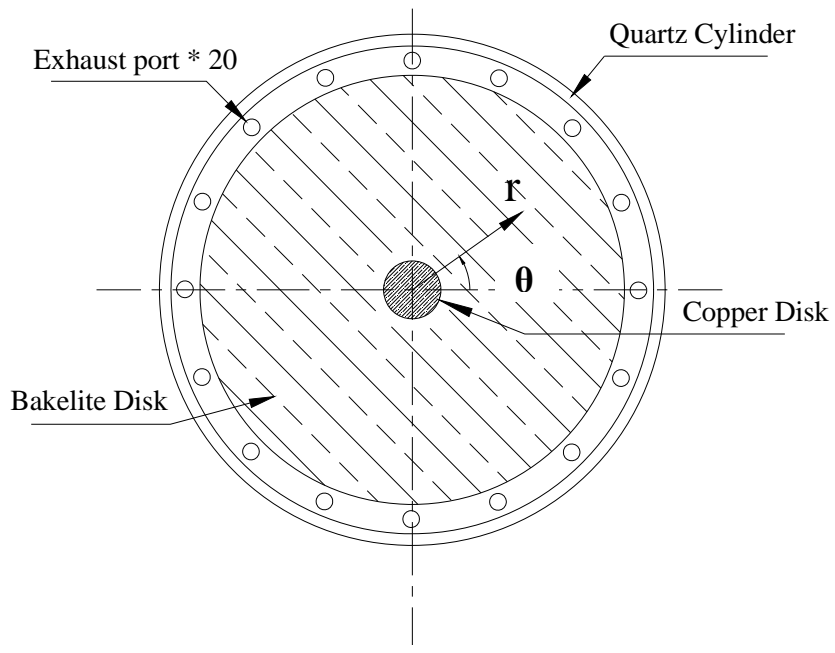
(a) Top View
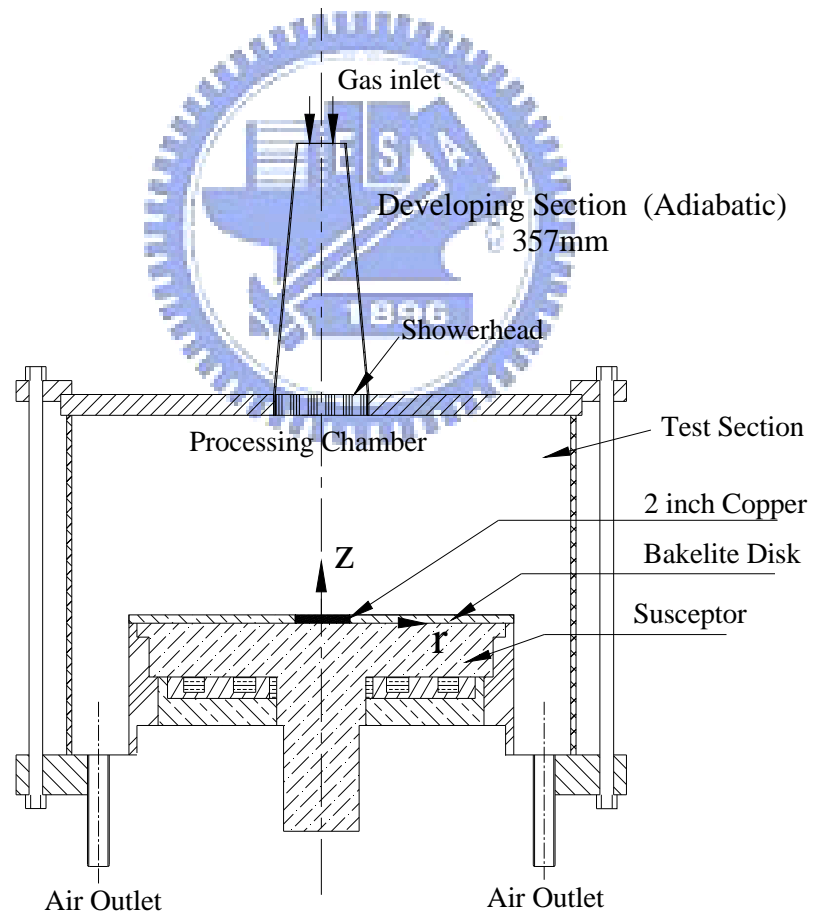
(b) Side View

Fig. 2.2   Schematic diagram of the processing chamber from (a) top view and (b)

side view.
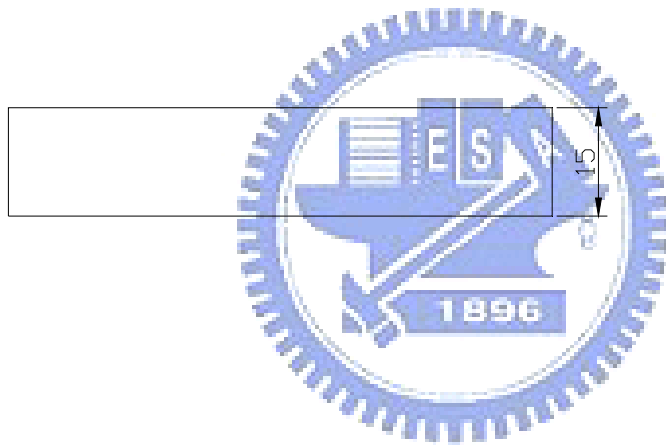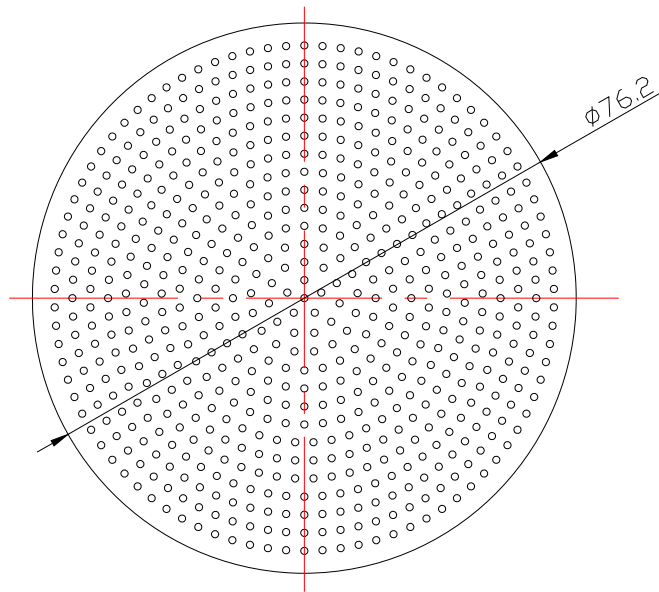
Unit: mm

Fig. 2.3   Schematic diagram of the showerhead.
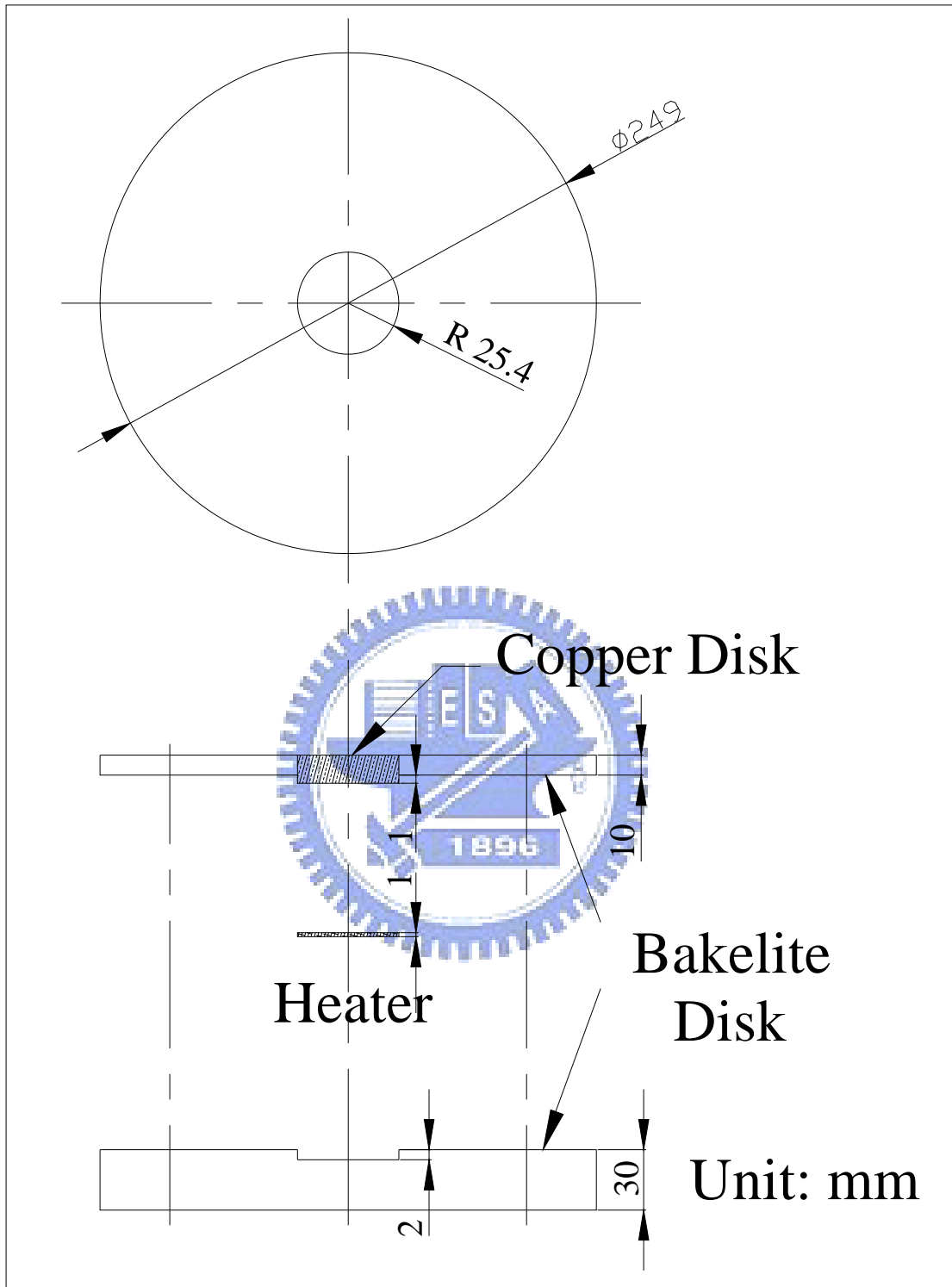
Fig. 2.4   Schematic diagram of heating unit.
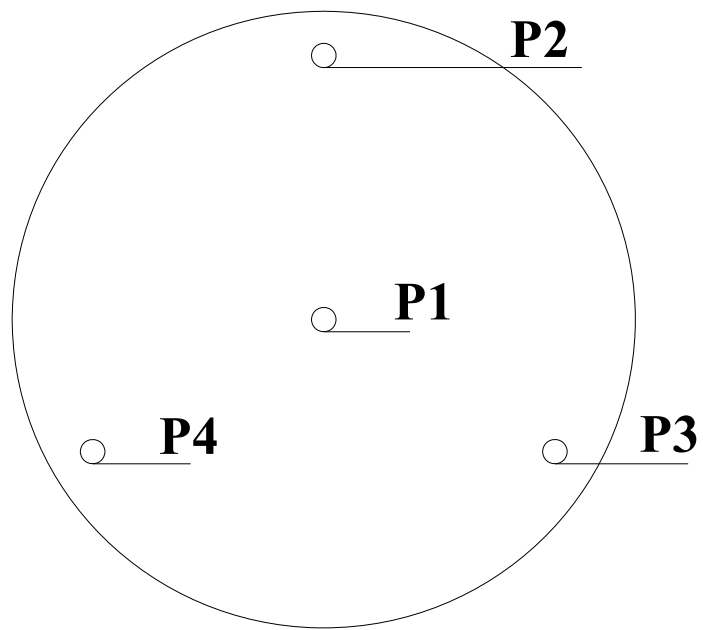
Fig. 2.5   Schematic diagram of the locations of the detection points

on the copper disk.
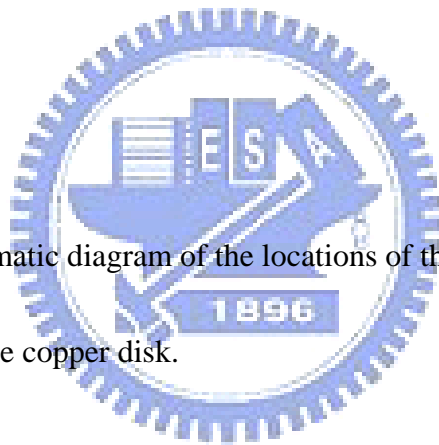
CHAPTER 3

DIMENSIONLESS GROUPS

AND UNCERTAINTY ANALYSIS

The dimensionless groups relevant to the present problem and the analysis of the uncertainties of the variables in this experiment are briefly examined in this chapter.

3.1 Dimensionless Groups

The non-dimensional parameters associated with the flow considered here are the ratio HD_n of the jet-disk separation distance H to the diameter of the nozzle D_n, overall jet Reynolds number Re_n based on the average speed of the air flow V_n at the injection nozzle and the diameter of the injection nozzle D_n, the jet Reynolds number Re_j based on the average speed of the air flow V_j leaving the holes in the showerhead and the diameter of each hole d_j, and the Rayleigh number Ra based on the temperature difference between the heated disk and inlet gas ΔT and the jet-disk separation distance H. They are respectively defined as

$$HD_n = \frac{H}{D_n} \tag{3.1}$$

$$Re_n = \frac{V_n D_n}{\nu} = \frac{4}{\pi} \frac{Q_j}{\nu D_n} \tag{3.2}$$

$$Re_j = \frac{V_j d_j}{\nu} = \frac{4}{N\pi} \frac{Q_j}{\nu d_j} \tag{3.3}$$

and $$Ra = \frac{g\beta(T_h - T_j)H^3}{\alpha\nu} = \frac{g\beta\Delta T H^3}{\alpha\nu} \tag{3.4}$$

where N is the number of the holes in the showerhead, α is the thermal diffusivity,

g is the gravitational acceleration, β is the thermal expansion coefficient, and ν is the kinematic viscosity.

3.2 Uncertainty Analysis

An uncertainty analysis is carried out here to estimate the uncertainty levels in the experiment. Kline and McClintock [51] proposed a formula for evaluating the uncertainty in the result F as a function of independent variables, $X_1, X_2, \cdots\cdots\cdots, X_n$,

$$F = F(X_1, X_2, X_3, \cdots\cdots, X_n) \tag{3.5}$$

The absolute uncertainty of F is expressed as

$$\delta F = \left\{ \left[\left(\frac{\partial F}{\partial X_1} \right) \delta X_1 \right]^2 + \left[\left(\frac{\partial F}{\partial X_2} \right) \delta X_2 \right]^2 + \left[\left(\frac{\partial F}{\partial X_3} \right) \delta X_3 \right]^2 + \cdots + \left[\left(\frac{\partial F}{\partial X_n} \right) \delta X_n \right]^2 \right\}^{\frac{1}{2}} \tag{3.6}$$

and the relative uncertainty of F is

$$\frac{\delta F}{F} = \left\{ \left[\left(\frac{\partial \ln F}{\partial \ln X_1} \right) \left(\frac{\delta X_1}{X_1} \right) \right]^2 + \left[\left(\frac{\partial \ln F}{\partial \ln X_2} \right) \left(\frac{\delta X_2}{X_2} \right) \right]^2 + \cdots + \left[\left(\frac{\partial \ln F}{\partial \ln X_n} \right) \left(\frac{\delta X_n}{X_n} \right) \right]^2 \right\}^{\frac{1}{2}} \tag{3.7}$$

If $F = X_1^a X_2^b X_3^c \ldots\ldots$, then the relative uncertainty is

$$\frac{\delta F}{F} = \left[\left(a \frac{\delta X_1}{X_1} \right)^2 + \left(b \frac{\delta X_2}{X_2} \right)^2 + \left(c \frac{\delta X_3}{X_3} \right)^2 + \cdots\cdots \right]^{\frac{1}{2}} \tag{3.8}$$

where $(\partial F / \partial X_i)$ and δX_i are, respectively, the sensitivity coefficient and uncertainty level associated with the variable X_i. The values of the uncertainty intervals δX_i are obtained by a root-mean-square combination of the precision uncertainty of the instruments and the unsteadiness uncertainty, as recommended by

Moffat [52]. The choice of the variable X_i to be included in the calculation of the total uncertainty level of the result F depends on the purpose of the analysis. The uncertainties for the chosen parameters are calculated as follows:

(1) Uncertainty of the measured temperature difference $\Delta T = T_h - T_j$

$$\delta(T_h - T_j) = [(\delta T_h)^2 + (\delta T_j)^2]^{\frac{1}{2}} \qquad (3.9)$$

(2) The dependence of the air properties k, μ, and ν on temperature (T in K) [46] is

$$k = 1.195 \times 10^{-6} T^{1.6} / (T + 118)$$

$$\mu = 1.448 \times 10^{-6} T^{1.5} / (T + 118) \qquad (3.10)$$

$$\nu = \mu / \rho$$

The uncertainties of the properties are

$$
\begin{aligned}
\frac{\delta k}{k} &= \frac{T}{k} \frac{\partial k}{\partial T} \frac{\delta T}{T} \\
\frac{\delta \rho}{\rho} &= \frac{T}{\rho} \frac{\partial \rho}{\partial T} \frac{\delta T}{T} \\
\frac{\delta \mu}{\mu} &= \frac{T}{\mu} \frac{\partial \mu}{\partial T} \frac{\delta T}{T}
\end{aligned}
\qquad (3.11)
$$

(3) Uncertainty of the ratio HD_n,

$$HD_n = \frac{H}{D_n} \qquad (3.12)$$

$$\frac{\delta HD_n}{HD_n} = \left[\left(\frac{\delta H}{H} \right)^2 + \left(\frac{\delta D_n}{D_n} \right)^2 \right]^{1/2} \qquad (3.13)$$

(4) Uncertainty of the Rayleigh number Ra,

$$Ra = \frac{g\beta(T_h - T_j)H^3}{\alpha\nu} = \frac{g\beta\Delta T H^3}{\alpha\nu}$$ (3.14)

$$\frac{\delta Ra}{Ra} = \left[\left(\frac{\delta g\beta}{g\beta}\right)^2 + \left(3\frac{\delta H}{H}\right)^2 + \left(\frac{\delta\Delta T}{\Delta T}\right)^2 + \left(\frac{\delta\alpha}{\alpha}\right)^2 + \left(\frac{\delta\nu}{\nu}\right)^2\right]^{1/2}$$ (3.15)

(5) Uncertainty of the overall jet Reynolds number Re_n,

$$Re_n = \frac{V_n D_n}{\nu} = \frac{4}{\pi}\frac{Q_j}{\nu D_n}$$ (3.16)

$$\frac{\delta Re_n}{Re_n} = \left[\left(\frac{\delta\nu}{\nu}\right)^2 + \left(\frac{\delta Q_j}{Q_j}\right)^2 + \left(\frac{\delta D_n}{D_n}\right)^2\right]^{1/2}$$ (3.17)

(6) Uncertainty of the jet Reynolds number Re_j,

$$Re_j = \frac{V_j d_j}{\nu} = \frac{4}{N\pi}\frac{Q_j}{\nu d_j}$$ (3.18)

$$\frac{\delta Re_j}{Re_j} = \left[\left(\frac{\delta\nu}{\nu}\right)^2 + \left(\frac{\delta Q_j}{Q_j}\right)^2 + \left(\frac{\delta d_j}{d_j}\right)^2\right]^{1/2}$$ (3.19)

The results from this uncertainty analysis are summarized in Table 3.1.

Parameter and Estimate Uncertainty	
Parameters	Uncertainty
H (m)	± 0.00005 m
D_n	± 0.000005 m
d_j	± 0.0000005 m
T (℃)	± 0.2℃
ΔT (℃)	± 0.3℃
Q_j (slpm)	± 2%
μ (kg/ms)	± 0.05%
ρ (kg/m^3)	± 0.05%
υ (m^2/s)	± 0.07%
HD_n	± 1.67%
Ra	± 8.6%
Re_n	± 2.0%
Re_j	± 2.0%

Table 3.1   Summary of uncertainty analysis

CHAPTER 4

RESULTS AND DISCUSSION

It is noted that the flow characteristics associated with the air jet impinging onto the heated disk confined in the cylindrical chamber under investigation are affected by the jet inertia, buoyancy force due to the heated disk, and jet-disk separation distance. In the present experiment the chamber is at the atmospheric pressure. Three jet-disk separation distances are considered with H = 20.0, 30.0, and 40.0 mm for the total jet flow rate Q_j ranging from 0 to 5.0 slpm (standard liter per minute) and the temperature difference between the disk and the air injected into the chamber ΔT is varied from 0 to 25.0℃. As noted in Chapter 3, the dimensionless groups governing the flow are the ratio of the jet-disk separation distance to diameter of the nozzle, jet Reynolds numbers and Rayleigh number. They have been respectively defined in Chapter 3 as

$$HD_n = \frac{H}{D_n} \tag{4.1}$$

$$Re_n = \frac{V_n D_n}{\nu} = \frac{4}{\pi} \frac{Q_j}{\nu D_n} \tag{4.2}$$

$$Re_j = \frac{V_j d_j}{\nu} = \frac{4}{N\pi} \frac{Q_j}{\nu d_j} \tag{4.3}$$

$$Ra = \frac{g\beta(T_h - T_j)H^3}{\alpha\nu} = \frac{g\beta\Delta T H^3}{\alpha\nu} \tag{4.4}$$

The Grashof number is defined as

$$Gr = \frac{g\beta\Delta T H^3}{\nu^2} = Ra/\Pr \tag{4.5}$$

Thus the nondimensional jet-disk separation distance HD_n ranges from 0.26 to 0.52,

the overall jet Reynolds number Re_n from 0 to 89, the jet Reynolds number Re_j from 0 to 28, the Rayleigh number Ra from 0 to 150,325, and the Grashof number Gr from 0 to 214,750. The inclusion of the two jet Reynolds numbers here intends to illustrate the effects of the showerhead on the resulting vortex flow in the chamber. In what follows selected flow photos taken from the side view are examined closely to delineate how the gas flow characteristics in the chamber with the showerhead installed at the gas injection nozzle are affected by the relevant parameters. Besides, the results for the cases with and without the showerhead installation are compared and discussed.

4.1 Pure Buoyancy- and Inertia- Driven Vortex Flow Patterns

At first, the vortex flow pattern in the chamber with the showerhead installation for the limiting case of no flow injection to the processing chamber at $Q_j = 0$ in examined. This is the pure natural convection flow. The typical steady natural convective vortex flow pattern observed in the cylindrical chamber with H = 20.0 mm, $\Delta T = 25°C$ and $Q_j = 0$ slpm ($HD_n = 0.26$, Ra = 18,790, $Re_n = 0$ and $Re_j = 0$) at long time when the flow already reaches steady state is illustrated in Fig. 4.1. The steady flow photo from the side view is shown here along with the corresponding schematically sketched vortex flow pattern to indicate the actual direction of the flow recirculation, which is based on the detailed flow visualization. The results manifest that there is a big buoyancy-driven circular roll in the processing chamber. A close inspection of the successive side view flow photos in the video tapes taken during the time evolution of the vortex flow reveals that the vortex roll almost fills the entire chamber and is nearly axisymmetric. Note that the buoyancy force pushes the gas to rise in the central portion of the chamber above the heated copper disk. As the gas flow encounters the chamber top, it moves radially outward along the top. Meanwhile,

the gas flow slows down and gets cooled during this outward moving. At some radial location it descends and later encounters the bakelite plate. The flow then moves radially inward forming a circular roll. We also note that this roll drags the air in the annular section of the chamber upward through viscous shearing effect, resulting a weak and small circular roll near the chamber side.

The typical vortex flow pattern in the cylindrical chamber with the showerhead installation for another limiting case of no buoyancy effect with H = 30.0 mm, ΔT = 0℃ and Q_j = 5 slpm (HD_n = 0.39, Ra = 0, Re_n = 89 and Re_j = 28) at long time when the flow already reaches steady state is illustrated in Fig. 4.2. The steady flow photo from the side view is also shown here along with the corresponding schematically sketched vortex flow pattern to indicate the actual direction of the flow recirculation, which is based on the detailed flow visualization. This is the pure inertia-driven vortex flow. Note that there are two circular rolls in the processing chamber. A close inspection of the successive side view flow photos in the video tapes taken during the transient stage of the flow formation reveals that immediately after the impinging, the gas flow is deflected to move radially outward along the bakelite plate and slows down significantly due to the radial spread of the wall-jet flow. The wall-jet flow travels a certain distance from the stagnation point and then moves obliquely upwards since the wall jet momentum is unable to overcome the wall friction and the retarding effects of the entrained flow in the upper part of chamber. Then, the oblique flow is divided into two streams as it encounters the chamber top. One stream moves radially inwards towards the low pressure region created by the viscous shearing of the surrounding fluid associated with the jet injection, forming the inner roll which is therefore considered as the primary inertia-driven roll. Another stream is defected by the chamber top to move obliquely downwards along the edge of the bakelite disk, and finally leaves the chamber through the outlets in the chamber bottom. The outer

roll near the sidewall of the chamber is formed by the backflow from the outlets and rotates in the same direction as the primary inertia driven roll, which is called the corner roll. This corner roll becomes bigger and stronger for an increase in HD_n as shown for Fig. 4.3. It is noted that at a small jet Reynolds number the region above the copper disk is dominated by the plug flow. Furthermore, at high Q_j a smaller third roll which exists in the region between the primary inertia-driven roll and corner roll is found to be induced through the viscous shearing effects produced by the stronger and larger primary inertia-driven roll, which is termed as the secondary inertia-driven roll and has the opposite rotating direction with the primary inertia-driven roll. Both the primary inertia-driven roll and secondary inertia-driven roll become stronger and larger at increasing flow rate and jet-disk separation distance which can be seen from the flow photos in Fig. 4.4. The primary roll is known to result from the flow separation at the sudden expansion in the cross-sectional area as the jet flow enters the chamber, as already pointed out by Fotiadis et al. [46 & 47].
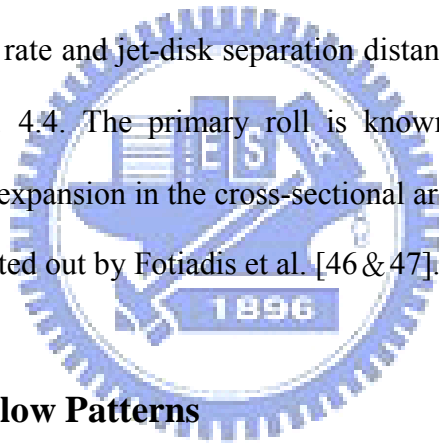
4.2 Typical Vortex Flow Patterns

Next, when there is a temperature difference between the jet and copper disk the typical steady vortex flow in the processing chamber with the showerhead installation shown in Fig. 4.5 for H = 20.0-40.0 mm, $\Delta T = 10.0℃$ and $Q_j = 2.0$ slpm (HD_n = 0.26-0.52, Re_j = 11, Ra = 7,516-60,130, and Gr / Re_j^2 = 62.11-496.94) is somewhat different from that in Fig. 4.3 for $\Delta T = 0℃$. Note that when ΔT is raised to $10.0℃$ the downward multiple-jet flow issuing from the showerhead is deflected to move radially outward at certain upper location by the vertically upward buoyancy generated by the heated disk and no corner roll is induced when the radial flow hits the chamber side. But, the photo in Fig. 4.5(a) reveals that a weak buoyancy-driven roll has been pushed far away from the heated disk by the strong jet flow. For larger

HD_n of 0.39 and 0.52 (Figs. 4.5(b)＆(c)) a big and strong buoyancy-driven circular roll, however, appears since the Rayleigh number is proportional to H^3. In fact the flow in the chamber is dominated by the buoyancy-driven roll at these larger HD_n. Again no inertia-driven vortex roll exists due to the large buoyancy-to-inertia ratio. Thus, we move further to examine the flow pattern for a higher gas flow rate of 5.0 slpm in Fig. 4.6. The steady flow photos from the side view show that the buoyancy-driven roll is pushed outward by the stronger jet flow when Q_j is increased to 5.0 slpm and it becomes smaller and weaker. Besides, a primary inertia-driven roll appears in the region near the edge of the showerhead (Fig. 4.6(a)). The appearance of this roll is attributed to the high speed gas flow experiencing a sudden expansion of the flow cross section at the exit of the jet injection nozzle as the flow enters the chamber. This roll is bigger and stronger for a large HD_n (Figs. 4.6(b)＆(c)). Moreover, it should be noted that at increasing HD_n both the primary inertia-driven roll and buoyancy-driven roll are larger and contact with each other. These results are similar to that observed by Fotiadis et al. [46＆47].
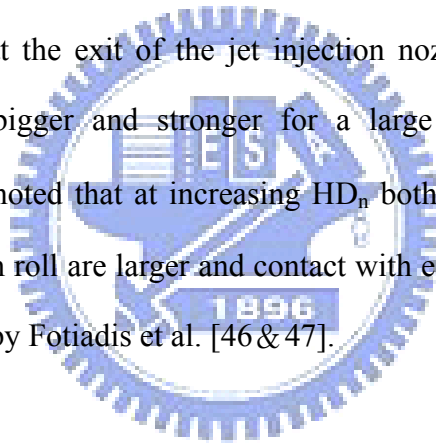
4.3 Onset of Inertia-Driven Vortex Flow

The understanding of the critical condition for the appearance of the inertia-driven vortex roll in the chamber is of fundamental interest in the fluid flow study and is valuable in vertical MOCVD thin film growth with the showerhead installation. Here, we move further to investigate the onset of inertia-driven vortex roll by visualizing the flow in the processing chamber at lower jet Reynolds number for the copper disk unheated (Ra = 0). The present data are summarized in Table 4.1 for the onset of the primary and secondary inertia-driven vortex rolls at HD_n = 0.26-0.52. The trend is different from the previous study by Hsieh and Lin [18], which did not install the showerhead. Note that with the showerhead installation the onset of

the primary roll is delayed to a higher Re_j. This can be attributed to some unique features of the multiple small-diameter impinging jets resulting from the installation of the showerhead. As the present small-diameter jets with short pitches impinge the heated copper disk, the wall-jet flow streams from the adjacent impinging jets tend to offset each other and no vortice is induced, as schematically illustrated in Fig. 4.7. Obviously, the peripheral jets issuing from the holes closest to the showerhead edge can induce circular rolls which are apparently much weaker than that driven by the jet without the showerhead installation. Hence, the critical jet Reynolds number increases significantly by installing the showerhead. From the Table 4.1, at low average jet Reynolds number ($Re_j < 8.7$) the plug flow dominates and only a corner roll appears near the sidewall. But, a small increase in Q_j causes the primary inertia-driven roll to emerge from the edge of the showerhead. Moreover, the onset of the primary inertia-driven roll is delayed for an increase in HD_n. The data in Table 4.1 also manifest that the critical jet Reynolds number for the onset of secondary inertia-driven roll is nonmonotonic. This can be ascribed to the fact that at the small HD_n of 0.26 the chamber does not have enough space for the secondary inertia-driven roll to emerge. Thus a higher Re_j is needed for the onset of the secondary roll. On the other hand, at the high HD_n of 0.52 the primary inertia-driven and corner rolls are relatively large (Fig. 4.8(c)) and the space left in the chamber for the appearance of the secondary roll is again very limited. Hence a high Re_j is also needed for the roll onset. As a result, at the intermediate HD_n of 0.39 the critical Re_j for the onset of the secondary roll is lowest.

Next, when there is a temperature difference between the jet and disk, the large buoyancy-driven roll is suppressed and a primary inertia-driven roll appears near the edge of the showerhead as the jet flow rate Q_j is increased to a certain value so that the buoyancy-to-inertia ratio Gr / Re_j^2 is below a critical level, which is shown in Fig.

4.9 for various Q_j and HD_n at $\Delta T = 5^\circ C$. The critical values for the onset of the inertia-driven roll for various ΔT are summarized in Table 4.2. The results show that for $HD_n = 0.26\text{-}0.52$, the critical Re_j for the onset of the primary roll is higher for a higher ΔT, indicating that the flow inertia needs to be stronger to overcome the stronger buoyancy roll for the primary inertia driven vortex roll to appear. Besides, the critical buoyancy-to-inertia ratio increases substantially with Ra and HD_n. Furthermore, we found in the experiment that when the HD_n is raised to 0.39 and 0.52, the observed flow pattern reveals that for $\Delta T \geqq 1.0^\circ C$ the buoyancy-driven vortex roll always exists in the chamber even at the highest Q_j of 5.0 slpm tested here. Finally, there is no room available for the appearance of the secondary inertia-driven roll when the inertia and buoyancy rolls grow to a certain finite size and contact each other.

4.4 Effects of Parameters on Vortex Flow Characteristics

How the experimental parameters affect the gas flow pattern at long time in the processing chamber with the installation of the showerhead is demonstrated in Figs. 4.10-4.33 for $HD_n = 0.26\text{-}0.52$ by presenting the long time side view flow photos taken at the cross plane $\theta = 0^\circ \,\&\, 180^\circ$ for various Re_j and Ra. At first, the results from Figs. 4.10-4.14 for $HD_n = 0.26$ show that at low Re_j a large circular roll is driven by the buoyancy (Figs. 10(a)$\&$(b), 11(a)$\&$(b), 12(a)-(c), 13(a)-(e), 14(a)-(e)). For a small increase in the jet Reynolds number this buoyancy roll is pushed outward by the jet inertia. Meanwhile, another small circular roll is induced right above the copper disk also by the buoyancy (Figs. 10(c)$\&$(d), 11(d), 12(f), 13(f)$\&$(g), 14(d)$\&$(e)). The two buoyancy rolls decay noticeably for a further increase in Re_j. At a certain high Re_j the inner buoyancy roll disappears and the outer buoyancy roll becomes small and weak. However, at this high Re_j the primary inertia-driven appears. The primary roll

31

grows in size and intensity at increasing Re_j. It is of interest to note that the flow does not reach steady state when the inner buoyancy roll is present.

For an increase of HD_n to 0.39, both the buoyancy and inertia effects on the vortex flow are expected to be stronger. The results shown in Figs. 4.15-4.24 for HD_n = 0.39 do exhibit these trends and can be clearly seen in Fig. 4.20 for $\Delta T = 7.0°C$ (Ra =17,757) at various Re_j. Specifically, at this higher HD_n the flow in the chamber is dominated by a big buoyancy-driven circular roll at a low Re_j (Fig 4.20(a)). A small increase in Re_j is found to reduce the vertical extent of the buoyancy roll (Fig. 4.20(b)) and the roll becomes somewhat slender. For a further increase in Re_j the upper part of the buoyancy roll indents to some degree near the outer edge of the showerhead (Fig. 4.20(c)). At a slightly higher Re_j the indentation of the buoyancy roll becomes more prominent (Fig. 4.20(d)). For an even higher Re_j the buoyancy roll indentation is very severe and it is about to break into two small rolls (Fig. 4.20(e)). In the mean time a small primary inertia-driven roll appears near the outer edge of the showerhead. As the jet Reynolds number is further raised, the two buoyancy rolls are suppressed to become smaller and the primary inertia-driven roll grows stronger and larger (Figs. 4.20(f) & (g)). For Re_j raised to exceed a certain high value the inner buoyancy roll is completely suppressed and only the outer buoyancy roll is seen (Figs. 4.20(h)-(l)). A close inspection of the results reveals that for the cases with the presence of the splitting of the buoyancy roll the flow does not reach steady state at long time (Figs. 4.20(d)-(g)). For an even larger HD_n of 0.52 the effects of the jet Reynolds number on the vortex flow in the chamber are similar to that presented above for HD_n= 0.39, as evident from the results shown in Figs. 4.25-4.33. But at this larger HD_n the corner roll is larger and stronger especially at low Re_j and Ra.

4.5 Flow Regime Maps

In the MOCVD growth of thin crystal film the vortex flow pattern in the processing chamber is important. Therefore the gas flow pattern in the processing chamber is examined closely. Four different gas flow patterns can be identified from the flow photos presented in Figs. 4.10-4.33: (1) plug flow – no vortices are induced in the chamber; (2) buoyancy-driven vortex flow – the chamber is dominated by the buoyancy-driven rolls; (3) inertia-driven vortex flow – inertia-driven rolls dominate in the chamber; (4) mixed vortex flow – the chamber is dominated simultaneously by the inertia- and buoyancy-driven rolls. Flow regime maps in terms of Ra vs. Re_n delineating these gas flow patterns based on the present data are given in Figs. 4.34-4.36 for various jet-disk separation distances. The results indicate that only at Ra=0 and low Re_n the plug flow prevails. At a high Re_n but for Ra = 0 the inertia-driven vortex flow dominates. While for Ra exceeding certain low level the buoyancy-driven vortex flow is predominant at high buoyancy-to-inertia ratio and the mixed vortex flow prevails at low buoyancy-to-inertia ratio.

Based on the present data for $HD_n = 0.26$ the boundary separating the buoyancy-driven and mixed vortex flows can be empirically correlated as

$$Ra = -6.27 \times 10^4 + 4.82 \times 10^3 \times Re_n - 1.165 \times 10^2 \times Re_n^2 + 0.99 \times Re_n^3 \qquad (4.6)$$

with a standard deviation of 2.42% for $30 \leq Re_n \leq 58$ and $3{,}758 \leq Ra \leq 22{,}548$. For $HD_n = 0.39$ this boundary is correlated as

$$Ra = 6.963 \times 10^5 - 4.905 \times 10^4 \times Re_n + 1.104 \times 10^3 \times Re_n^2 - 7.693 \times Re_n^3 \qquad (4.7)$$

with a standard deviation of 7.45% for $36 \leq Re_n \leq 57$ and $2{,}536 \leq Ra \leq 63{,}418$. Then, the separating boundary for $HD_n = 0.52$ can be correlated as

$$Ra = 1.245 \times 10^5 - 1.351 \times 10^4 \times Re_n + 4.783 \times 10^2 \times Re_n^2 - 5.152 \times Re_n^3 \qquad (4.8)$$

with a standard deviation of 2.42% for $22.5 \leq Re_n \leq 66.5$ and $3{,}758 \leq Ra \leq 22{,}548$.

It is also well known that the temporal state of the gas flow in the processing chamber is important in the thin film growth. Hence flow regime maps delineating the temporal state of the flow studied here are also provided in Figs. 4.37-4.39. The results show that for a given Ra the vortex flow is steady at low and high jet Reynolds numbers. But at the intermediate range of Re_n the flow is time dependent. The unsteady vortex flow is non-periodic for $HD_n = 0.26$. The evolution of the non-periodic vortex flow for a typical case at $HD_n = 0.26$ is shown in Fig. 4.40. The results show that the two small buoyancy rolls above the heated disk gradually decay and merge together. Finally, they disappear. But later a new vortex roll pair is induced and it gradually grows into two rolls. But for the larger HD_n of 0.39 and 0.52 we have time periodic flow in the chamber after the primary inertia-driven roll appearance. The evolution of the time periodic vortex flow for $HD_n = 0.39$ is illustrated in Fig. 4.41 by presenting the side view photos at selected time instants in a typical cycle ($t_p = 8.0sec$). The flow is characterized by the significant growth and decay of the two buoyancy-driven rolls with time. This is the buoyancy unstable vortex flow occurring entrainment effect. At some time instants the two rolls nearly separate from each other. But the two rolls nearly merge together at the other time instants. While at the large HD_n of 0.52 the two buoyancy rolls are large and contact with each other (Fig. 4.42). In the first half of the periodic cycle one roll grows and pushes the other roll and the opposite process takes place in the second half of the cycle. Thus we have mutual-pushing vortex flow instability.

Finally, we correlate these data given in the flow regime maps. The lower and upper bounds of the non-periodic vortex flow instability for H = 20.0mm can be empirically correlated as

$$Ra = -9.92 \times 10^3 + 4.03 \times 10^2 \times Re_n^2 - 1.311 \times 10^2 \times Re_n^{2.5} + 11.23 \times Re_n^3 \qquad (4.9)$$

with a standard deviation of 0.51% for $14 \leq Re_n \leq 37$ and $3,758 \leq Ra \leq$

18,790

and

$$Ra = -4.73 \times 10^4 + 4.03 \times 10^3 \times Re_n - 1.046 \times 10^2 \times Re_n{}^2 + 0.94 \times Re_n{}^3 \qquad (4.10)$$

with a standard deviation of 0.42% for $27 \leq Re_n \leq 58.5$ and $3,758 \leq Ra \leq 18,790$.

The lower and upper bounds of the time-periodic vortex flow instability for H = 30.0mm can be correlated as

$$Ra = -5.915 \times 10^6 + 6.742 \times 10^5 \times Re_n - 3.01 \times 10^4 \times Re_n{}^2 + 6.566 \times 10^2 \times Re_n{}^3 \qquad (4.11)$$
$$- 6.982 \times Re_n{}^4 + 0.029 \times Re_n{}^5$$

with a standard deviation of 10.64% for $31 \leq Re_n \leq 58$ and $2,536 \leq Ra \leq 63,418$

and

$$Ra = 2.795 \times 10^5 - 2.279 \times 10^4 \times Re_n + 6.653 \times 10^2 \times Re_n{}^2 - 8.117 \times Re_n{}^3 \qquad (4.12)$$
$$+ 0.0361 \times Re_n{}^4$$

with a standard deviation of 14.71% for $36 \leq Re_n \leq 80$ and $2,536 \leq Ra \leq 38,051$.

While for H = 40.0mm the lower and upper bounds can be correlated as

$$Ra = -2.275 \times 10^6 + 1.503 \times 10^5 \times Re_n - 3.307 \times 10^3 \times Re_n{}^2 + 24.51 \times Re_n{}^3 \qquad (4.13)$$

with a standard deviation of 7.49% for $38 \leq Re_n \leq 61$ and $6,013 \leq Ra \leq 150,325$
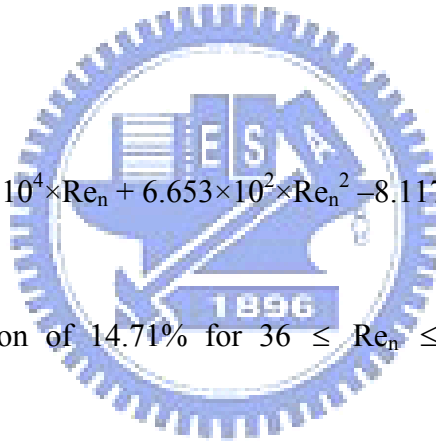
and

$$Ra = -1.722 \times 10^6 + 9.994 \times 10^4 \times Re_n - 1.934 \times 10^3 \times Re_n{}^2 + 12.649 \times Re_n{}^3 \qquad (4.14)$$

with a standard deviation of 9.71% for $43.5 \leq Re_n \leq 72$ and $6,013 \leq Ra \leq 90,195$.

4.6 Comparison of Vortex Flows with and without Showerhead Installation

To further reveal the effects of the showerhead installation on the resulting vortex flow, we compare the vortex flow in the same chamber with and without showerhead installation. By installing the showerhead, the large-diameter gas jet at the injection nozzle is broken into a great number of the tiny jets (Fig. 4.43). The tiny jets move at a much high speed because $V_j / V_n = D_n^2 / (N d_j^2) = 47.4$ but at a much lower Reynolds number $Re_j / Re_n = D_n / (N d_j) = 0.311$. Figures 4.44-46 shows the flow photos taken from the chamber with and without showerhead installed for the limiting cases of $\Delta T = 0℃$ at the same H and Q_j. Note that the inertia-driven vortex rolls are large and strong at high Q_j when no showerhead is installed (Figs. 4.44(a), 4.45(a) & 4.46(a)) for $Q_j \geq 2.0$ slpm. With the showerhead installation the inertia-driven rolls are much smaller and weaker (Figs. 4.44(b), 4.45(b) & 4.46(b)) and there rolls appear in the outer zone of the chamber. We further make this comparison for $\Delta T \geq 5.0℃$ in Figs. 4.47-4.52 for H = 20.0 to 40.0 mm. The results clearly show that the showerhead installation can effectively suppress the inertia-driven rolls. But the buoyancy-driven roll may become larger and stronger. Besides from Table 4.3, the onset of the inertia-driven rolls without the showerhead installation for the disk unheated (Ra=0) indicate that the primary and secondary rolls appear earlier than that with the showerhead installation.

Table. 4.1   Critical condition for the onset of the primary and secondary inertia-driven vortex rolls for H = 20-40 mm with disk unheated (Ra=0)

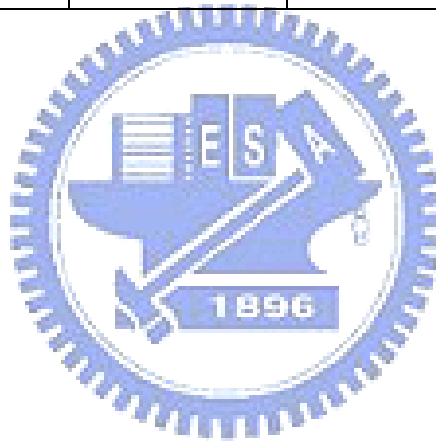|	Separation Distance (H, mm)	Flowrate $(Q_j, SLPM)$	Re_n	Re_j
Primary inertia-driven roll	20	1.6	28	8.7
	30	1.7	30	9.3
	40	2.0	35	11
Secondary inertia-driven roll	20	3.7	66	20
	30	1.8	32	10
	40	2.2	39	12

.

Table. 4.2   Critical condition for the onset of the primary inertia-driven vortex roll for H = 20-40 mm with heated disk

Separation Distance (H, mm)	ΔT (°C)	Flowrate (Q_j,SLPM)	Re_j	Re_n	Ra	Gr/Re_j^2	Gr/Re_n^2
20.0	5	1.8	10	32	3,758	54.38	5.26
	10	2.5	14	44	7,516	56.38	5.45
	15	3.0	17	53	11,274	58.73	5.68
	20	3.2	18	57	15,032	68.83	6.65
	25	3.4	19	60	18,790	76.21	7.37
30.0	1	2.1	12	37	2,536	26.97	2.61
	2	2.2	12	39	5,073	49.14	4.75
	3	2.3	13	41	7.610	67.45	6.52
	4	2.3	13	41	10,146	89.93	8.69
	5	2.4	13	43	12,683	103.24	9.99
	7	2.5	14	44	17,757	133.20	12.88
	10	2.6	14	46	25,367	175.93	17.02
	15	2.9	16	51	38,051	212.12	20.52
	20	3.1	17	55	50,734	247.51	23.93
	25	3.3	18	59	63,418	273.03	26.41

Table. 4.2   Continued

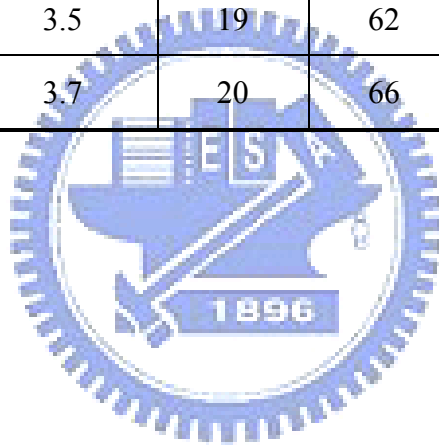| Separation Distance (H, mm)	ΔT (°C)	Flowrate $(Q_j, SLPM)$	Re_j	Re_n	Ra	Gr/Re_j^2	Gr/Re_n^2
	1	2.3	13	41	6,013	53.29	5.15
	2	2.4	13	43	12,026	97.89	9.46
	3	2.5	14	44	18,039	135.32	13.09
	4	2.6	14	46	24,052	166.81	16.13
40.0	5	2.8	15	50	30,065	179.79	17.38
	10	3.1	17	55	60,130	293.35	28.37
	15	3.3	18	59	90,195	388.32	37.56
	20	3.5	19	62	120,260	460.26	44.52
	25	3.7	20	66	150,325	514.81	49.79

Table. 4.3   Critical condition for the onset of the primary and secondary inertia-driven vortex roll without showerhead for H = 20-40 mm with disk unheated (Ra=0)

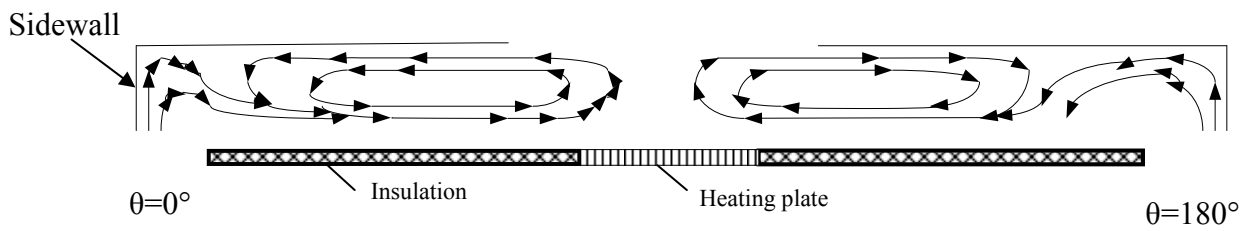|	Separation Distance (H, mm)	Flowrate (Q_j,SLPM)	Re_n
Primary inertia-driven roll	20	1.5	27
	30	1.6	28
	40	1.8	32
Secondary inertia-driven roll	20	2.0	35
	30	1.8	32
	40	2.2	39
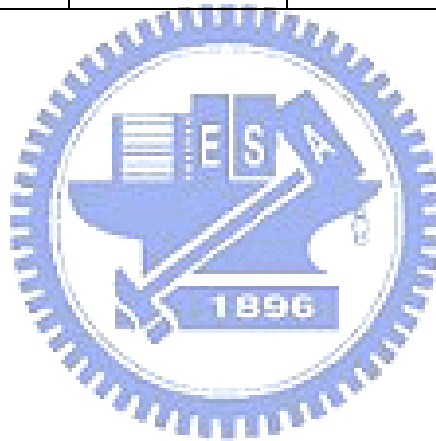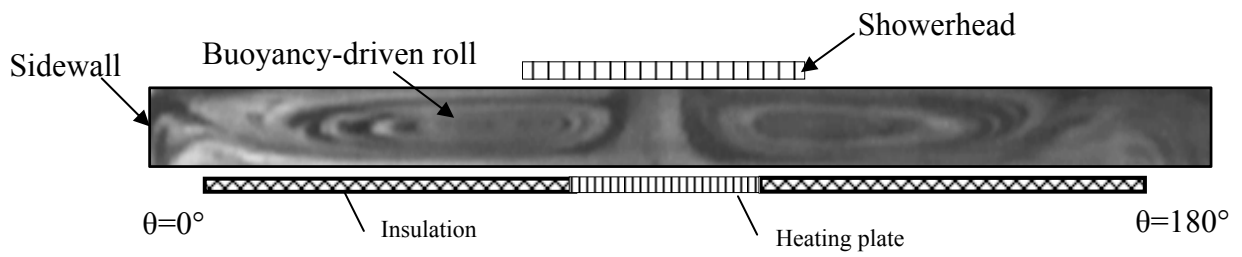
Fig. 4.1 Natural convection flow pattern in the chamber with H = 20.0mm for $Re_j = 0$ ($Q_j =$ 0 slpm) and Ra = 18,790 ($\Delta T = 25\,^{\circ}\mathrm{C}$) for (a) side view flow photo taken at the cross plane θ=0° & 180° and (b) the corresponding schematically sketched cross plane vortex flow.
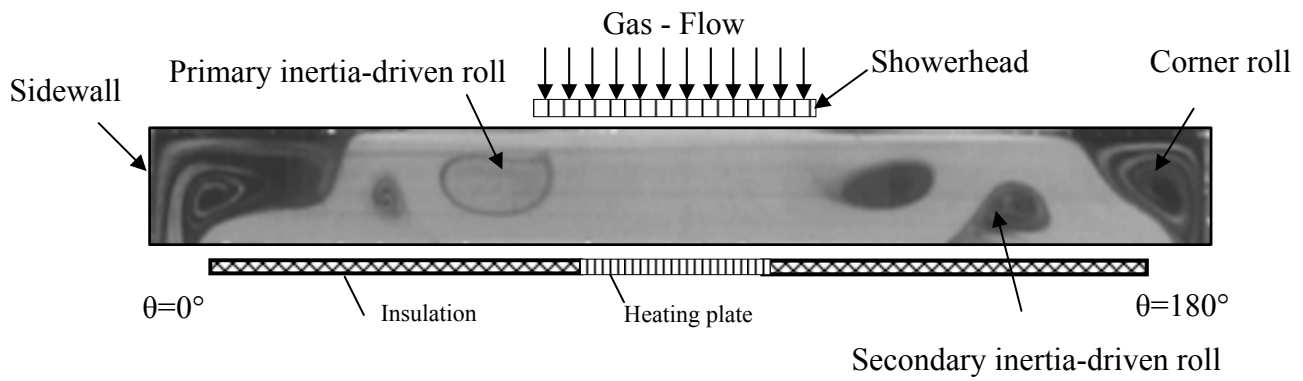
(a)
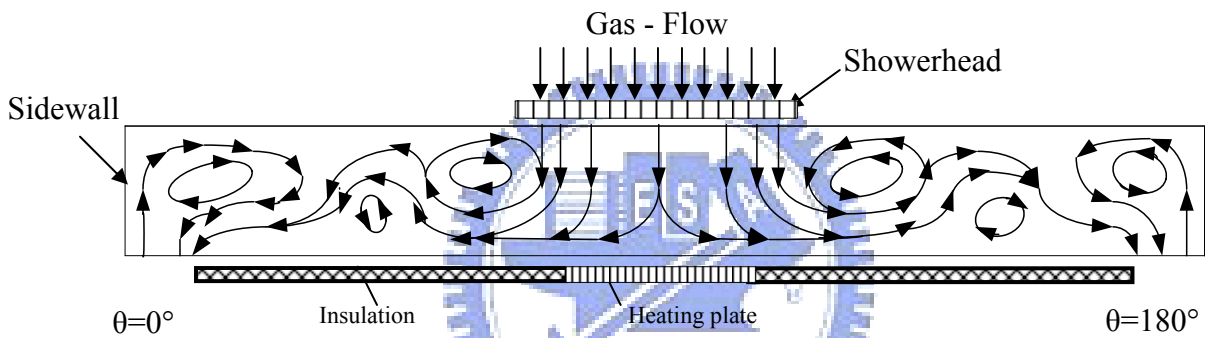
(b)

Fig. 4.2 Inertia driven flow pattern in the chamber with H = 30.0mm for $Re_n = 89$, $Re_j = 28$ ($Q_j = 5.0$ slpm) and Ra = 0 (ΔT = 0℃) for (a) side view flow photo taken at the cross plane θ=0° & 180° and (b) the corresponding schematically sketched cross plane vortex flow.
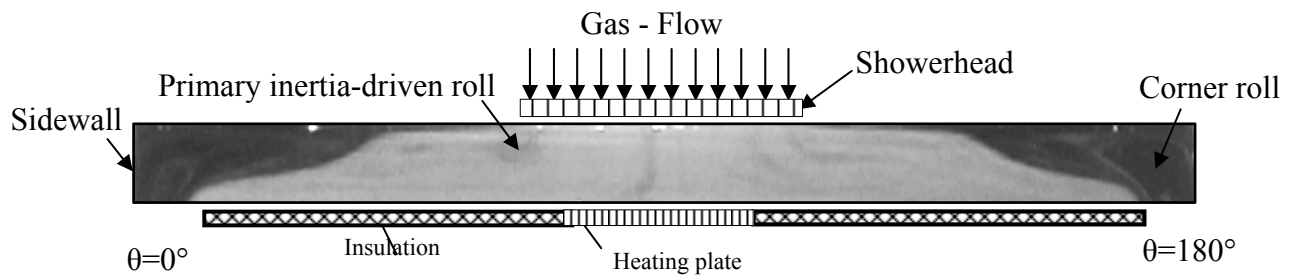
(a) H = 20.0 mm
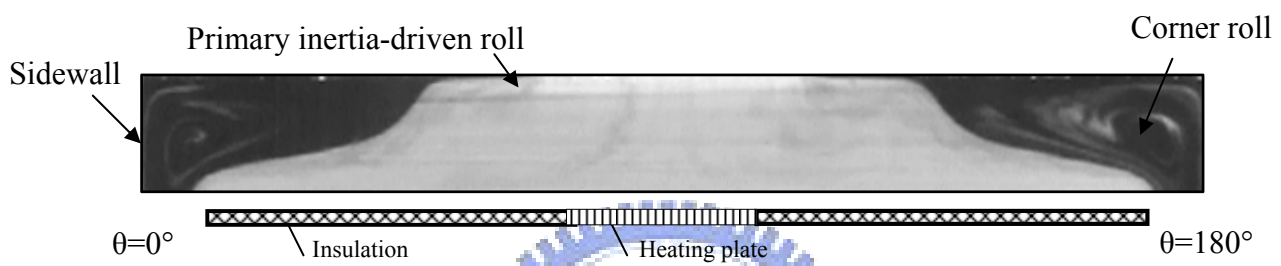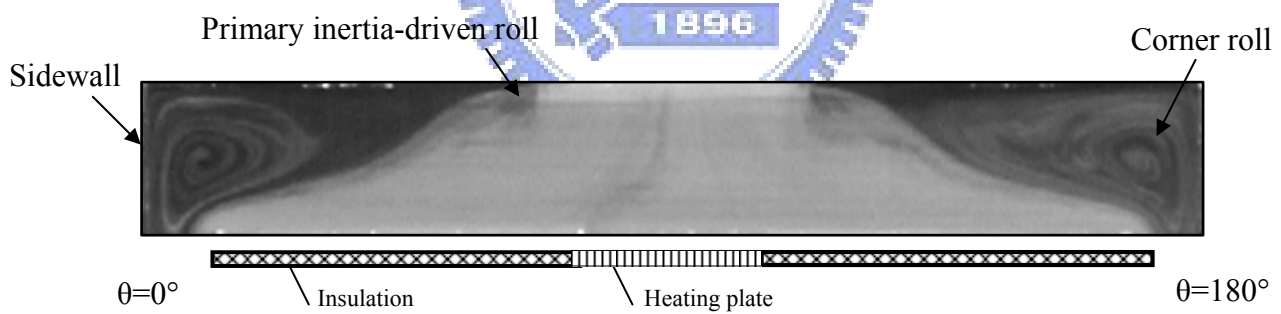

(b) H = 30.0 mm

(c) H = 40.0 mm

Fig. 4.3 Side view flow photos taken at the cross plane $\theta=0°$ & $180°$ at $Re_j = 14$ ($Q_j = 2.0$ slpm, $Re_n = 35$) and $\Delta T=0℃$ (Ra=0) for (a) H = 20.0 mm, (b) H = 30.0 mm and (b) H = 40.0 mm.

(a) H = 20.0 mm

(b) H = 30.0 mm

(c) H = 40.0 mm

Fig. 4.4   Side view flow photos taken at the cross plane θ=0° & 180° at Re_j = 22 (Q_j = 4.0 slpm, Re_n = 71) and ΔT = 0℃ (Ra = 0) for (a) H = 20.0 mm, (b) H = 30.0 mm and (b) H = 40.0 mm.
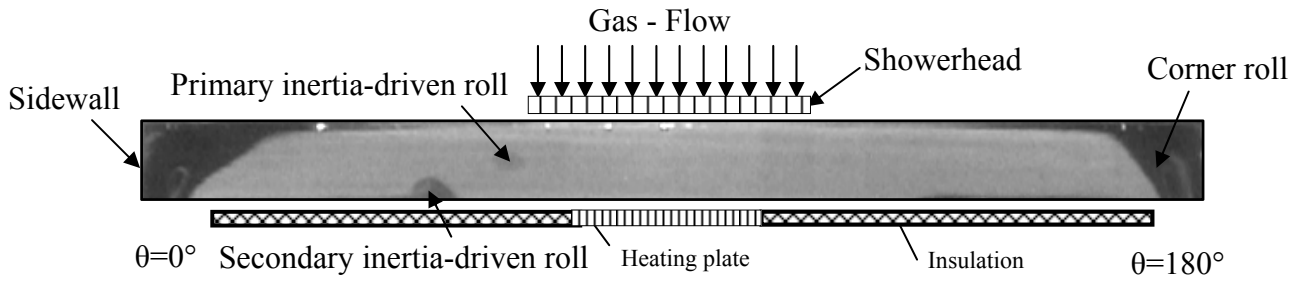
(a) H = 20.0 mm

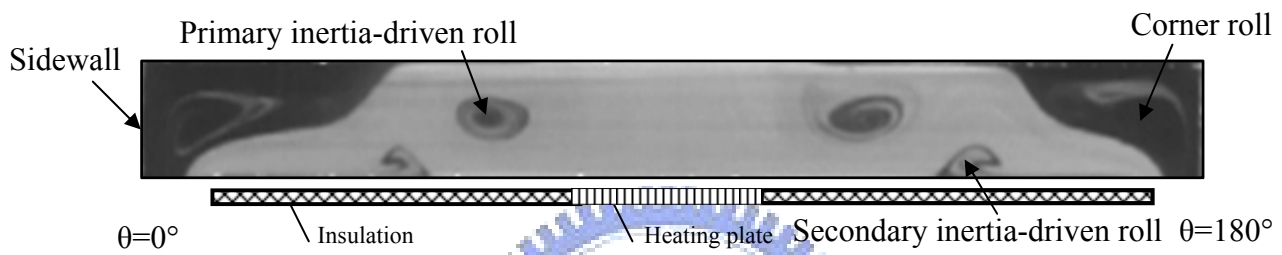

(b) H = 30.0 mm

(c) H = 40.0 mm

Fig. 4.5   Side view flow photos taken at the cross plane $\theta = 0°$ & $180°$ at $Re_j = 11$ ($Q_j = 2.0$ slpm, $Re_n = 35$), and $\Delta T = 10°C$ for (a) H = 20.0 mm (Ra = 7,516), (b) H = 30.0 mm (Ra = 25,367), and (c) H = 40.0 mm (Ra = 60,130).
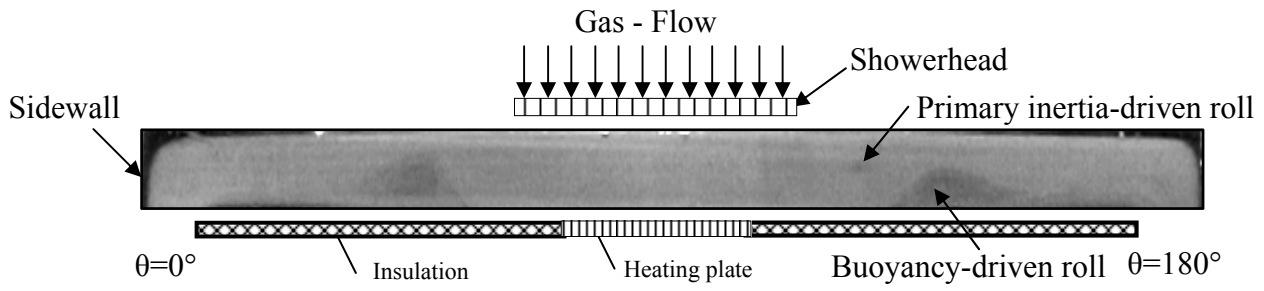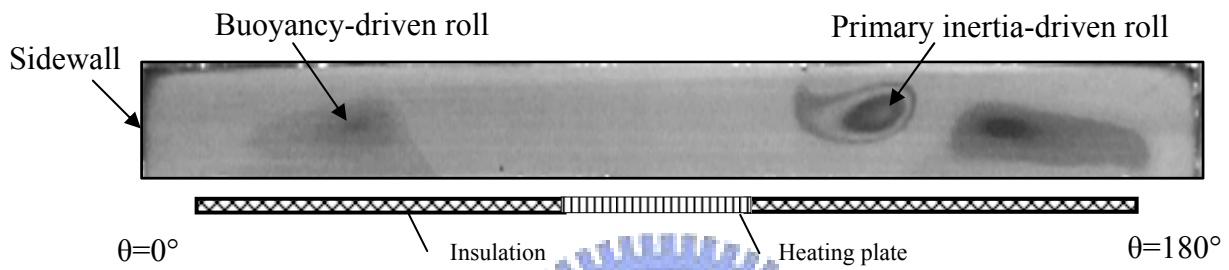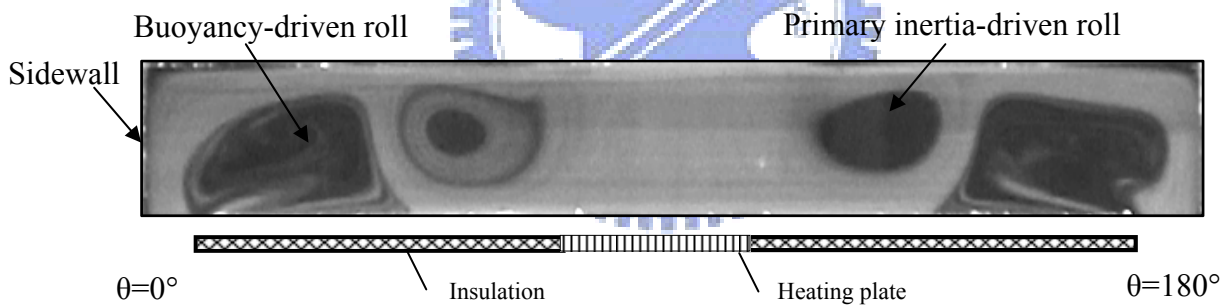
Fig. 4.6 Side view flow photos taken at the cross plane θ = 0° & 180° at Re_j = 28 (Q_j = 5.0 slpm, Re_n = 89), and ΔT = 10℃ for (a) H = 20.0 mm (Ra = 7,516), (b) H = 30.0 mm (Ra = 25,367), and (c) H = 40.0 mm (Ra = 60,130).
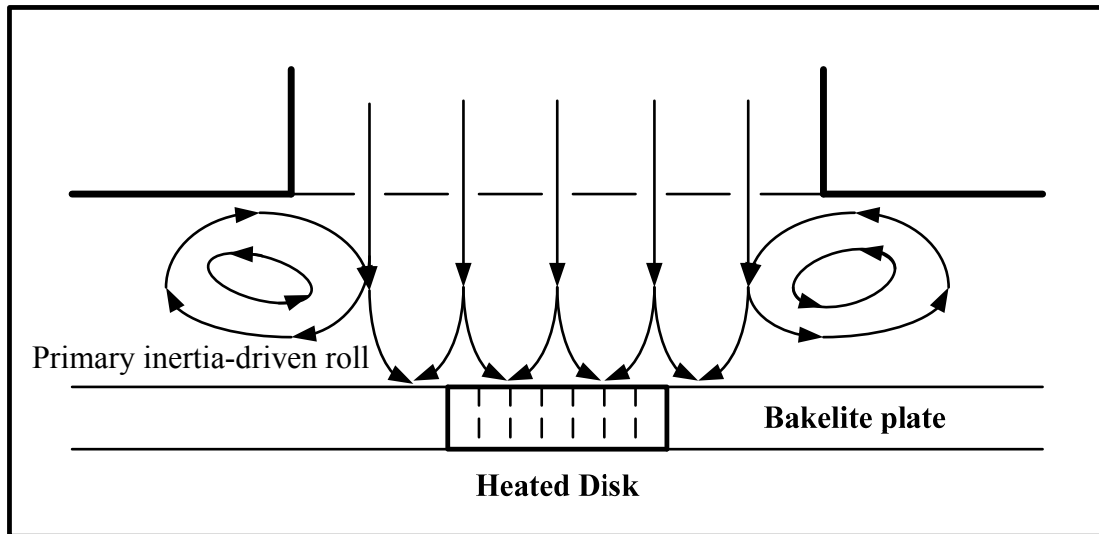
Fig. 4.7   Schematic illustration of the streamlines through the showerhead and impinging onto the heated disk.
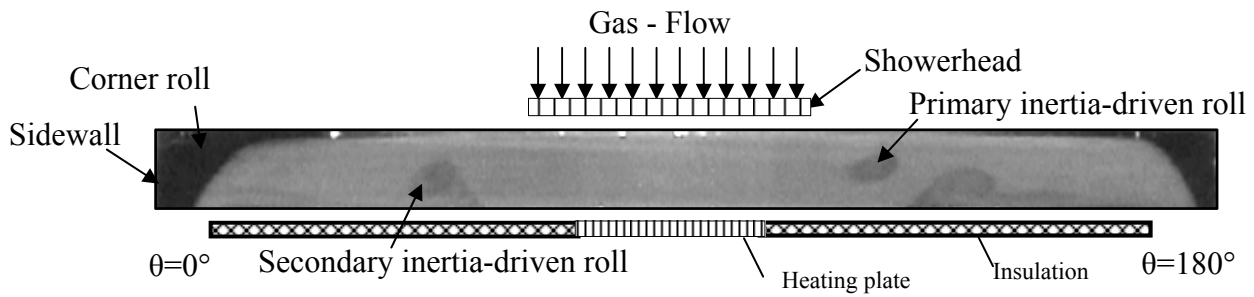
(a) H = 20.0 mm
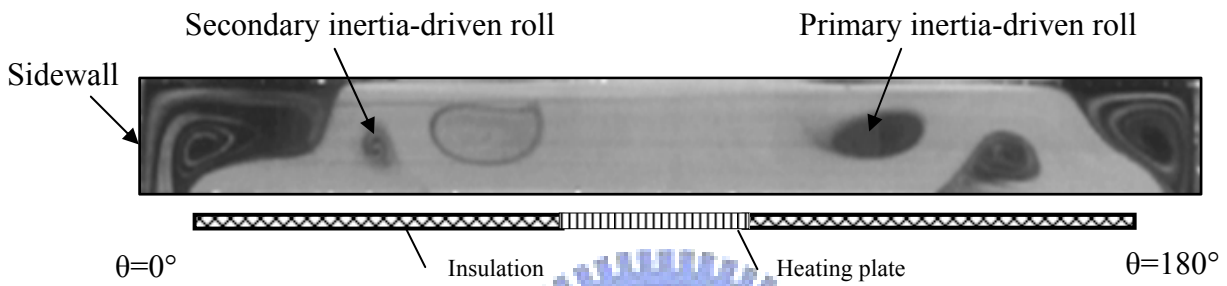
(b) H = 30.0 mm
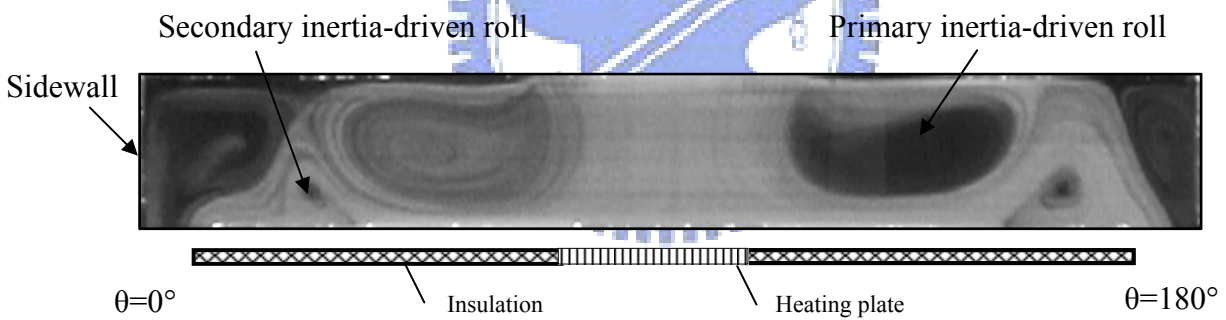
(c) H = 40.0 mm

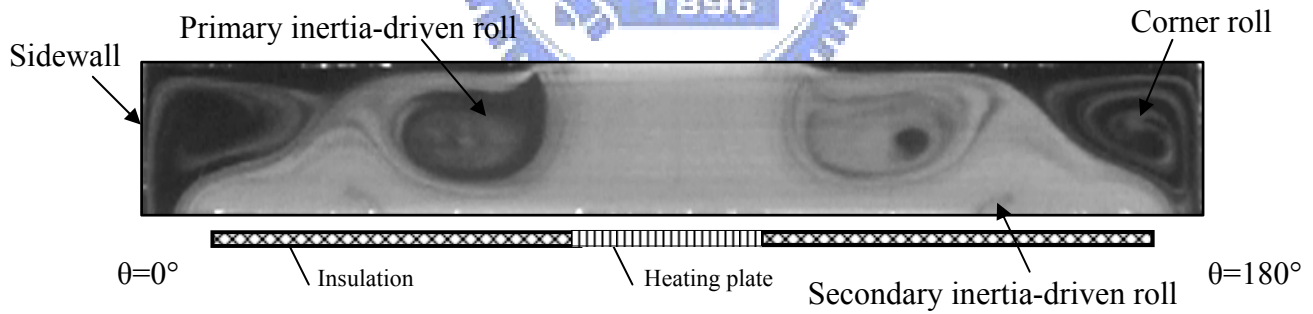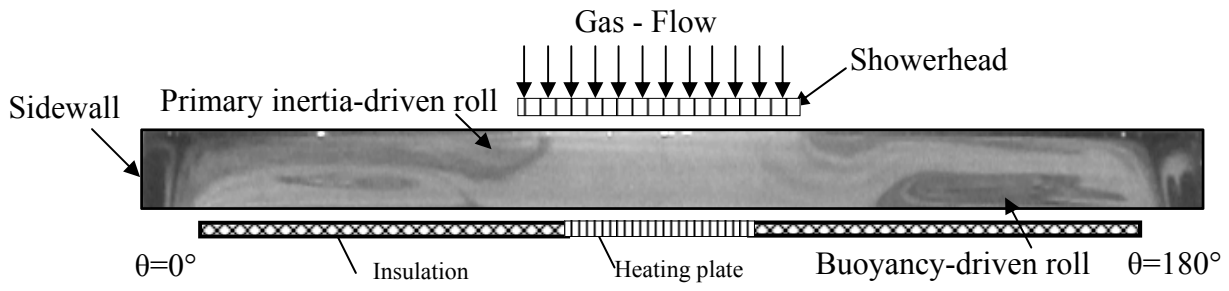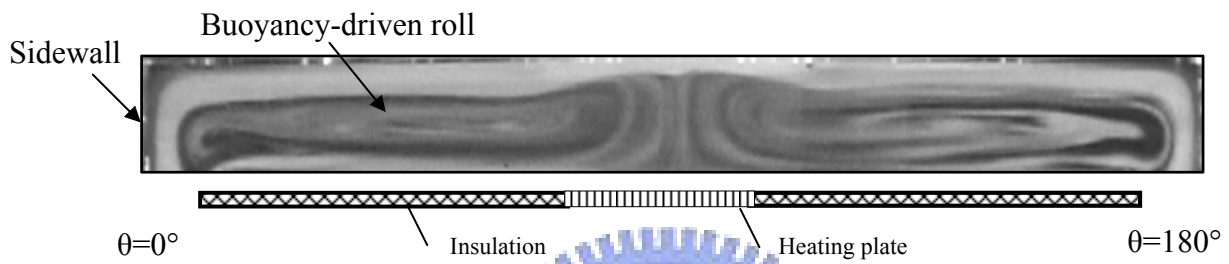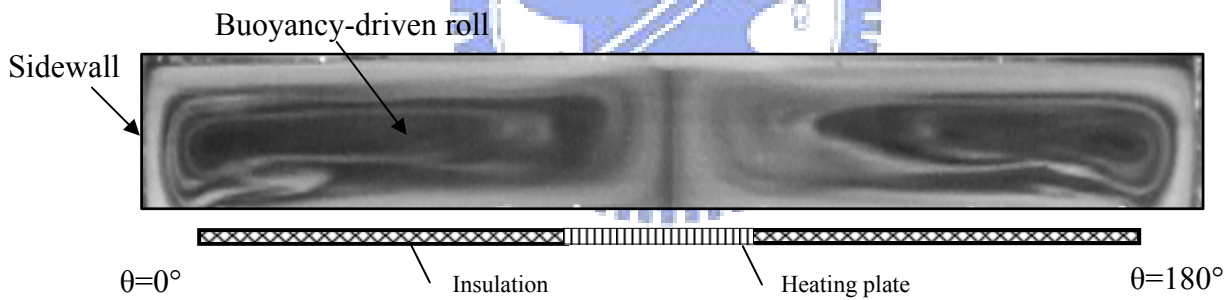Fig. 4.8   Side view flow photos taken at the cross plane $\theta = 0°$ & $180°$ at $Re_j = 28$ ($Q_j = 5.0$ slpm, $Re_n = 89$), and $\Delta T = 0℃$ for (a) H = 20.0 mm, (b) H = 30.0 mm, and (c) H = 40.0 mm.
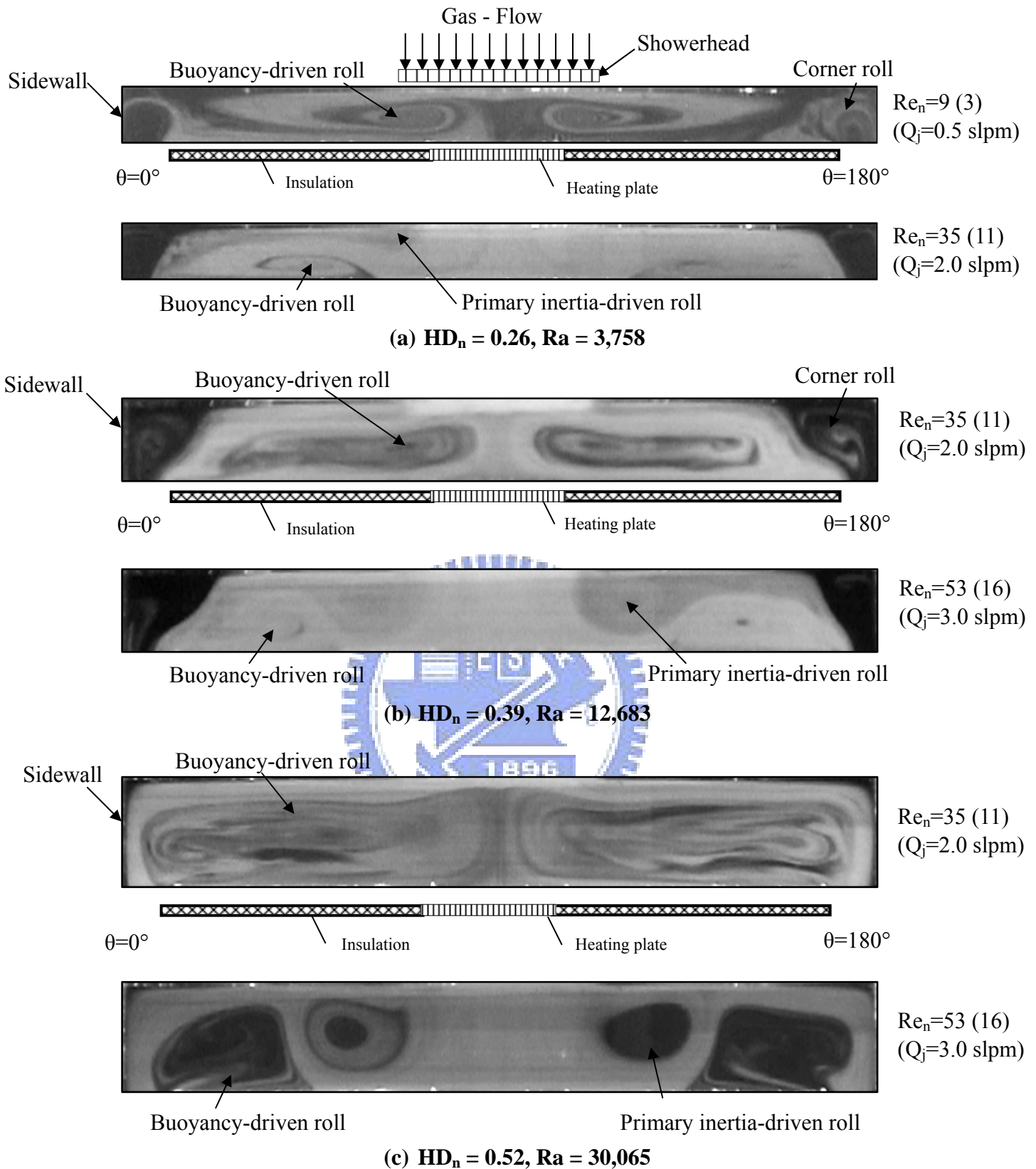
Fig. 4.9 Side view flow photos taken at the cross plane θ = 0° & 180° at ΔT = 5℃ steady
state for various Q_j (a) HD_n = 0.26, Ra = 3,758, (b) HD_n = 0.39, Ra = 12,683 and (c)
HD_n = 0.52, Ra = 30,065.

( ) : The number in the ( ) is the jet Reynolds number.

Fig. 4.10 Side view flow photos taken at the cross plane $\theta = 0°$ & $180°$ for various jet Reynolds numbers at Ra = 3,758 ($\Delta T = 5℃$) and H = 20.0 mm for Re_n = (a) 9, (b) 12, (c) 16, (d) 18, (e) 20, (f) 25, (g) 27, (h) 32, (i) 34, (j) 35, (k) 44, (l) 53, (m) 71 and (n) 89.

( ) : The number in the ( ) is the jet Reynolds number.

Fig. 4.10 Continued.

Fig. 4.11 Side view flow photos taken at the cross plane $\theta = 0°$ & $180°$ for various jet Reynolds numbers at Ra = 7,516 ($\Delta T = 10°C$) and H = 20.0 mm for Re_n = (a) 18, (b) 23, (c) 25, (d) 28, (e) 35, (f) 41, (g) 44, (h) 53, (i) 71 and (j) 89.

( ) : The number in the ( ) is the jet Reynolds number.

Fig. 4.12 Side view flow photos taken at the cross plane θ = 0° & 180° for various jet Reynolds numbers at Ra = 11,274 (ΔT = 15℃) and H = 20.0 mm for Re_n = (a) 18, (b) 27, (c) 28, (d) 30, (e) 34, (f) 35, (g) 44, (h) 53, (i) 57, (j) 59, (k) 62, (l) 71 and (m) 89.

( ) : The number in the ( ) is the jet Reynolds number.

(j) Primary inertia-driven roll — $Re_n=59$ (18) ($Q_j=3.3$ slpm) Steady — Buoyancy-driven roll

(k) Primary inertia-driven roll — $Re_n=62$ (19) ($Q_j=3.5$ slpm) Steady — Buoyancy-driven roll

(l) Primary inertia-driven roll — $Re_n=71$ (22) ($Q_j=4.0$ slpm) Steady — Buoyancy-driven roll

(m) Primary inertia-driven roll — $Re_n=89$ (28) ($Q_j=5.0$ slpm) Steady — Buoyancy-driven roll

Fig. 4.12   Continued.

Fig. 4.13 Side view flow photos taken at the cross plane θ = 0° & 180° for various jet Reynolds numbers at Ra = 15,032 (ΔT = 20℃) and H = 20.0 mm for Re_n = (a) 18, (b) 27, (c) 30, (d) 34, (e) 35, (f) 37, (g) 44, (h) 53, (i) 57, (j) 62, (k) 71 and (l) 89. ( ) : The number in the ( ) is the jet Reynolds number.

(j)   Primary inertia-driven roll Re_n=62 (19) (Q_j=3.5 slpm) Steady

Buoyancy-driven roll

(k)   Primary inertia-driven roll Re_n=71 (22) (Q_j=4.0 slpm) Steady

Buoyancy-driven roll

(l)   Primary inertia-driven roll Re_n=89 (28) (Q_j=5.0 slpm) Steady
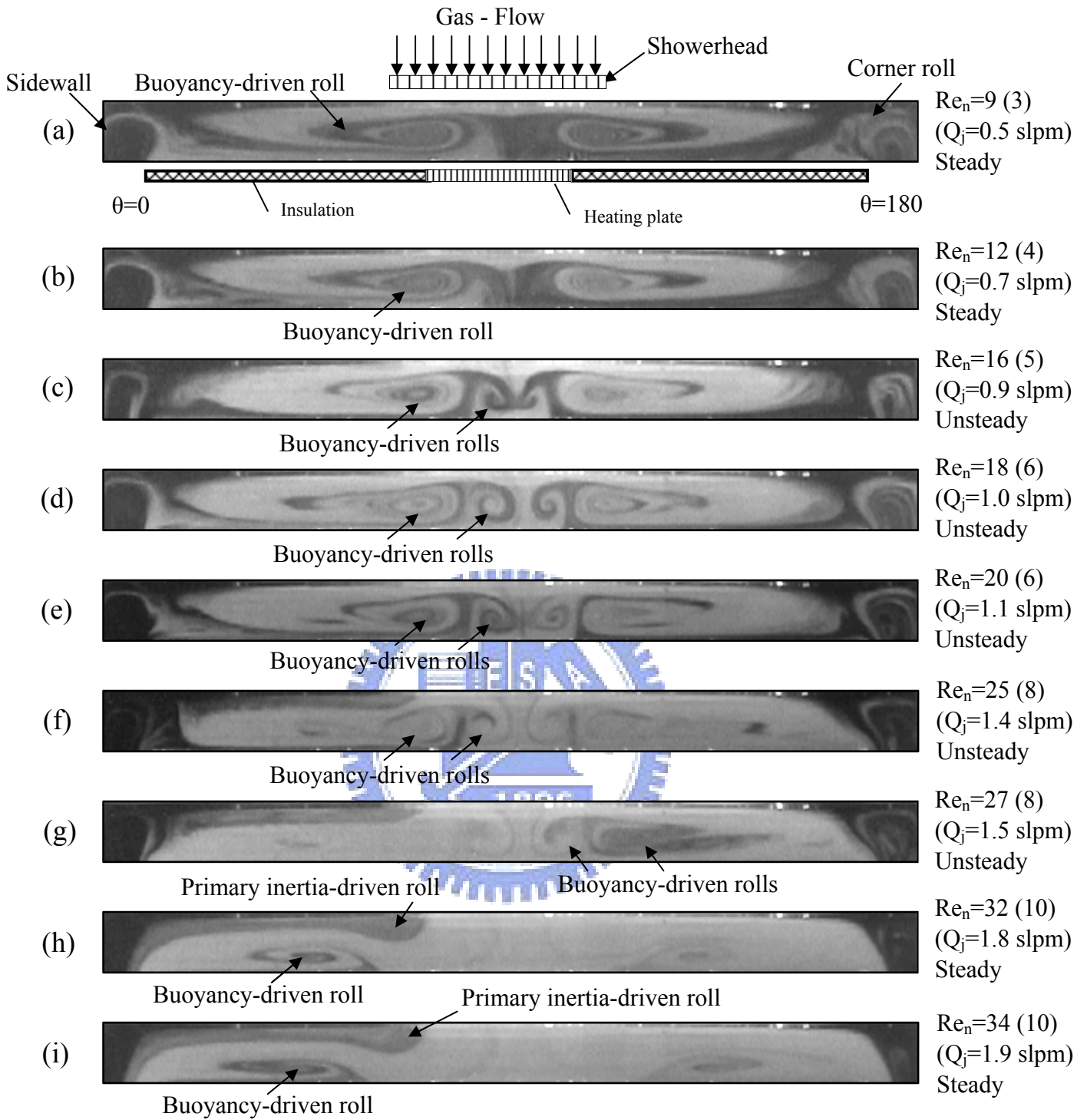
Buoyancy-driven roll
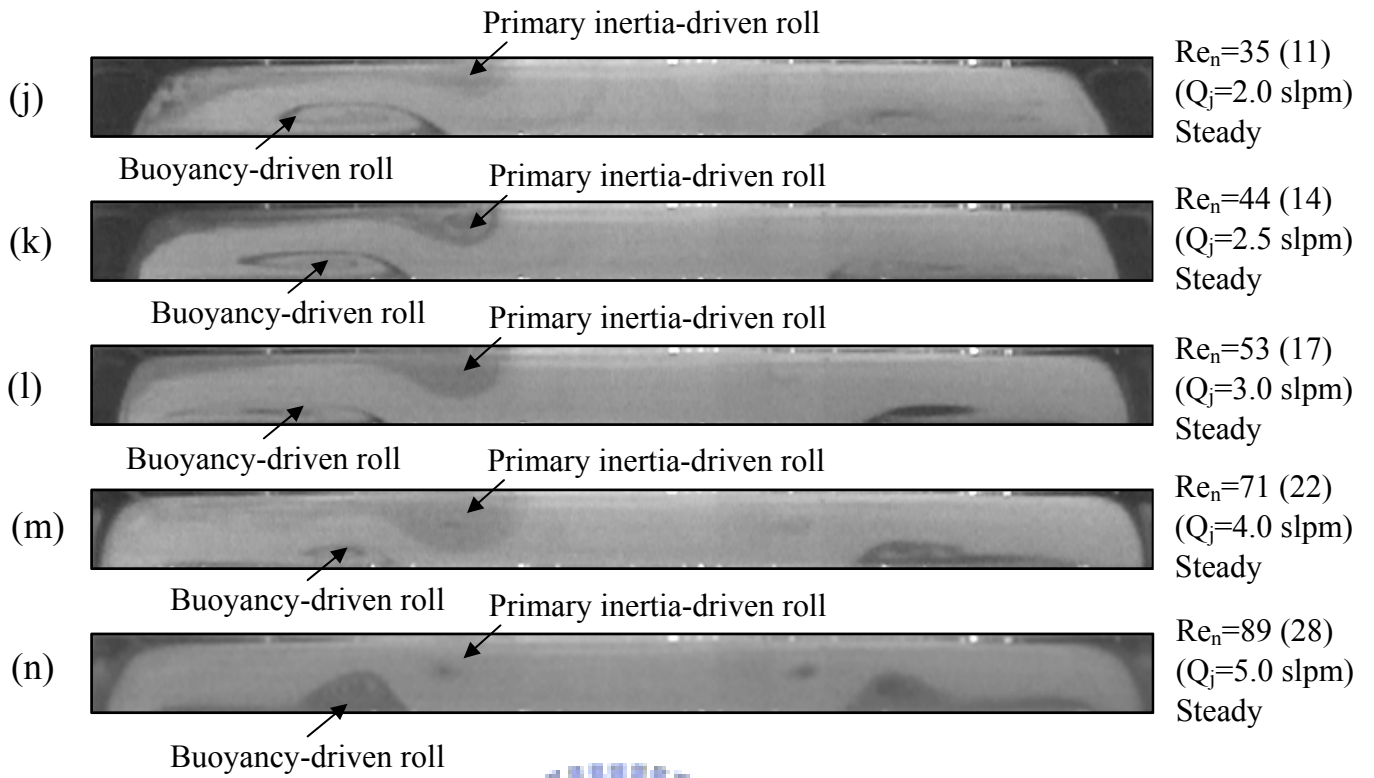
Fig. 4.13   Continued.

Fig. 4.14 Side view flow photos taken at the cross plane $\theta = 0°$ & $180°$ for various jet Reynolds numbers at Ra = 18,790 ($\Delta T = 25℃$) and H = 20.0 mm for Re_n = (a) 18, (b) 27, (c) 35, (d) 37, (e) 39, (f) 41, (g) 44, (h) 53, (i) 60, (j) 62, (k) 64, (l) 71, (m) 80 and (n) 89.

( ) : The number in the ( ) is the jet Reynolds number.

(j)　Buoyancy-driven roll　Primary inertia-driven roll　$Re_n=62$ (19) ($Q_j=3.5$ slpm) Steady

(k)　Buoyancy-driven roll　Primary inertia-driven roll　$Re_n=64$ (20) ($Q_j=3.6$ slpm) Steady

(l)　Buoyancy-driven roll　Primary inertia-driven roll　$Re_n=71$ (22) ($Q_j=4.0$ slpm) Steady

(m)　Buoyancy-driven roll　Primary inertia-driven roll　$Re_n=80$ (25) ($Q_j=4.5$ slpm) Steady

(n)　Buoyancy-driven roll　Primary inertia-driven roll　$Re_n=89$ (28) ($Q_j=5.0$ slpm) Steady

Fig. 4.14　Continued.

58
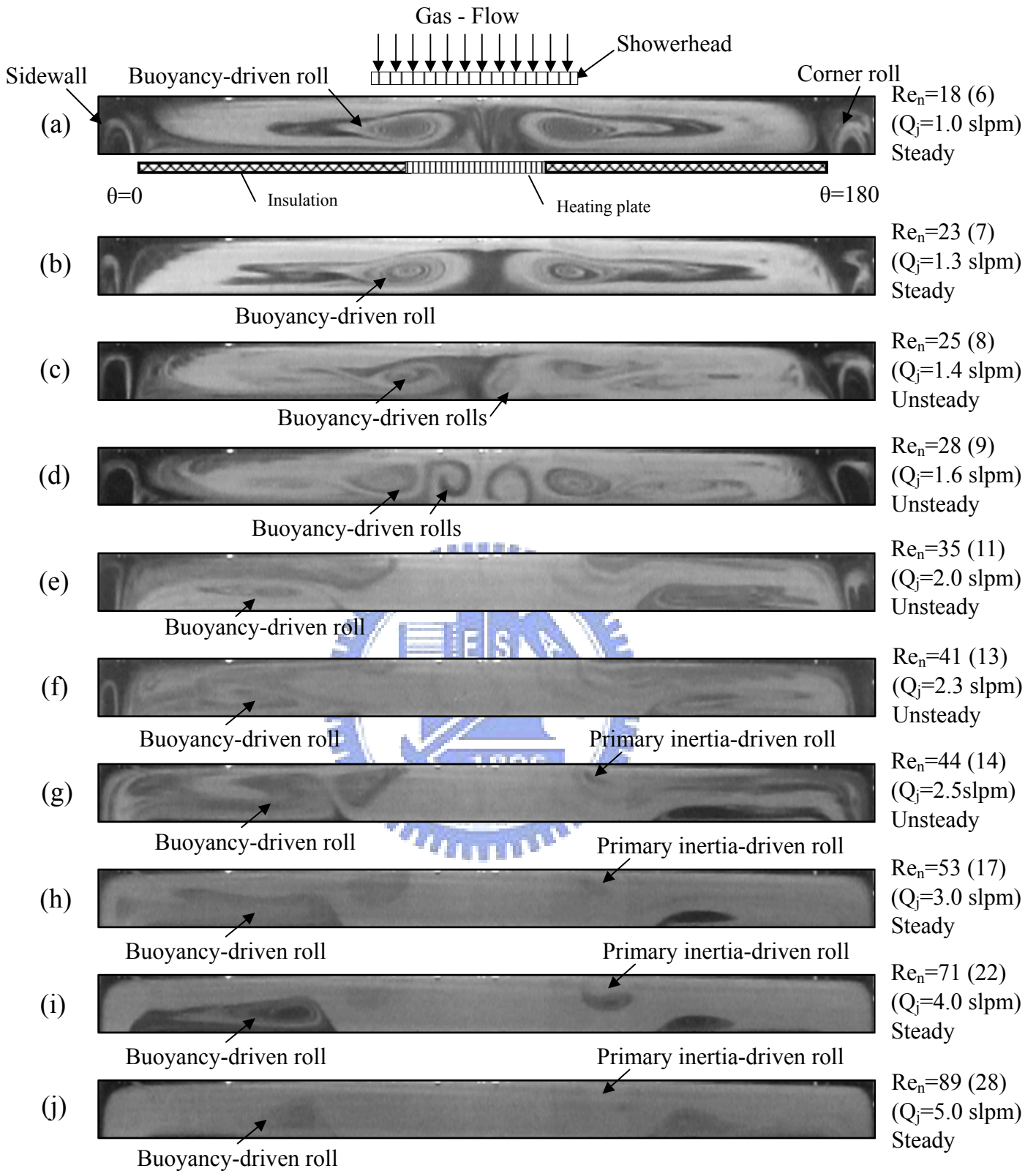
Fig. 4.15 Side view flow photos taken at the cross plane θ = 0° & 180° for various jet Reynolds numbers at Ra = 2,536 (ΔT = 1℃) and H = 30.0 mm for Re_n = (a) 27, (b) 30, (c) 35, (d) 37, (e) 39, (f) 44, (g) 53, (h) 71 and (i) 89.

( ) : The number in the ( ) is the jet Reynolds number.

Corner roll

Inertia-driven roll

$Re_n=71$ (22)
$(Q_j=4.0$ slpm)
Steady

(h)

Buoyancy-driven roll

Inertia-driven roll

$Re_n=89$ (28)
$(Q_j=5.0$ slpm)
Steady

(i)

Buoyancy-driven roll

Fig. 4.15   Continued.

Fig. 4.16 Side view flow photos taken at the cross plane θ = 0° & 180° for various jet Reynolds numbers at Ra = 5073 (ΔT = 2℃) and H = 30.0 mm for Re_n = (a) 18, (b) 34, (c) 35, (d) 37, (e) 39, (f) 44, (g) 53, (h) 71 and (i) 89.
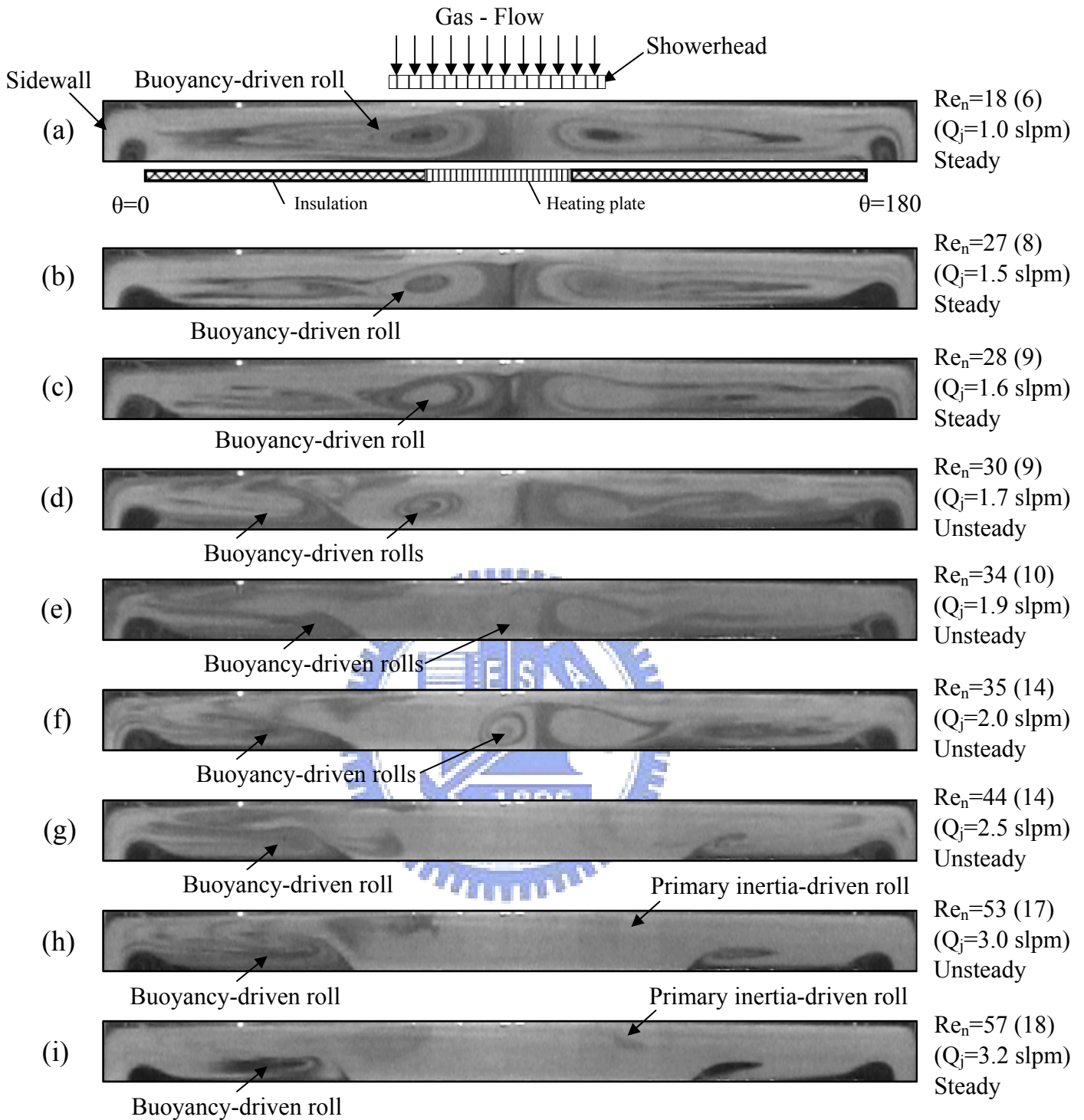
( ) : The number in the ( ) is the jet Reynolds number.

(h) Corner roll / Inertia-driven roll / Buoyancy-driven roll — $Re_n=71$ (22) ($Q_j=4.0$ slpm) Steady

(i) Inertia-driven roll / Buoyancy-driven roll — $Re_n=89$ (28) ($Q_j=5.0$ slpm) Steady
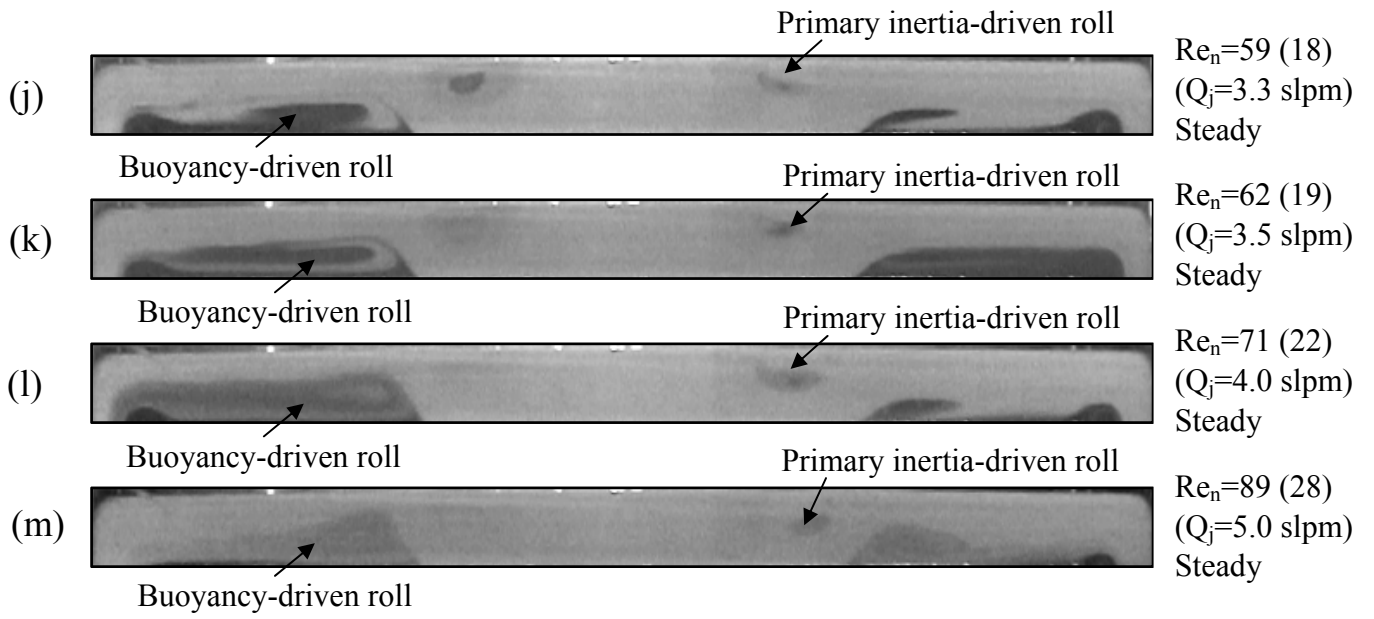
Fig. 4.16   Continued.

Fig. 4.17 Side view flow photos taken at the cross plane θ = 0° & 180° for various jet Reynolds numbers at Ra = 7,610 (ΔT = 3℃) and H = 30.0 mm for Re_j = (a) 35, (b) 37, (c) 39, (d) 41, (e) 43, (f) 44, (g) 53, (h) 71 and (i) 89.

( ) : The number in the ( ) is the jet Reynolds number.

(h)   Corner roll   Inertia-driven roll $Re_n=71$ (22) ($Q_j=4.0$ slpm) Steady

Buoyancy-driven roll

(i)   Inertia-driven roll $Re_n=89$ (28) ($Q_j=5.0$ slpm) Steady
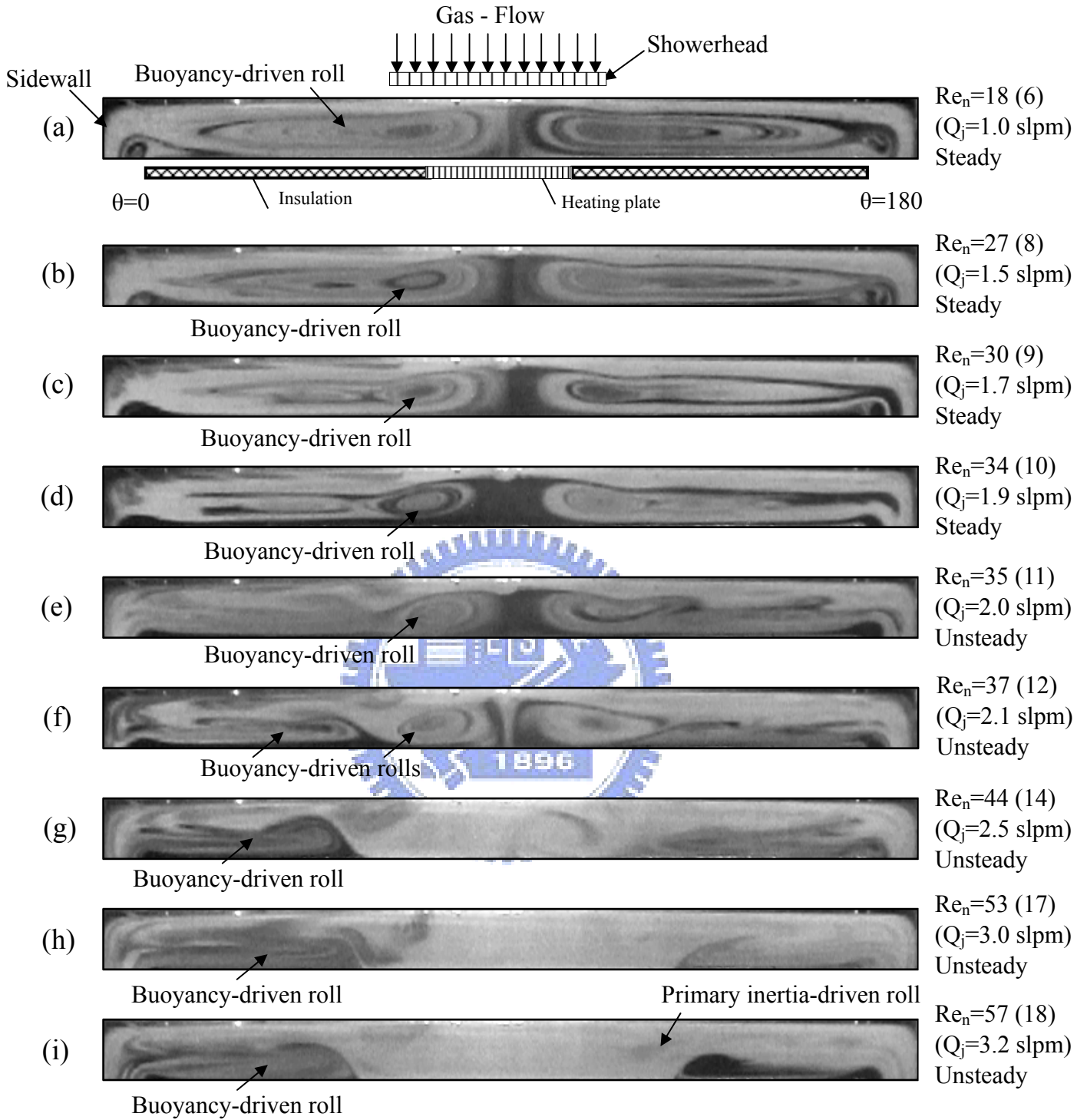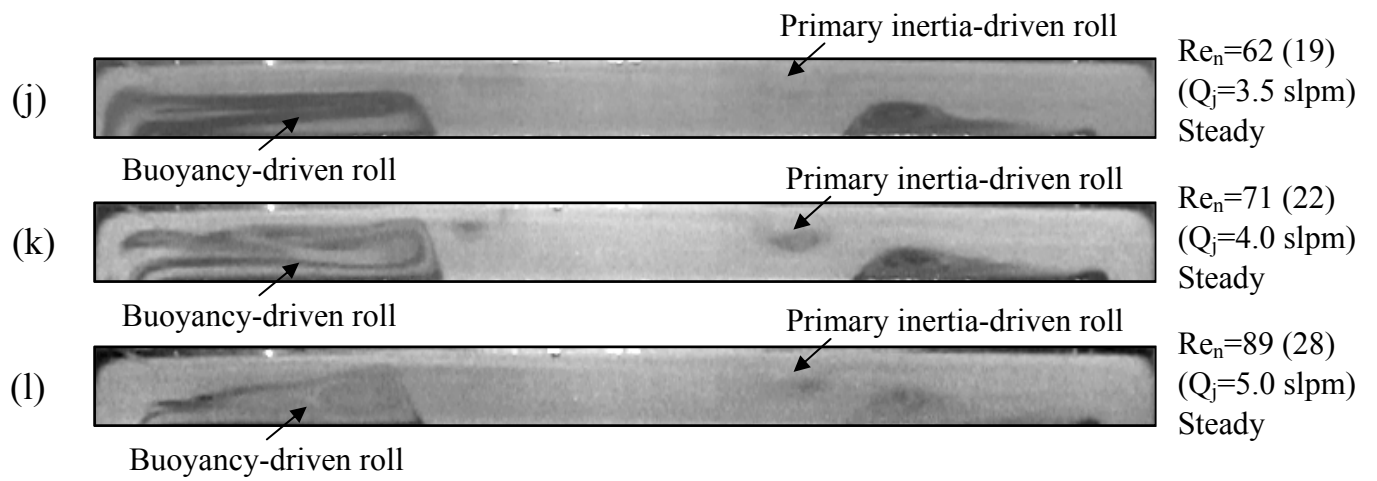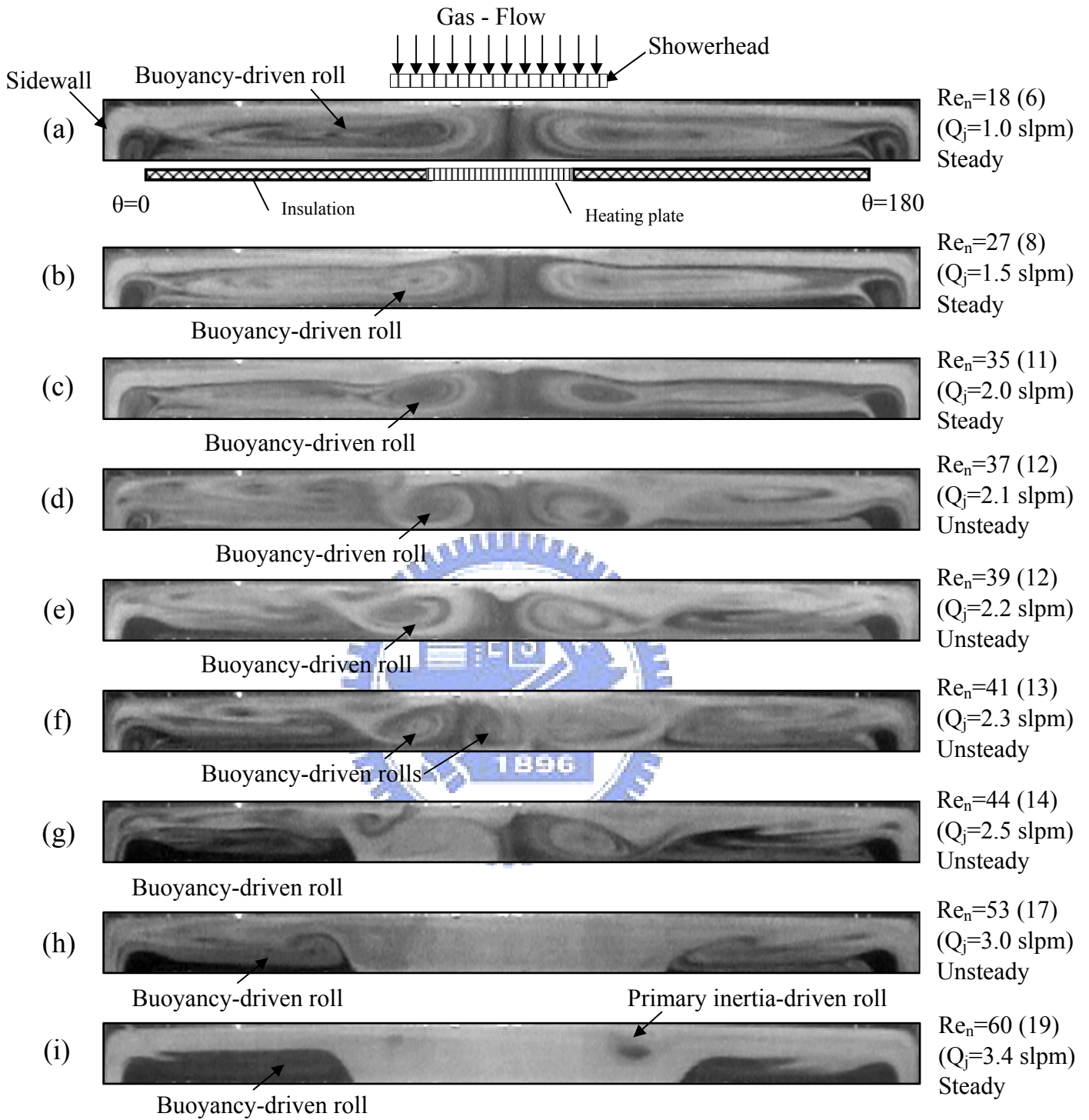
Buoyancy-driven roll

Fig. 4.17   Continued.

Fig. 4.18 Side view flow photos taken at the cross plane $\theta = 0°$ & $180°$ for various jet Reynolds numbers at Ra = 10,146 ($\Delta T = 4°C$) and H = 30.0 mm for Re_n = (a) 18, (b) 35, (c) 39, (d) 43, (e) 44, (f) 46, (g) 48, (h) 50, (i) 53, (j) 71 and (k) 89.

( ) : The number in the ( ) is the jet Reynolds number.

Corner roll — Inertia-driven roll

(h) $Re_n=50$ (15)
$(Q_j=2.8$ slpm)
Steady

Buoyancy-driven roll — Inertia-driven roll

(i) $Re_n=53$ (17)
$(Q_j=3.0$ slpm)
Steady

Inertia-driven roll

(j) $Re_n=71$ (22)
$(Q_j=4.0$ slpm)
Steady

Buoyancy-driven roll — Inertia-driven roll

(k) $Re_n=89$ (28)
$(Q_j=5.0$ slpm)
Steady

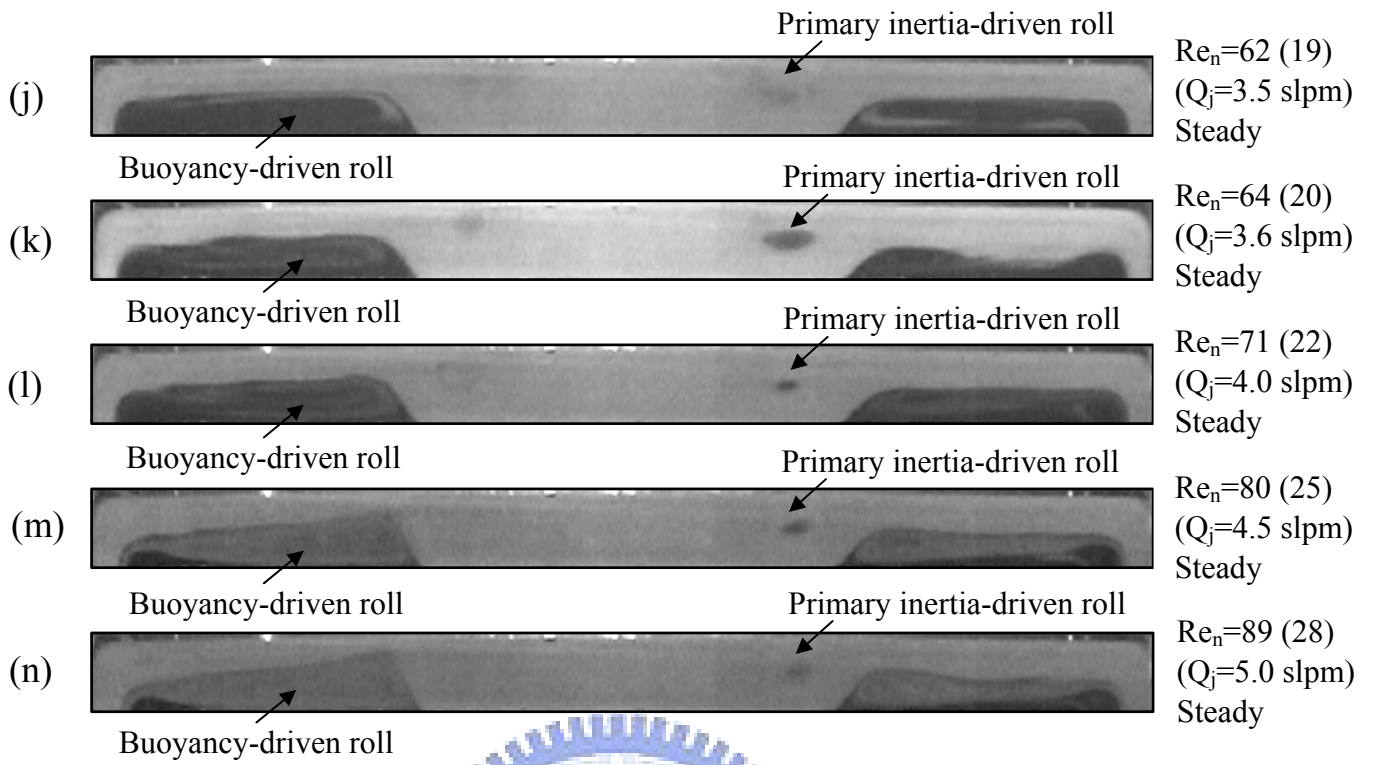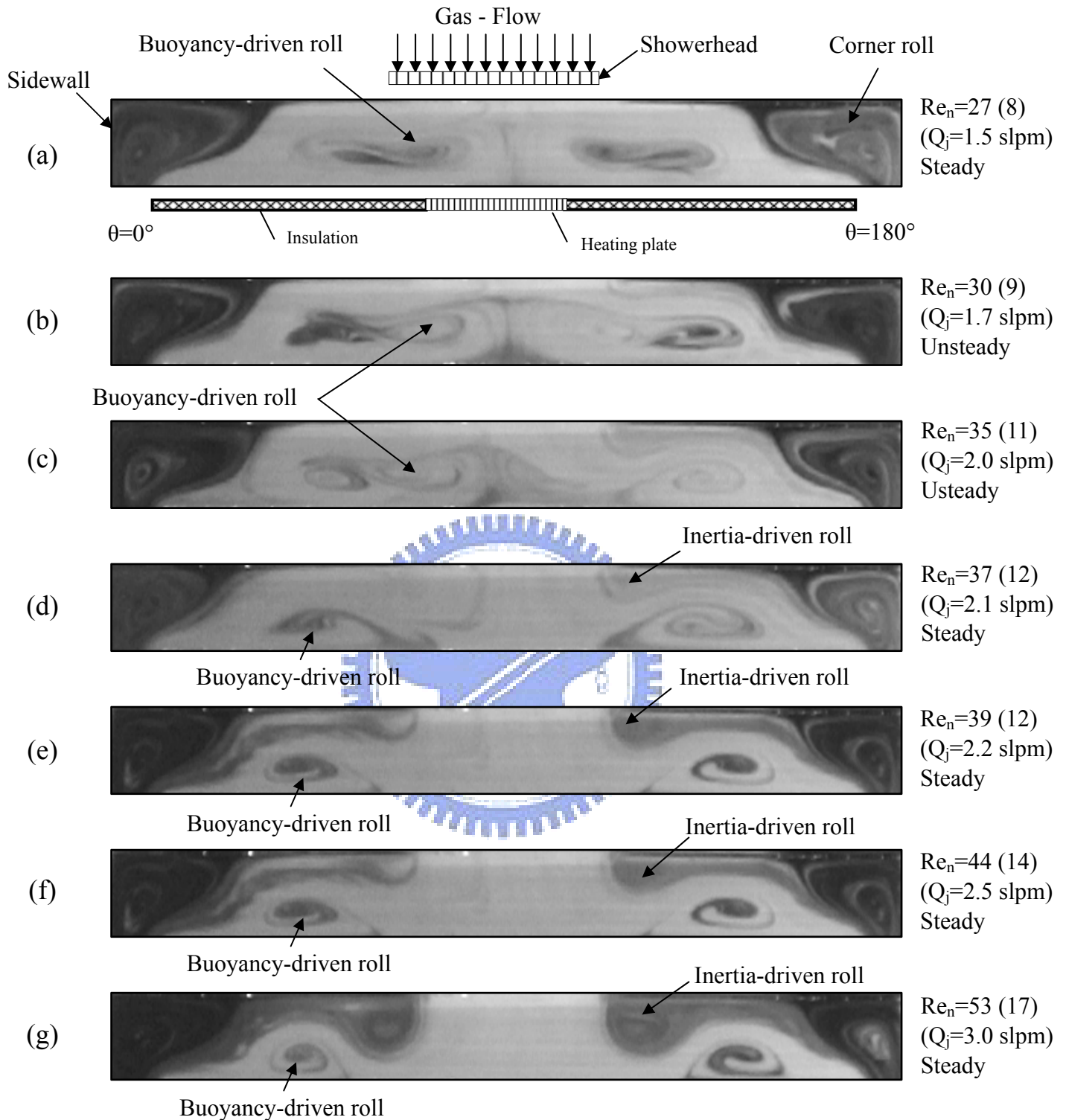Fig. 4.18   Continued.

66
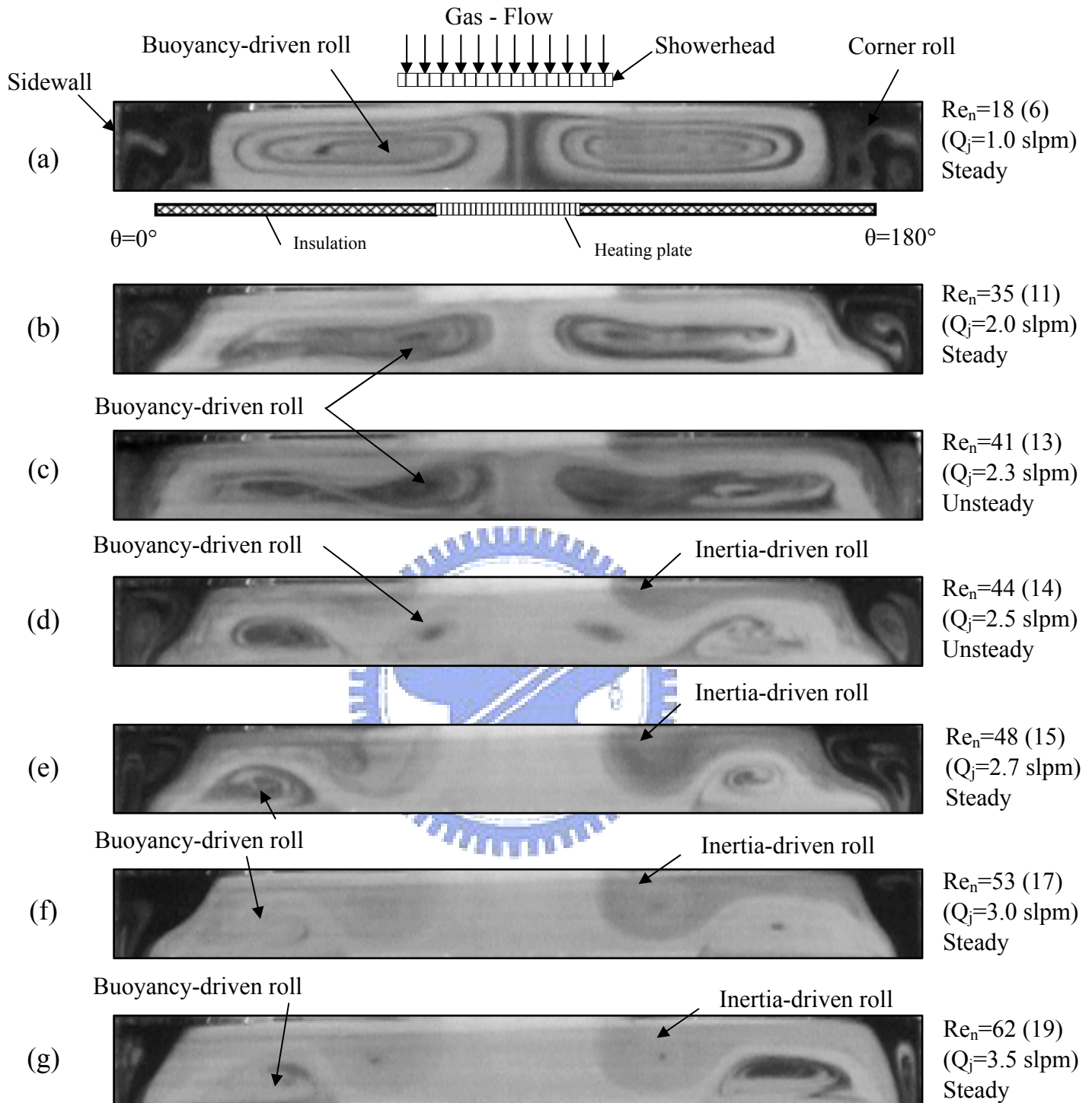
Fig. 4.19 Side view flow photos taken at the cross plane θ = 0° & 180° for various jet Reynolds numbers at Ra = 12,683 (ΔT = 5℃) and H = 30.0 mm for Re_n = (a) 18, (b) 35, (c) 41, (d) 44, (e) 48, (f) 53, (g) 62, (h) 71 and (i) 89.

( ) : The number in the ( ) is the jet Reynolds number.

Corner roll   Inertia-driven roll

(h) $Re_n=71$ (22) ($Q_j=4.0$ slpm) Steady

Buoyancy-driven roll   Inertia-driven roll
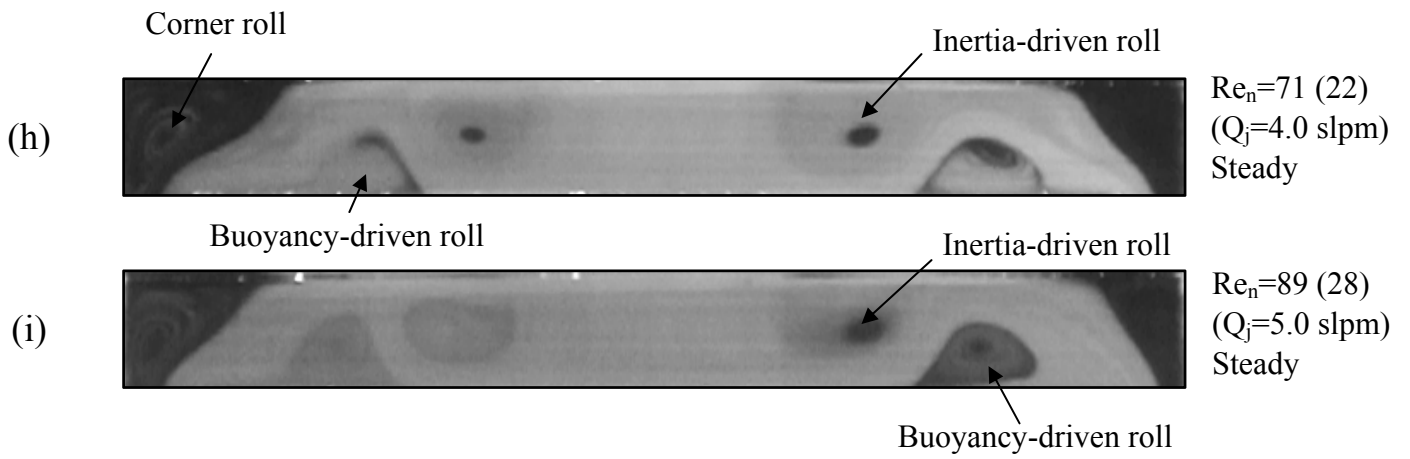
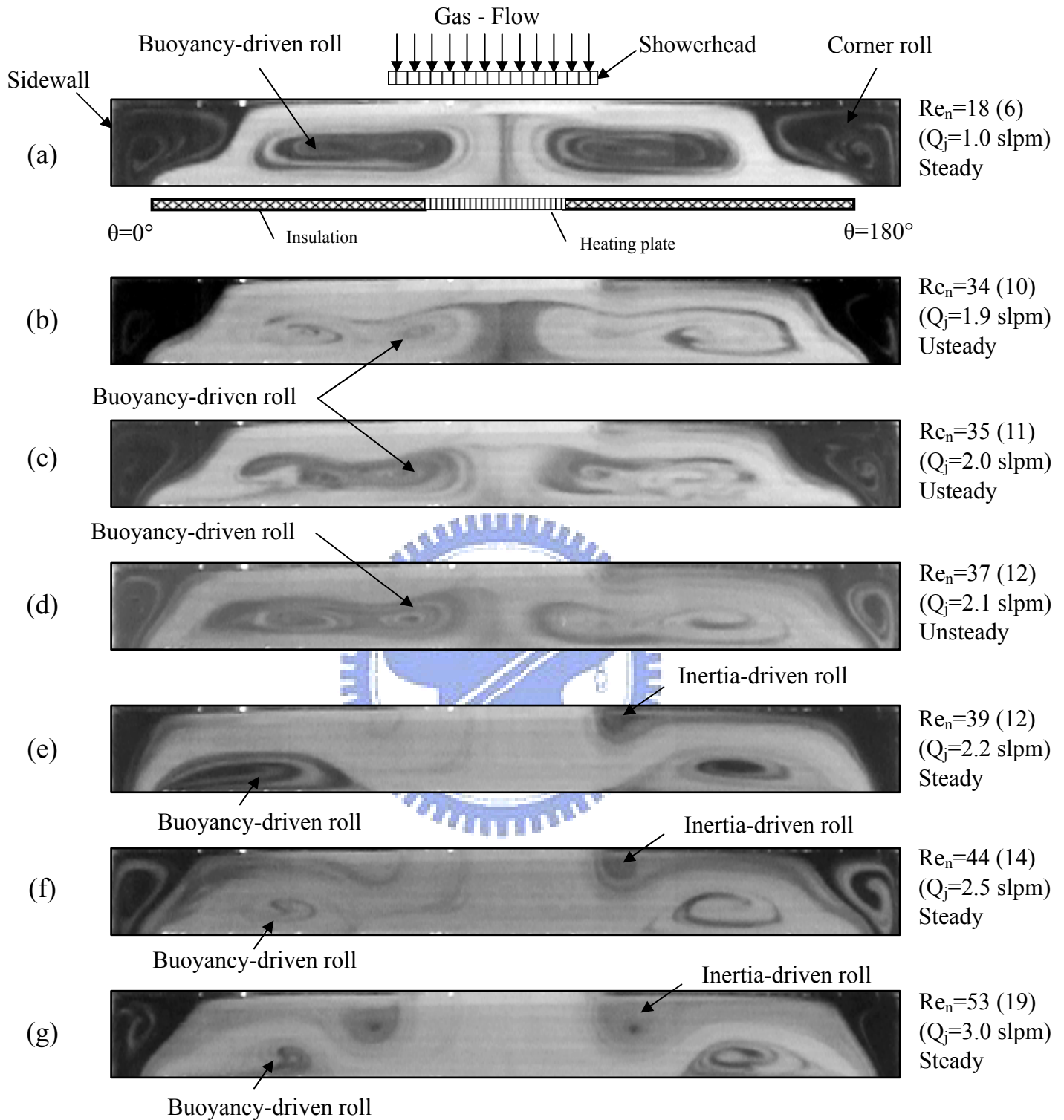(i) $Re_n=89$ (28) ($Q_j=5.0$ slpm) Steady

Fig. 4.19 Continued.
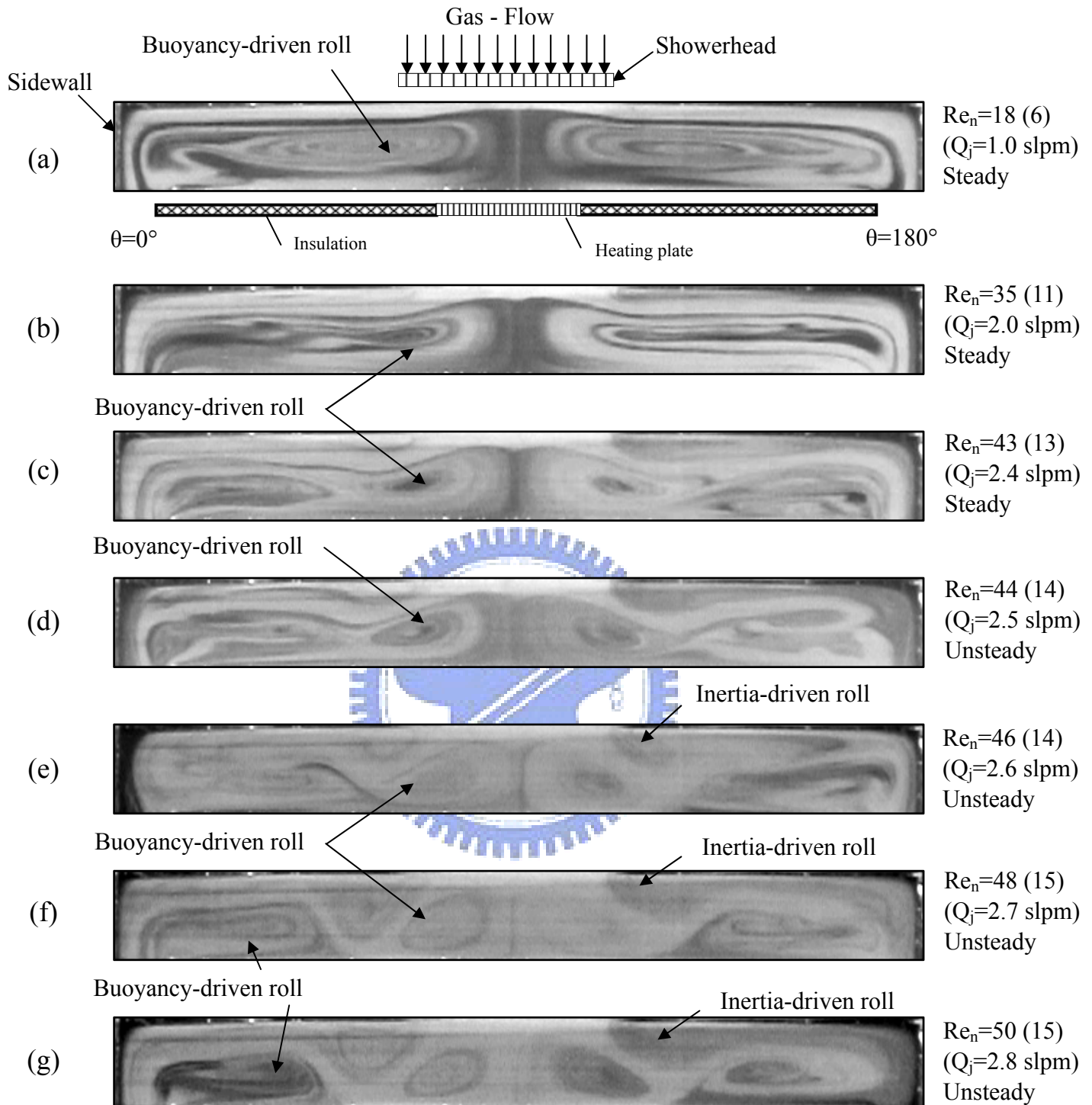
Fig. 4.20 Side view flow photos taken at the cross plane $\theta = 0°$ & $180°$ for various jet Reynolds numbers at Ra = 17,757 ($\Delta T = 7℃$) and H = 30.0 mm for Re_n = (a) 18, (b) 35, (c) 43, (d) 44, (e) 46, (f) 48, (g) 50, (h) 53, (i) 62, (j) 71, (k) 80 and (l) 89.

( ) : The number in the ( ) is the jet Reynolds number.

(h)   Inertia-driven roll Re_n=53 (17) (Q_j=3.0 slpm) Steady

Buoyancy-driven roll

(i)   Buoyancy-driven roll   Inertia-driven roll Re_n=62 (19) (Q_j=3.5 slpm) Steady

(j)   Inertia-driven roll Re_n=71 (22) (Q_j=4.0 slpm) Steady

Buoyancy-driven roll

(k)   Buoyancy-driven roll   Inertia-driven roll Re_n=80 (25) (Q_j=4.5 slpm) Steady

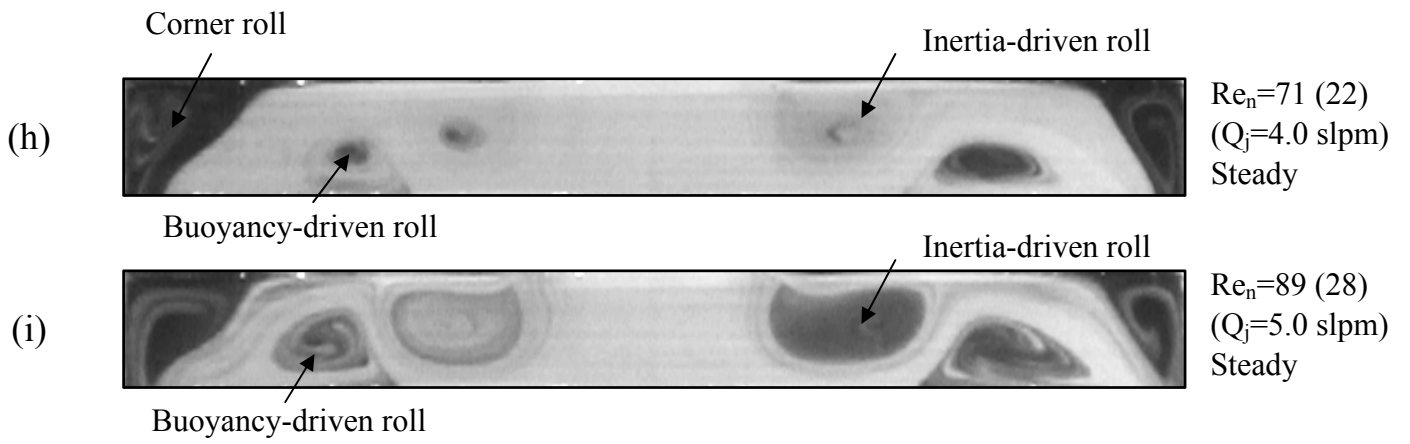(l)   Buoyancy-driven roll   Inertia-driven roll Re_n=89 (28) (Q_j=5.0 slpm) Steady
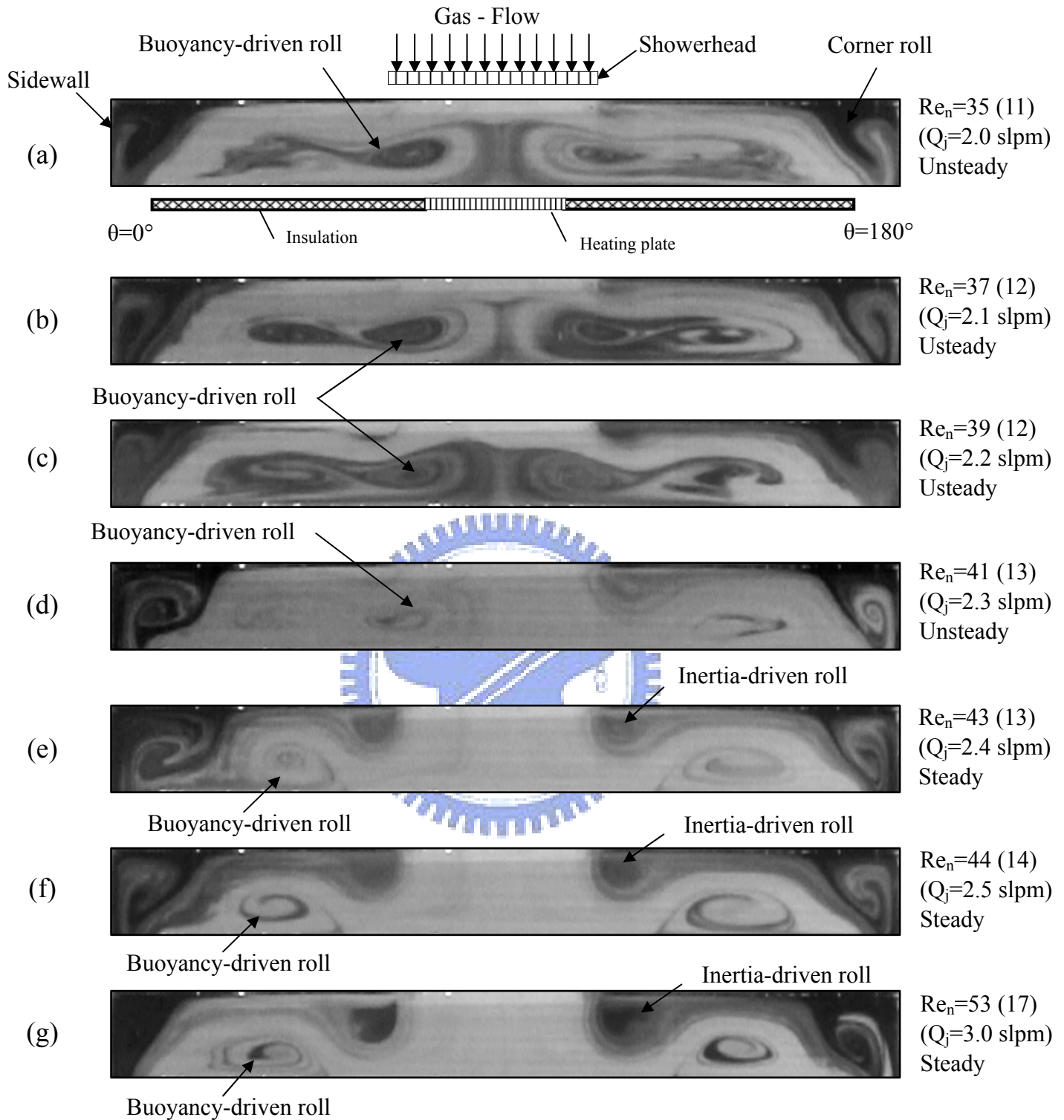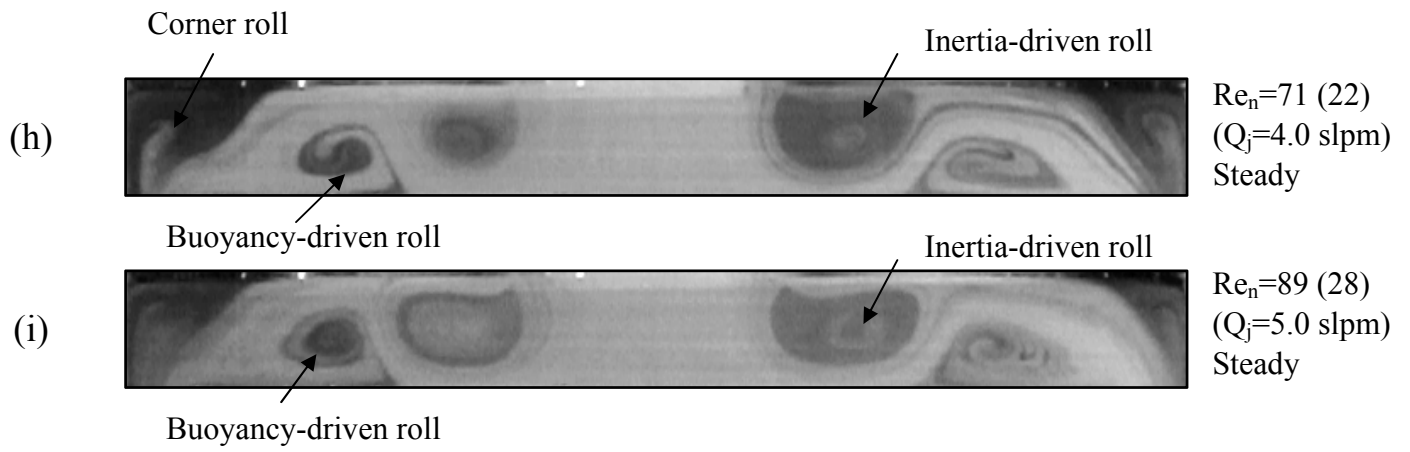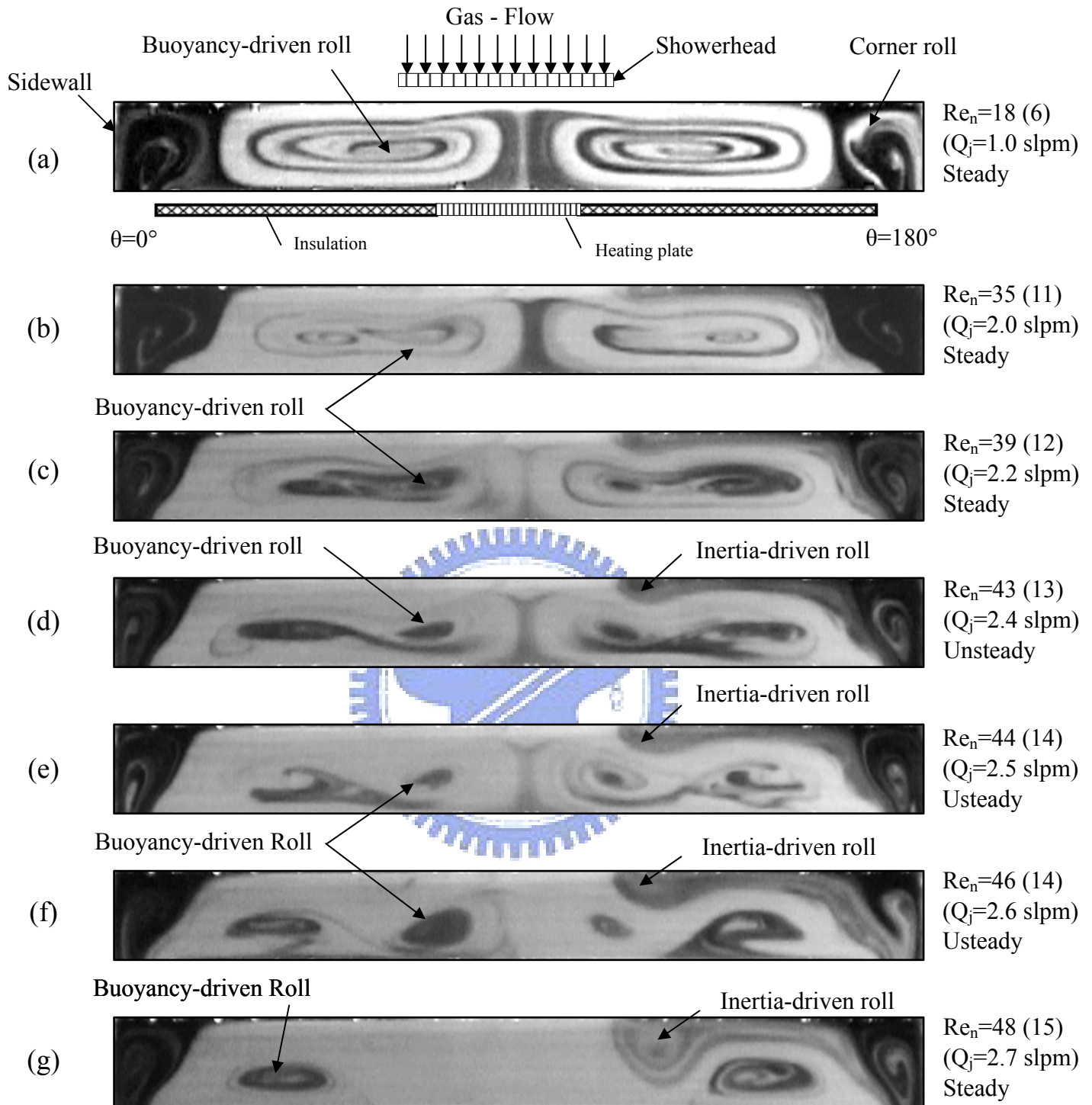
Fig. 4.20   Continued.

Fig. 4.21 Side view flow photos taken at the cross plane $\theta = 0°$ & $180°$ for various jet Reynolds numbers at Ra = 25,367 ($\Delta T = 10℃$) and H = 30.0 mm for Re_n = (a) 18, (b) 35, (c) 44, (d) 46, (e) 53, (f) 71, and (g) 89.

( ) : The number in the ( ) is the jet Reynolds number.

Fig. 4.22 Side view flow photos taken at the cross plane θ = 0° & 180° for various jet Reynolds numbers at Ra = 38051 (ΔT = 15℃) and H = 30.0 mm for Re_n = (a) 18, (b) 35, (c) 48, (d) 50, (e) 53, (f) 62, (g) 71, and (h) 89.

( ) : The number in the ( ) is the jet Reynolds number.

Buoyancy-driven roll   Inertia-driven roll

(h)   Re$_n$=89 (28)
                                                       (Q$_j$=5.0 slpm)
                                                       Steady
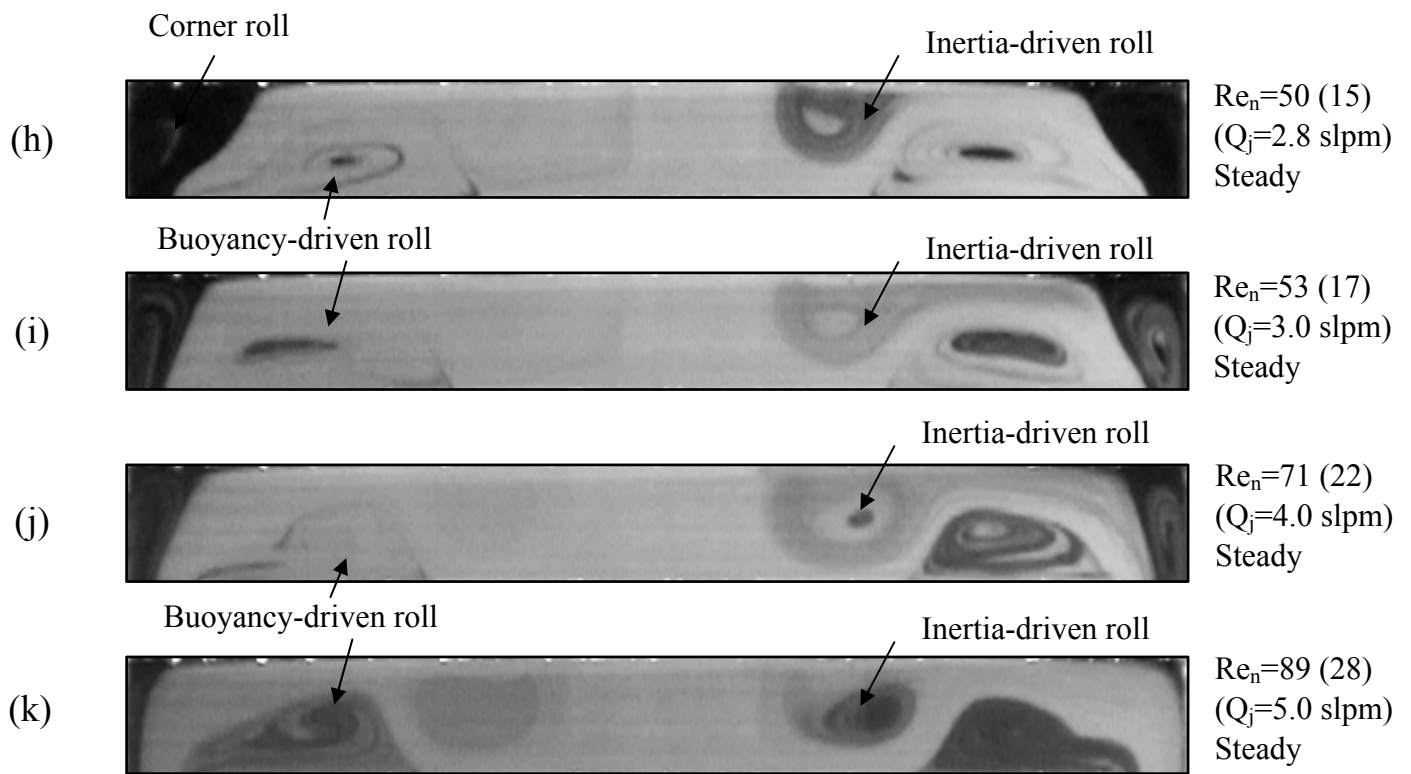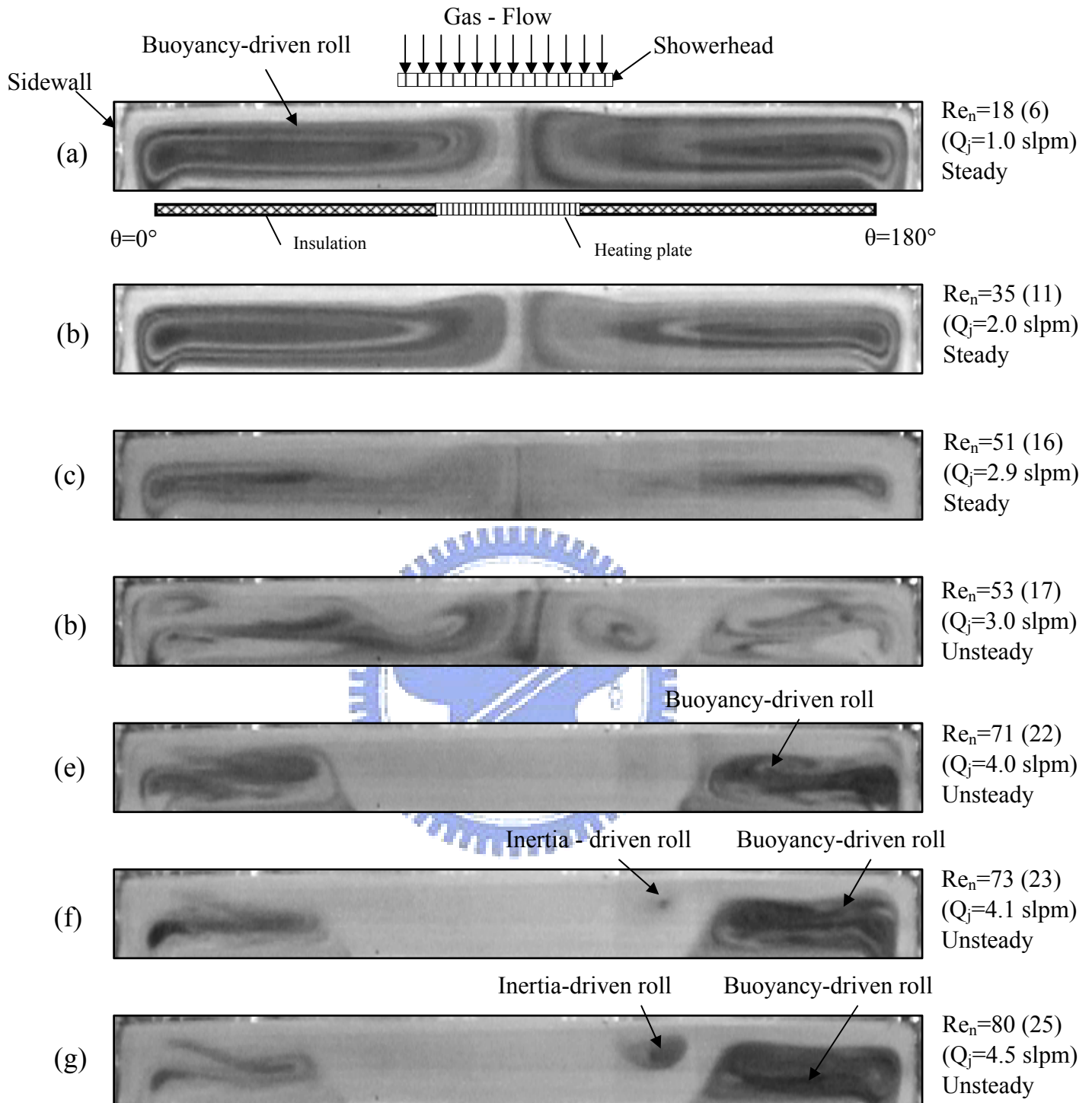
Fig. 4.22   Continued.

Fig. 4.23 Side view flow photos taken at the cross plane θ = 0° & 180° for various jet Reynolds numbers at Ra = 50,734 (ΔT = 20℃) and H = 30.0 mm for Re_n = (a) 18, (b) 35, (c) 51, (d) 53, (e) 71, (f) 73, (g) 80, and (h) 98.

( ) : The number in the ( ) is the jet Reynolds number.

Inertia-driven roll   Buoyancy-driven roll
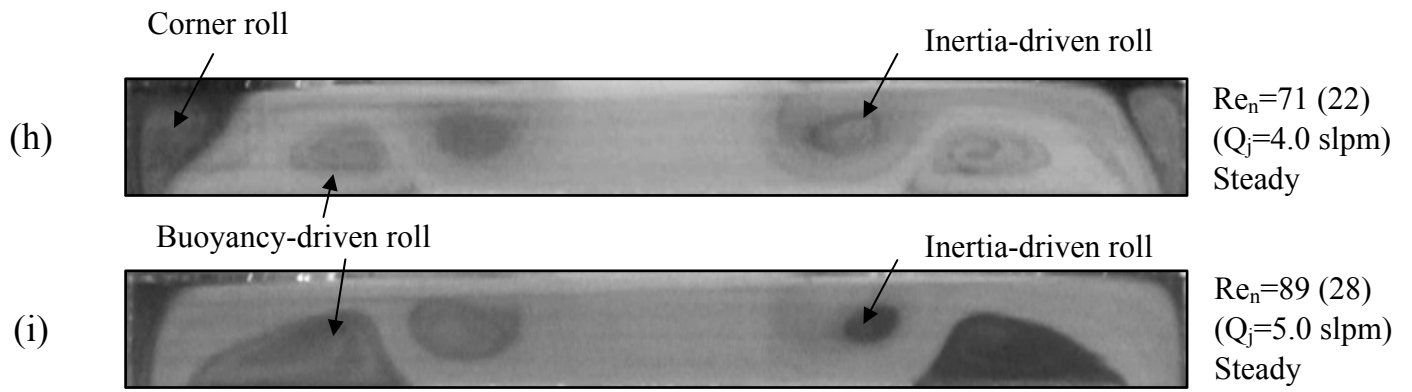
(h)

$Re_n = 98$ (28)
($Q_j = 5.5$ slpm)
Unsteady
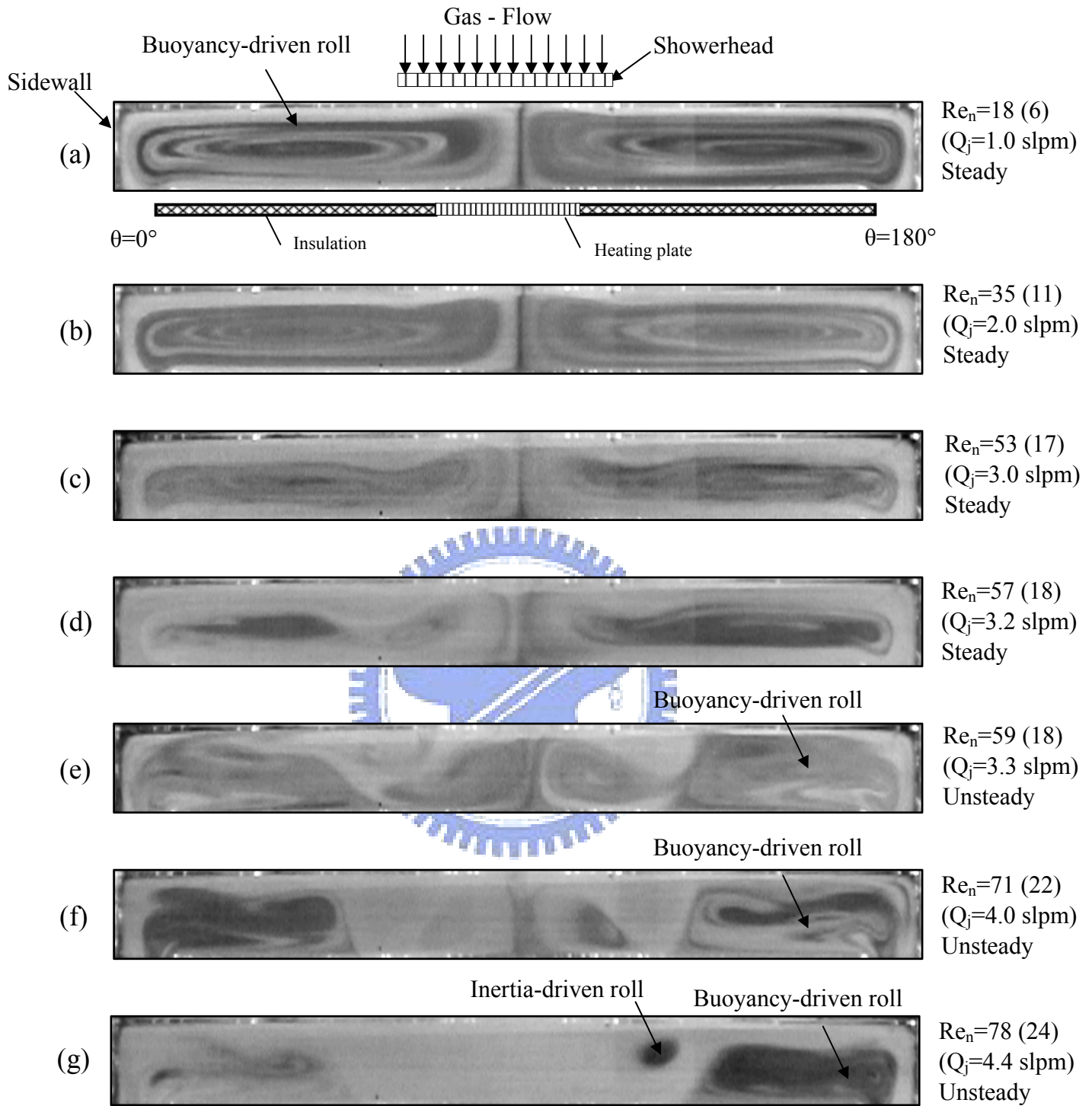
Fig. 4.23   Continued.

Fig. 4.24 Side view flow photos taken at the cross plane θ = 0° & 180° for various jet Reynolds numbers at Ra = 63,418 (ΔT = 25℃) and H = 30.0 mm for Re_n = (a) 18, (b) 35, (c) 53, (d) 57, (e) 59, (f) 71, (g) 78, and (h) 89.
( ) : The number in the ( ) is the jet Reynolds number.

Inertia-driven roll Buoyancy-driven roll
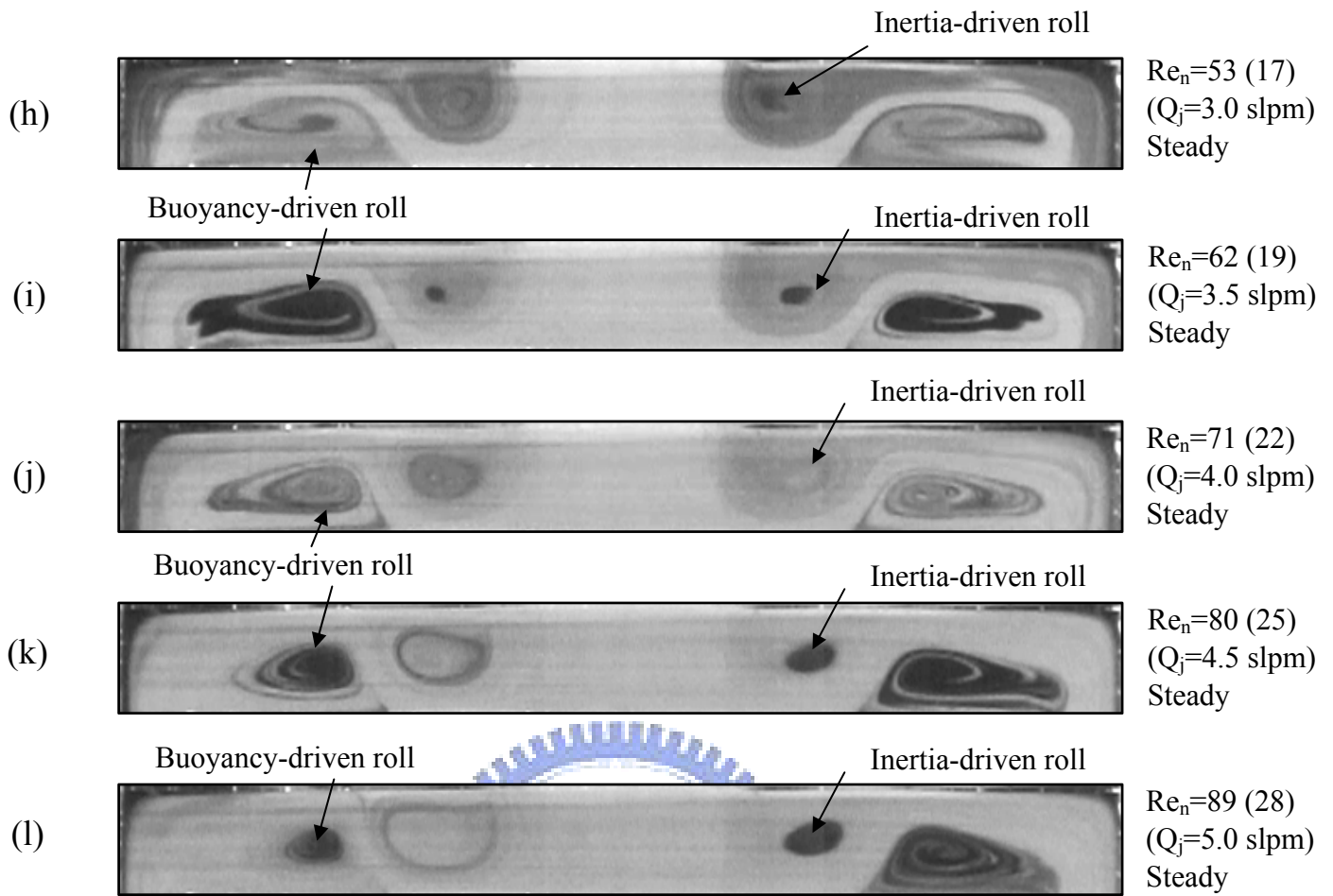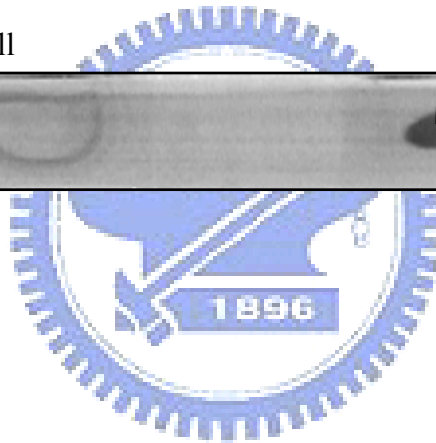
(h)

Re$_n$=89 (28)
(Q$_j$=5.0 slpm)
Unsteady

Fig. 4.24   Continued.

Fig. 4.25 Side view flow photos taken at the cross plane θ = 0° & 180° for various jet Reynolds numbers at Ra = 6,013 (ΔT = 1℃) and H = 40.0 mm for Re_n = (a) 18, (b) 30, (c) 35, (d) 39, (e) 41, (f) 44, (g) 46, (h) 50, (i) 53, (j) 74 and (k) 89.

( ) : The number in the ( ) is the jet Reynolds number.

(g) Corner roll   Inertia-driven roll
Re_n=46 (14)
(Q_j=2.6 slpm)
Steady
Buoyancy-driven roll

(h) Inertia-driven roll
Buoyancy-driven roll
Re_n=50 (15)
(Q_j=2.8 slpm)
Steady

(i) Inertia-driven roll
Buoyancy-driven roll
Re_n=53 (17)
(Q_j=3.0 slpm)
Steady

(j) Inertia-driven roll
Buoyancy-driven roll
Re_n=71 (22)
(Q_j=4.0 slpm)
Steady

(k) Inertia-driven roll
Buoyancy-driven roll
Re_n=89 (28)
(Q_j=5.0 slpm)
Steady
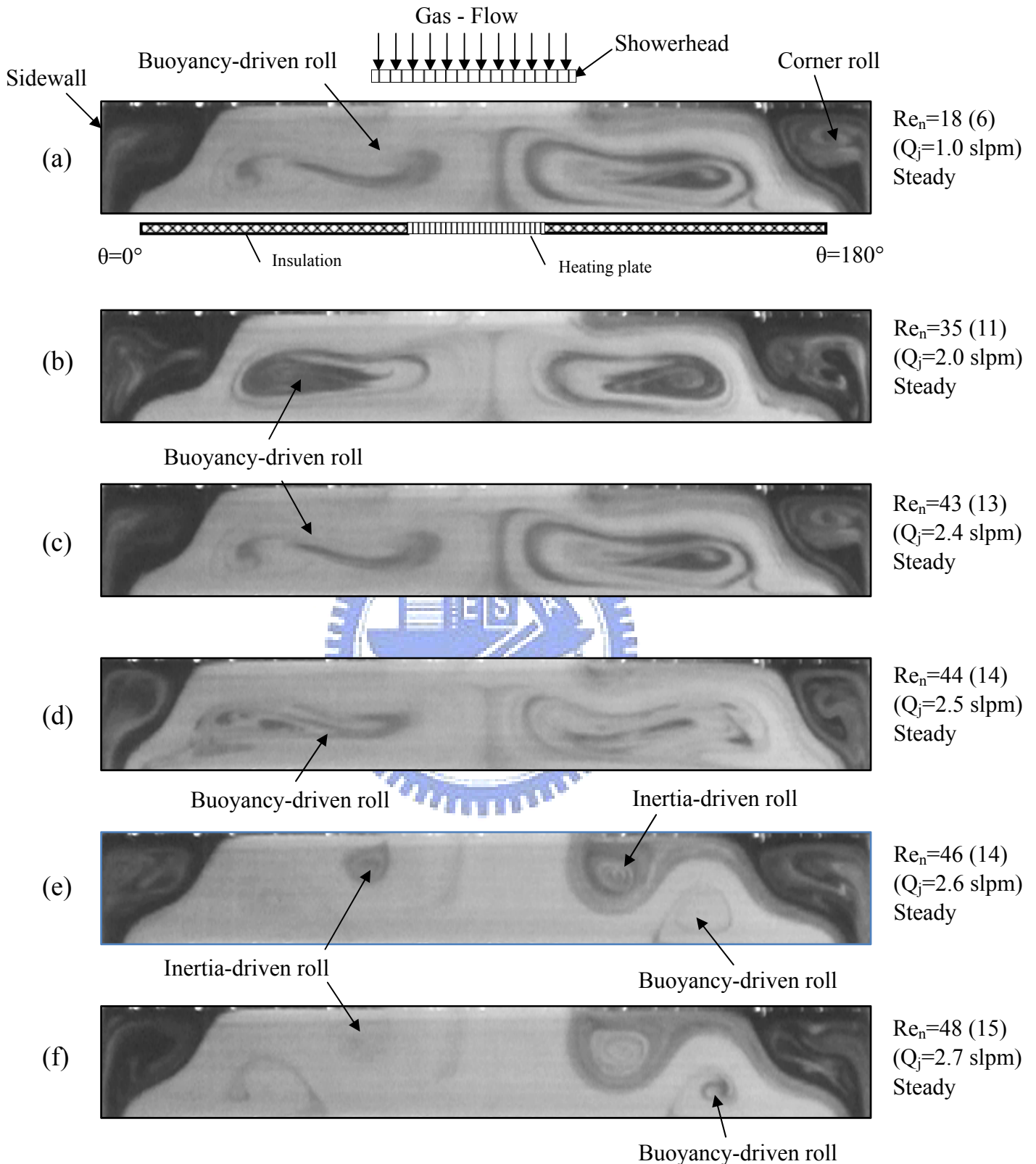
Fig. 4.25   Continued.
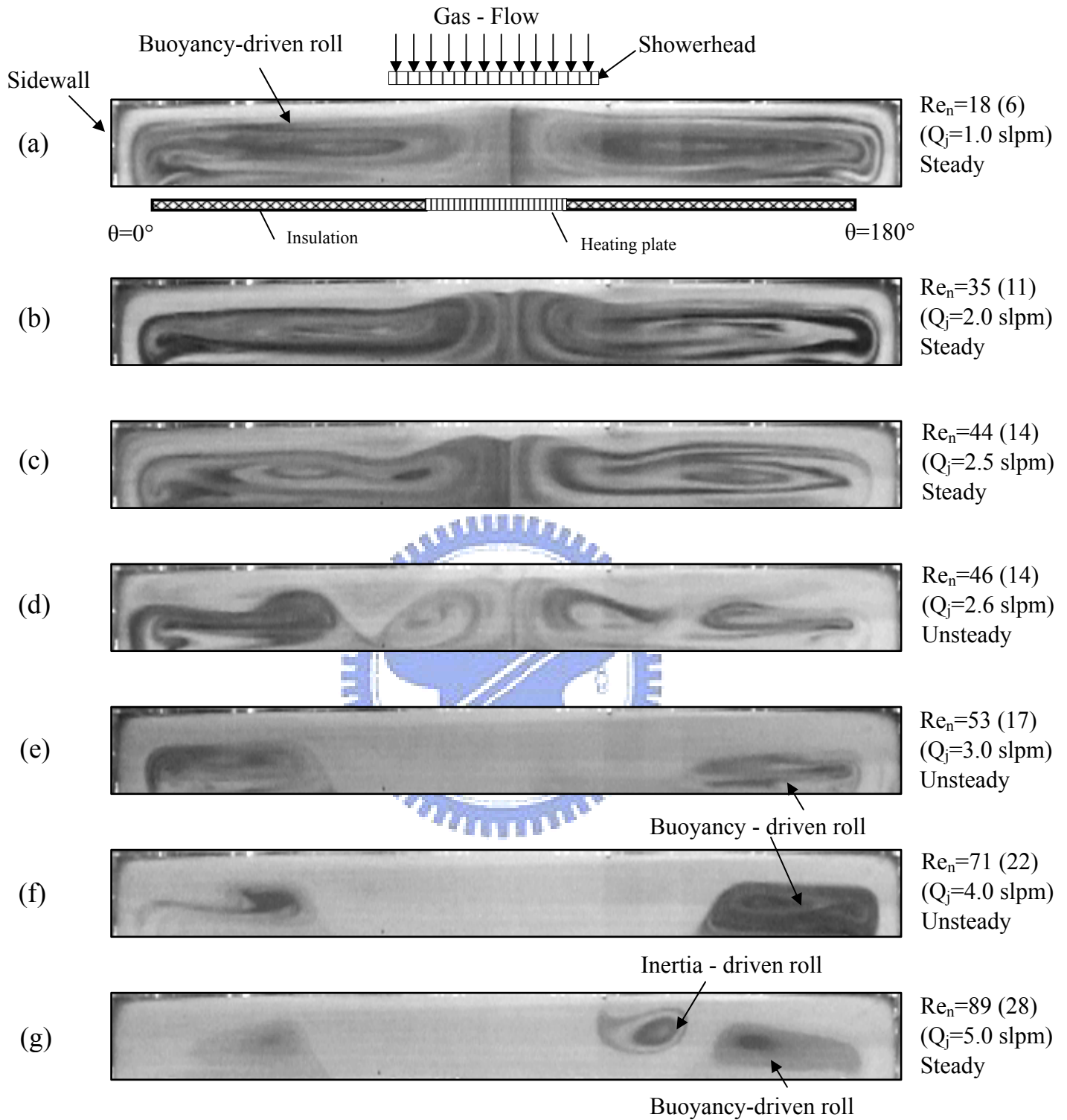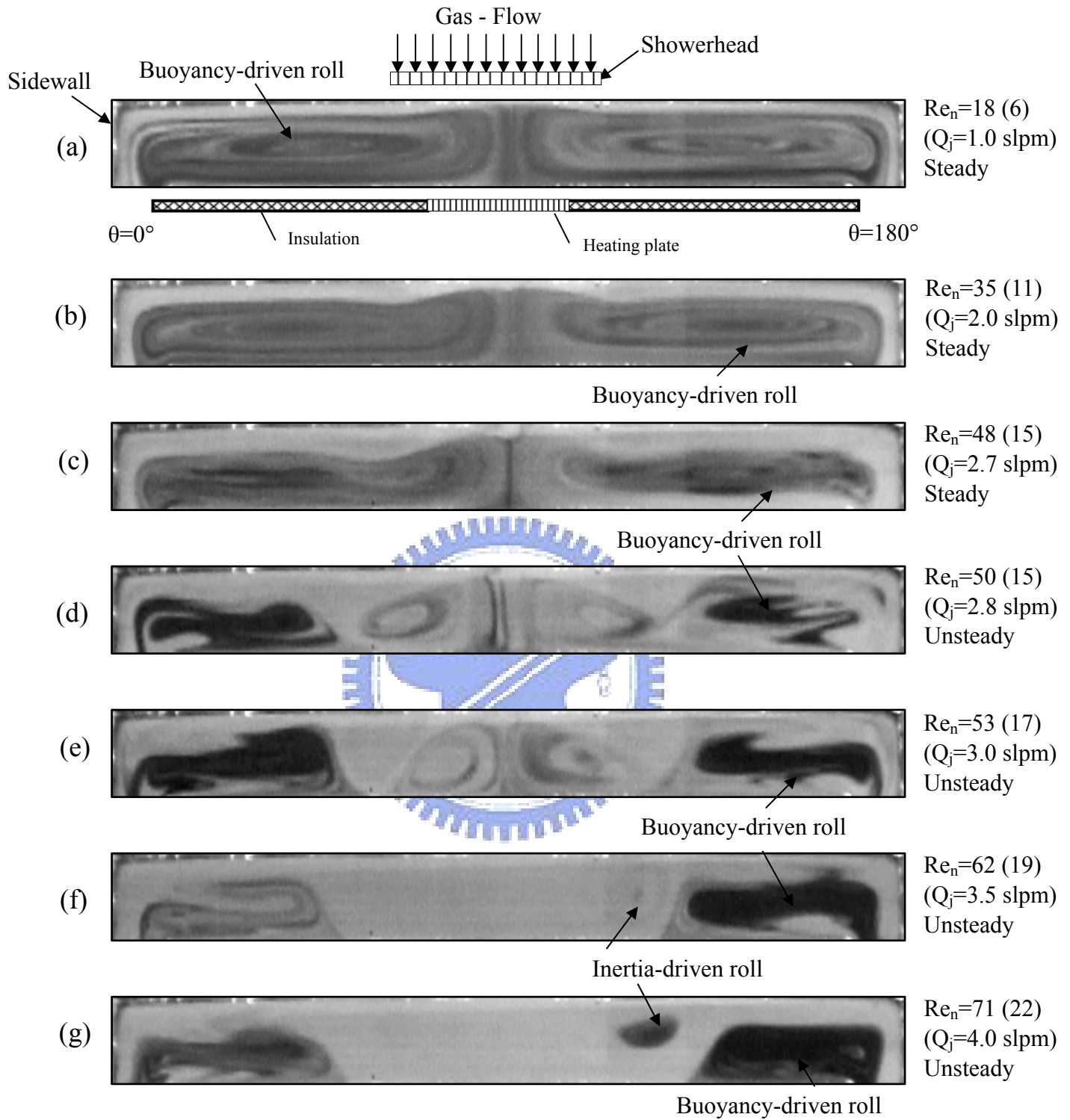
Fig. 4.26 Side view flow photos taken at the cross plane $\theta = 0°$ & $180°$ for various jet Reynolds numbers at Ra = 12,026 ($\Delta T = 2°C$) and H = 40.0 mm for Re_n = (a) 18, (b) 35, (c) 43, (d) 44, (e) 46, (f) 48, (g) 53, (h) 71 and (i) 89.

( ) : The number in the ( ) is the jet Reynolds number.

(g) — Corner roll / Inertia-driven roll — $Re_n=53$ (17) ($Q_j=3.0$ slpm) Steady

(h) — Inertia-driven roll / Buoyancy-driven roll — $Re_n=71$ (22) ($Q_j=4.0$ slpm) Steady

(i) — Inertia-driven roll / Buoyancy-driven roll — $Re_n=89$ (28_ ($Q_j=5.0$ slpm) Steady
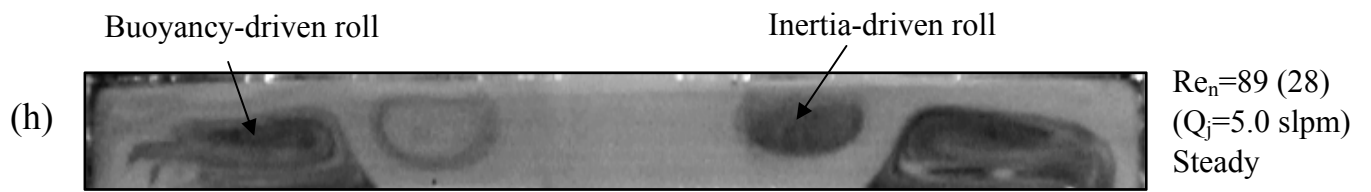
Fig. 4.26   Continued.

Fig. 4.27 Side view flow photos taken at the cross plane θ = 0° & 180° for various jet Reynolds numbers at Ra = 18,039 (ΔT = 3℃) and H = 40.0 mm for Re_n = (a) 18, (b) 35, (c) 43, (d) 44, (e) 46, (f) 48, (g) 50, (h) 53, (i) 71 and (j) 89.

( ) : The number in the ( ) is the jet Reynolds number.

(g) Inertia-driven roll ... Buoyancy-driven roll — $Re_n=50$ (15) ($Q_j=2.8$ slpm) Steady

(h) Inertia-driven roll ... Buoyancy-driven roll — $Re_n=53$ (17) ($Q_j=3.0$ slpm) Steady

(i) Inertia-driven roll ... Buoyancy-driven roll — $Re_n=71$ (22) ($Q_j=4.0$ slpm) Steady

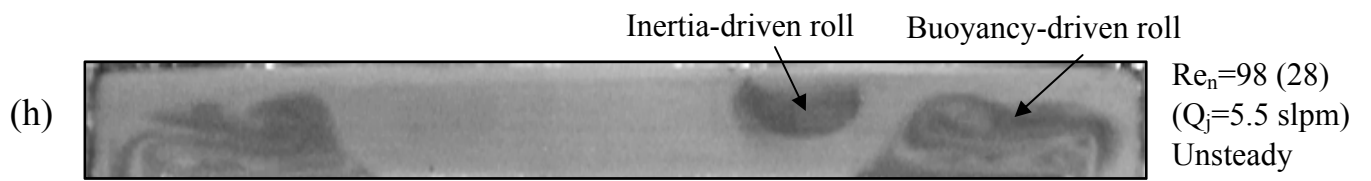(j) Inertia-driven roll ... Buoyancy-driven roll — $Re_n=89$ (28) ($Q_j=5.0$ slpm) Steady

Fig. 4.27   Continued.

Fig. 4.28 Side view flow photos taken at the cross plane θ = 0° & 180° for various jet Reynolds numbers at Ra = 24,052 (ΔT = 4℃) and H = 40.0 mm for Re_n = (a) 18, (b) 35, (c) 43, (d) 44, (e) 46, (f) 48, (g) 51, (h) 53, (i) 71 and (j) 89.
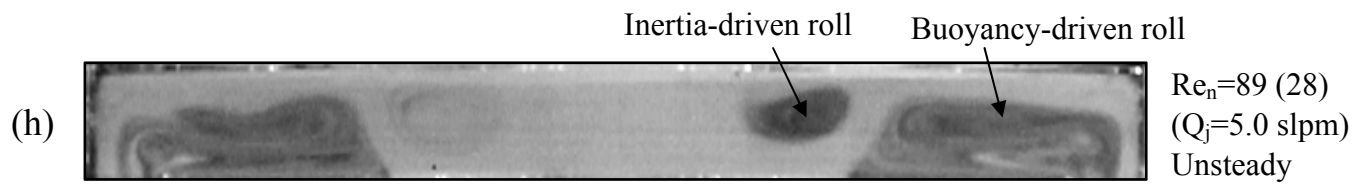
( ) : The number in the ( ) is the jet Reynolds number.

Fig. 4.28   Continued.
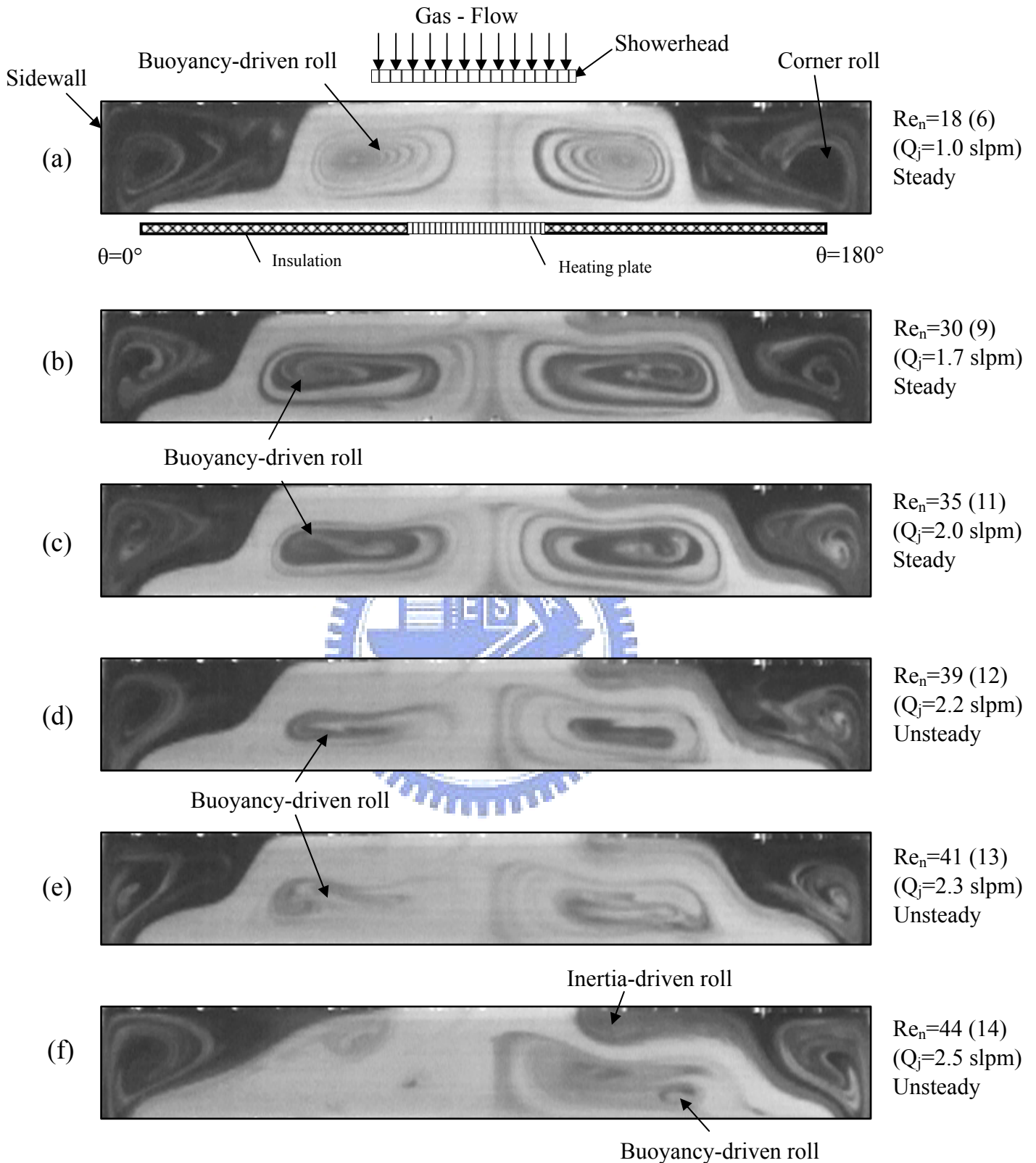
Fig. 4.29 Side view flow photos taken at the cross plane θ = 0° & 180° for various jet Reynolds numbers at Ra = 30,065 (ΔT = 5℃) and H = 40.0 mm for Re_n = (a) 18, (b) 35, (c) 50, (d)51, (e) 53, (f) 55, (g) 57, (h) 59, (i) 71 and (j) 89.

( ) : The number in the ( ) is the jet Reynolds number.

(g) Inertia-driven roll   Buoyancy-driven roll $Re_n=57$ (18) ($Q_j=3.2$ slpm) Steady

(h) Inertia-driven roll   Buoyancy-driven roll $Re_n=59$ (18) ($Q_j=3.3$ slpm) Steady

(i) Inertia-driven roll   Buoyancy-driven roll $Re_n=71$ (22) ($Q_j=4.0$ slpm) Steady

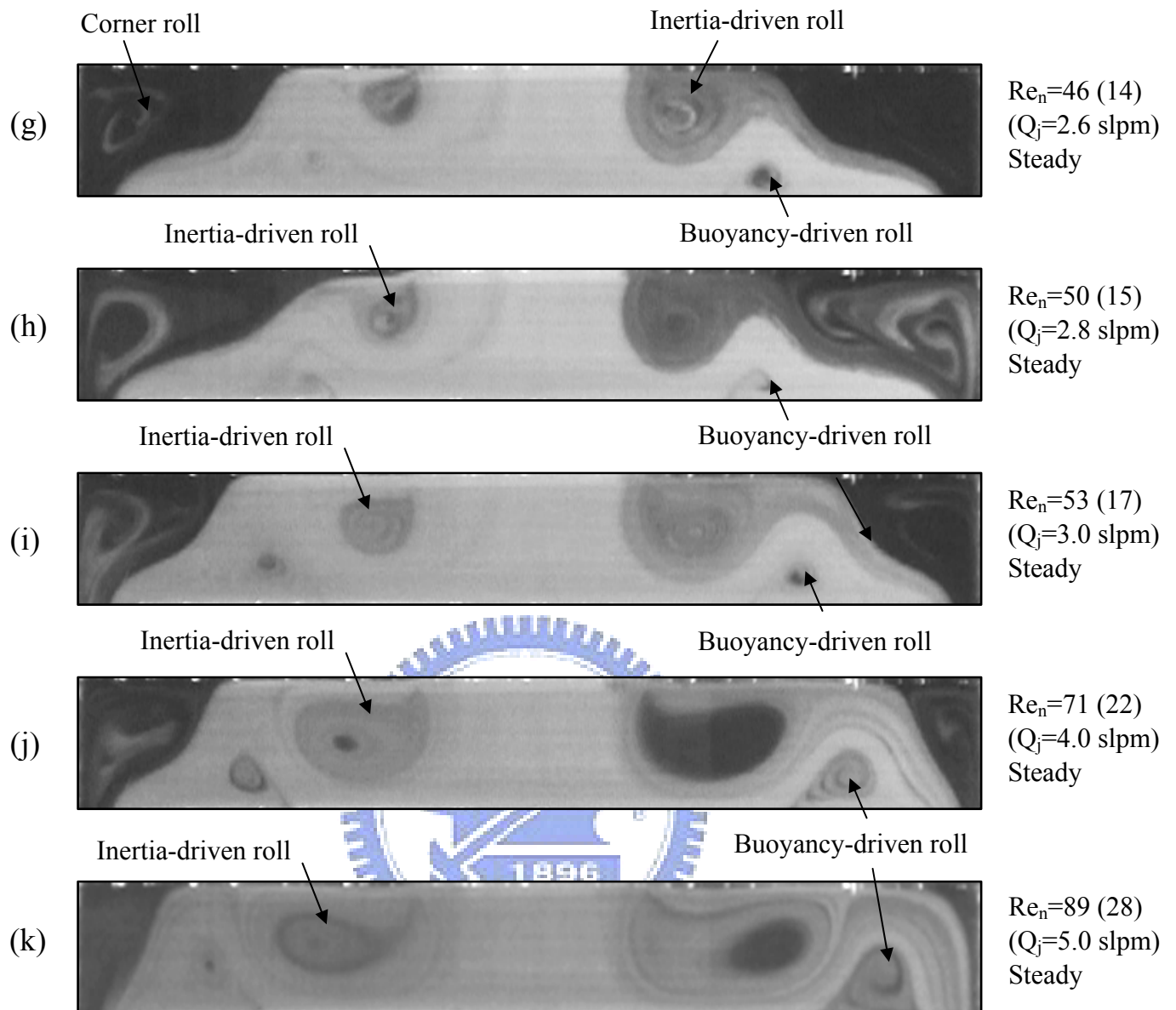(j) Inertia-driven roll   Buoyancy-driven roll $Re_n=89$ (28) ($Q_j=5.0$ slpm) Steady

Fig. 4.29   Continued.

Fig. 4.30 Side view flow photos taken at the cross plane θ = 0° & 180° for various jet
Reynolds numbers at Ra = 60,130 (ΔT = 10℃) and H = 40.0 mm for Re_j = (a) 18, (b)
27, (c) 35, (d)44, (e) 53, (f) 55, (g) 57, (h) 62, (i) 64, (j) 71, (k) 80, and (l) 89.
( ) : The number in the ( ) is the jet Reynolds number.

(g) $Re_n=57$ (18) ($Q_j=3.2$ slpm) Unsteady

(h) $Re_n=62$ (19) ($Q_j=3.5$ slpm) Unsteady

Inertia-driven roll   Buoyancy-driven roll

(i) $Re_n=64$ (20) ($Q_j=3.6$ slpm) Steady

Inertia-driven roll   Buoyancy-driven roll

(j) $Re_n=71$ (22) ($Q_j=4.0$ slpm) Steady

Inertia-driven roll   Buoyancy-driven roll

(k) $Re_n=80$ (25) ($Q_j=4.5$ slpm) Steady

Inertia-driven roll   Buoyancy-driven roll
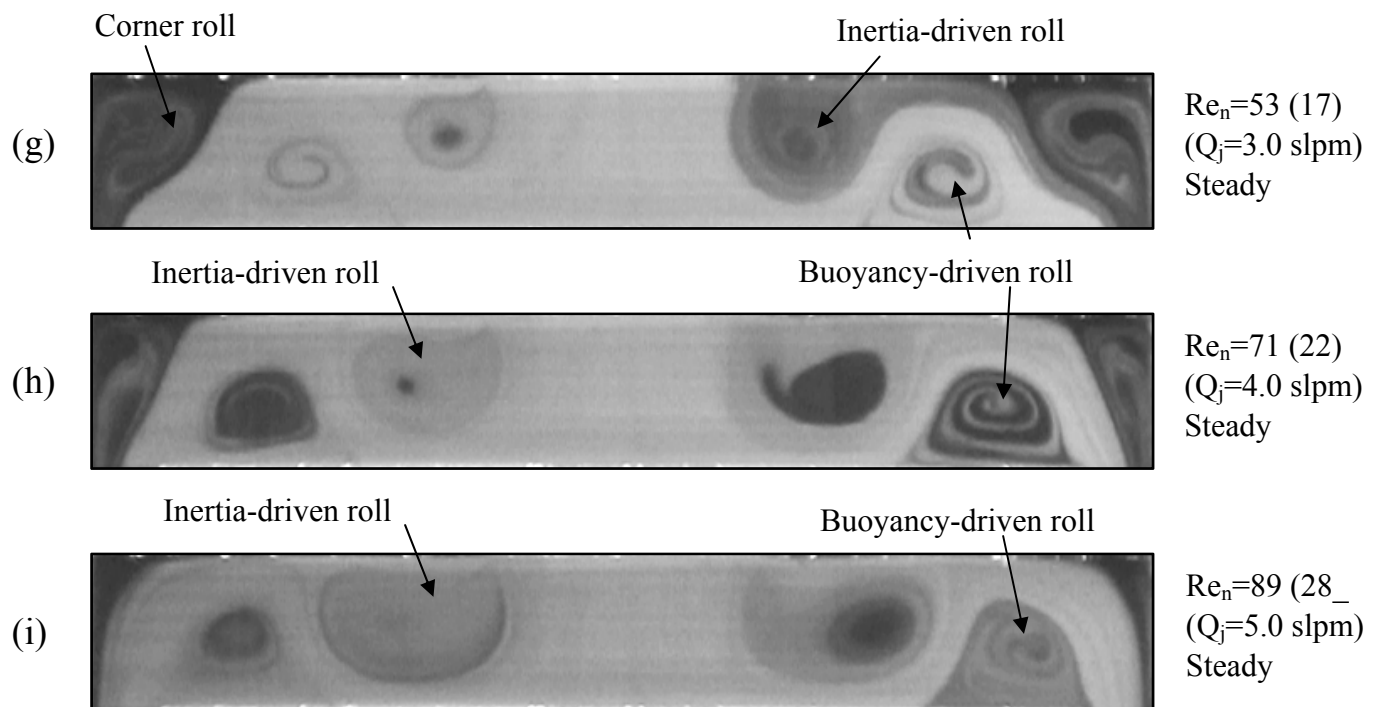
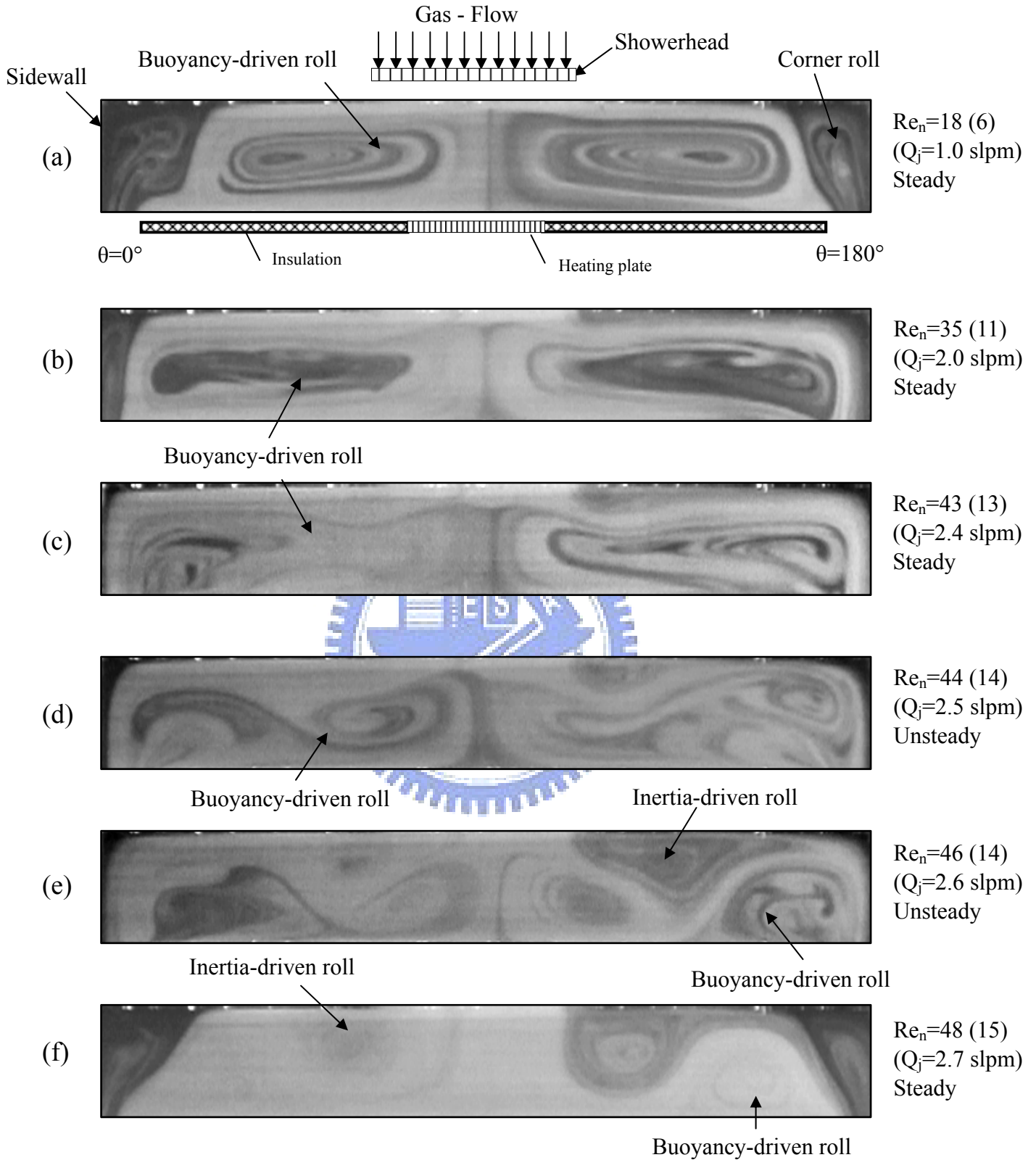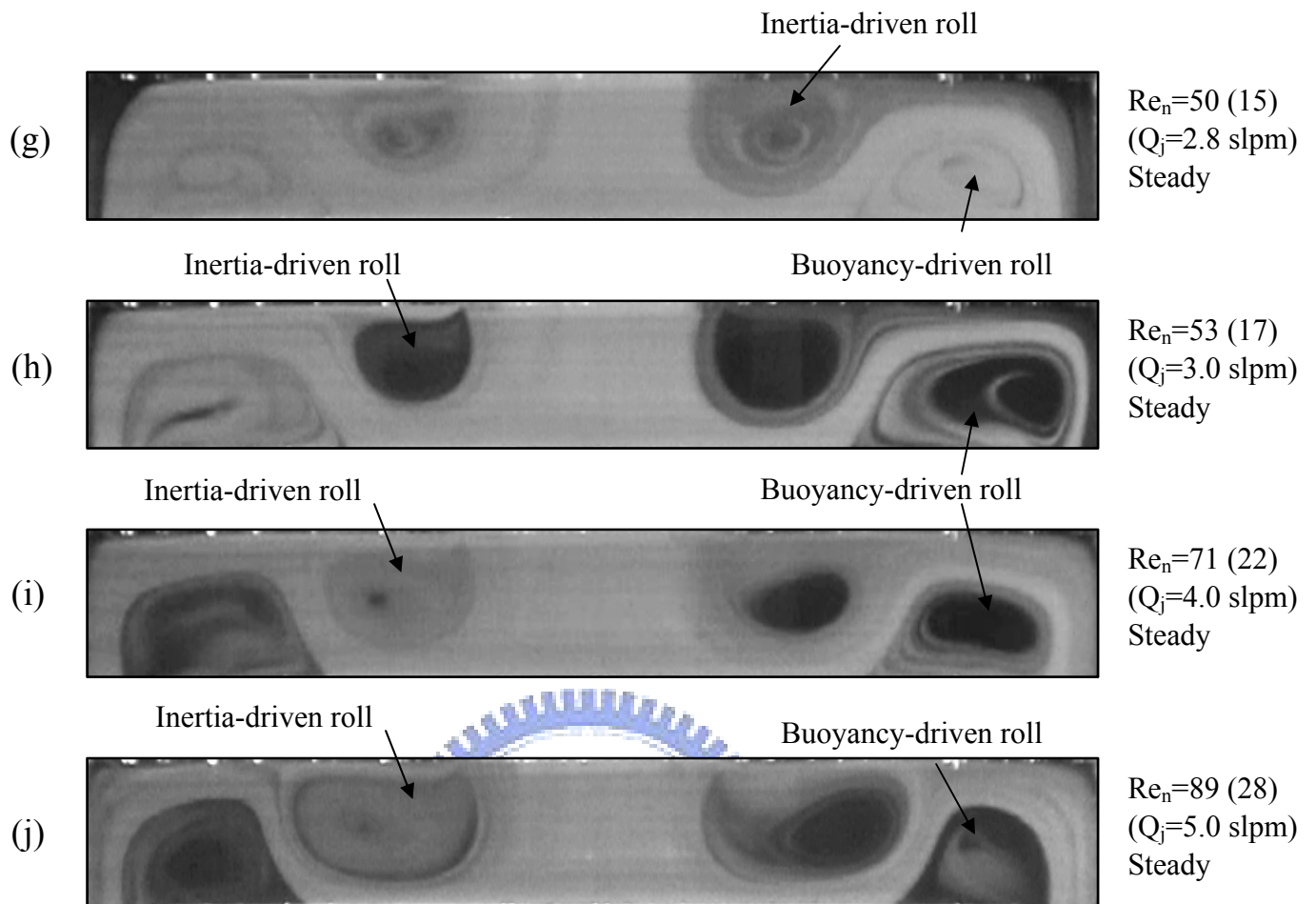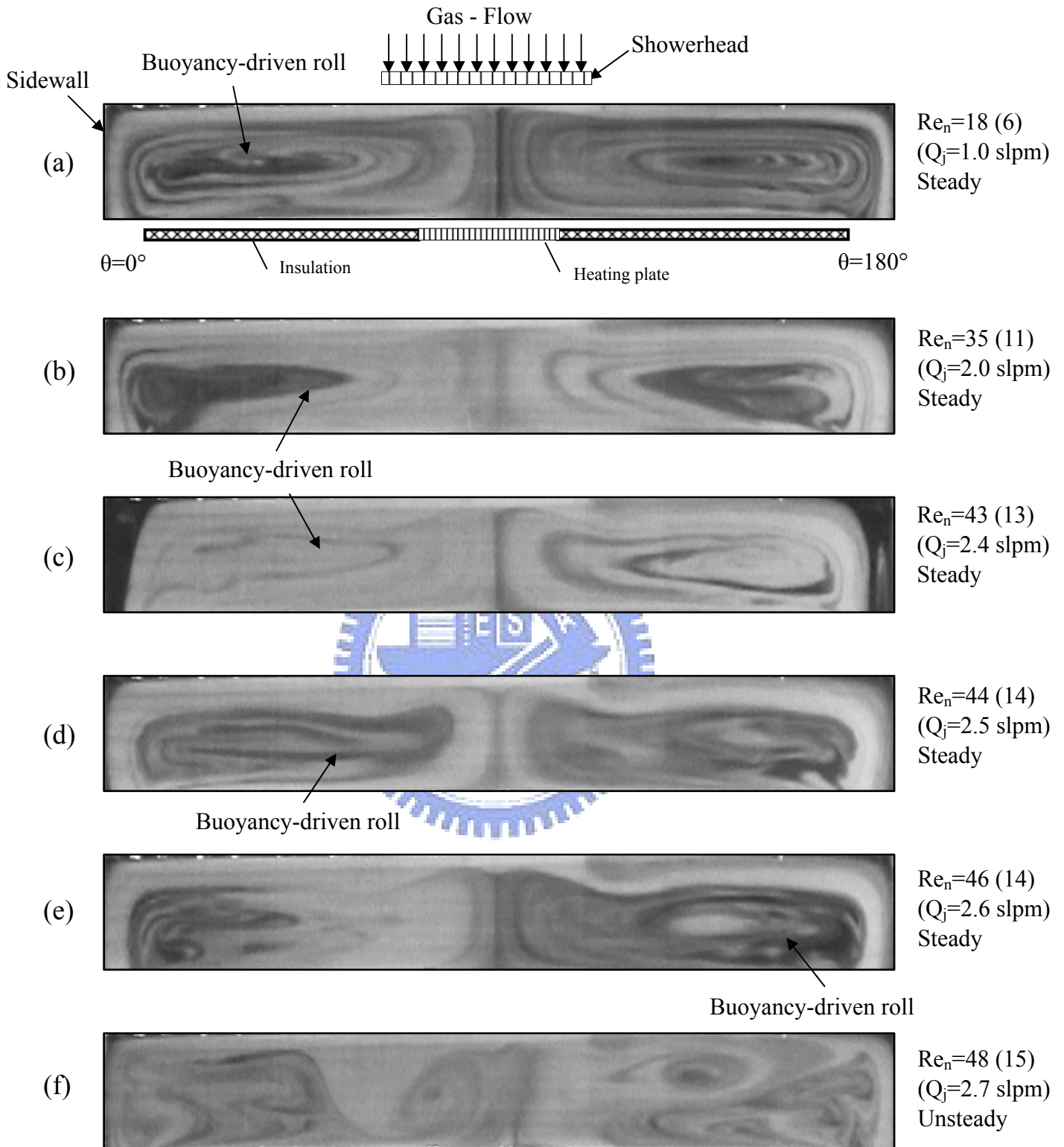(l) $Re_n=89$ (28) ($Q_j=5.0$ slpm) Steady
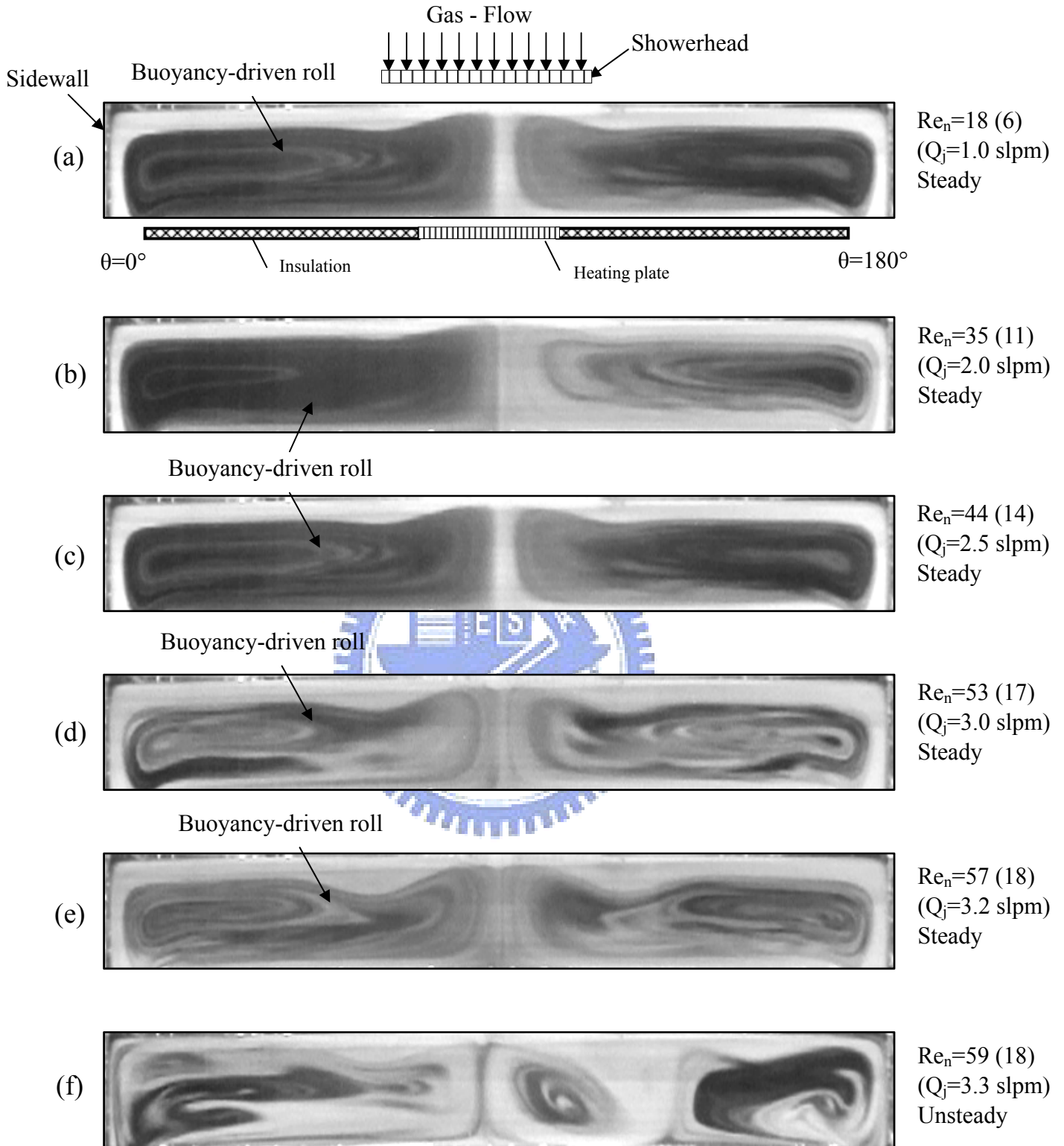
Fig. 4.30   Continued.

Fig. 4.31   Side view flow photos taken at the cross plane $\theta = 0°$ & $180°$ for various jet Reynolds numbers at Ra = 90,195 ($\Delta T = 15°C$) and H = 40.0 mm for $Re_n =$ (a) 18, (b) 35, (c) 44, (d)53, (e) 57, (f) 59, (g) 62, (h) 71, (i) 80, and (j) 89.

( ) : The number in the ( ) is the jet Reynolds number.

(g) Re_n=62 (19) (Q_j=3.5 slpm) Unsteady

Inertia-driven roll   Buoyancy-driven roll

(h) Re_n=71 (22) (Q_j=4.0 slpm) Steady

Inertia-driven roll   Buoyancy-driven roll

(i) Re_n=80 (25) (Q_j=4.5 slpm) Steady

Inertia-driven roll   Buoyancy-driven roll

(j) Re_n=89 (28) (Q_j=5.0 slpm) Steady
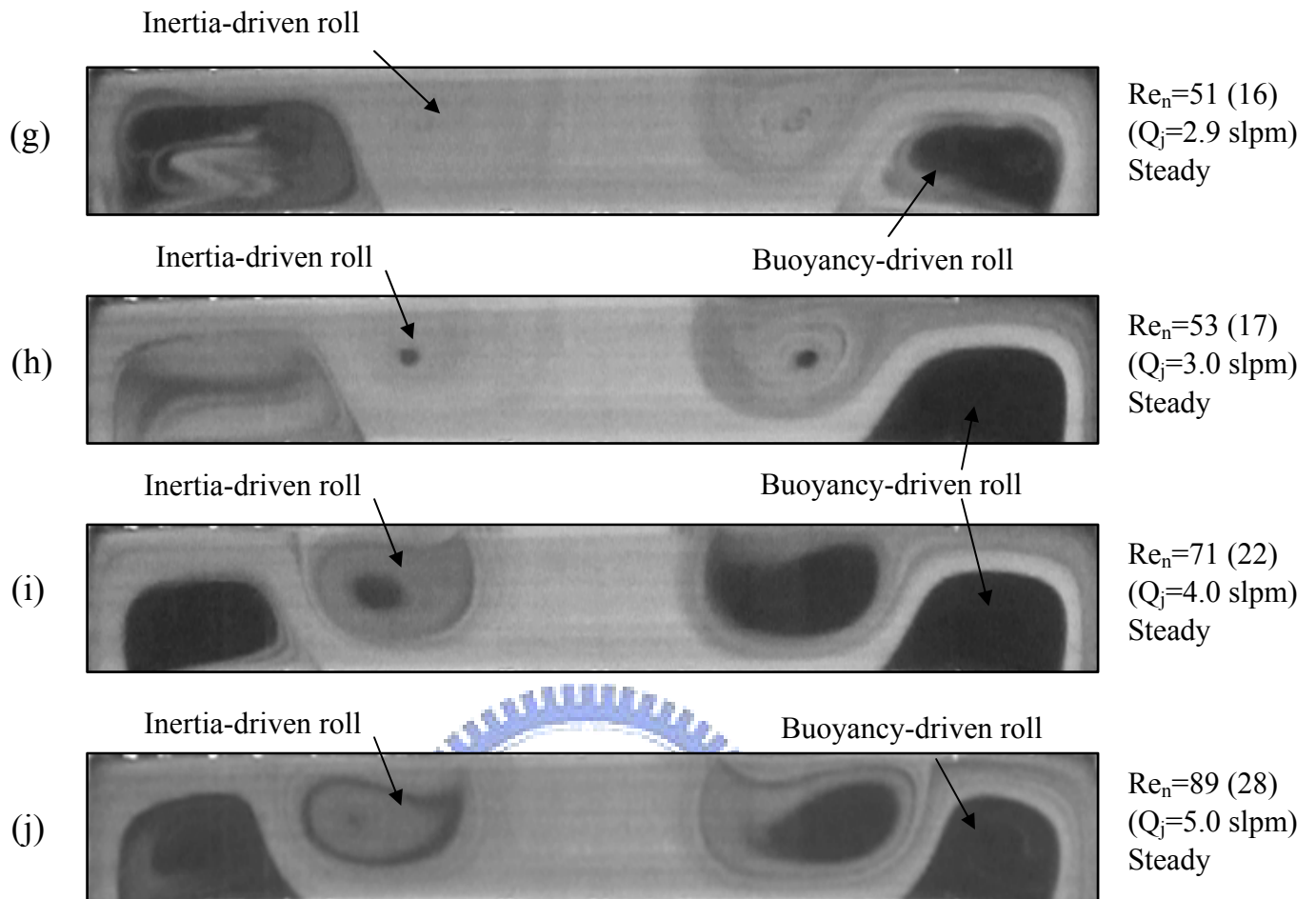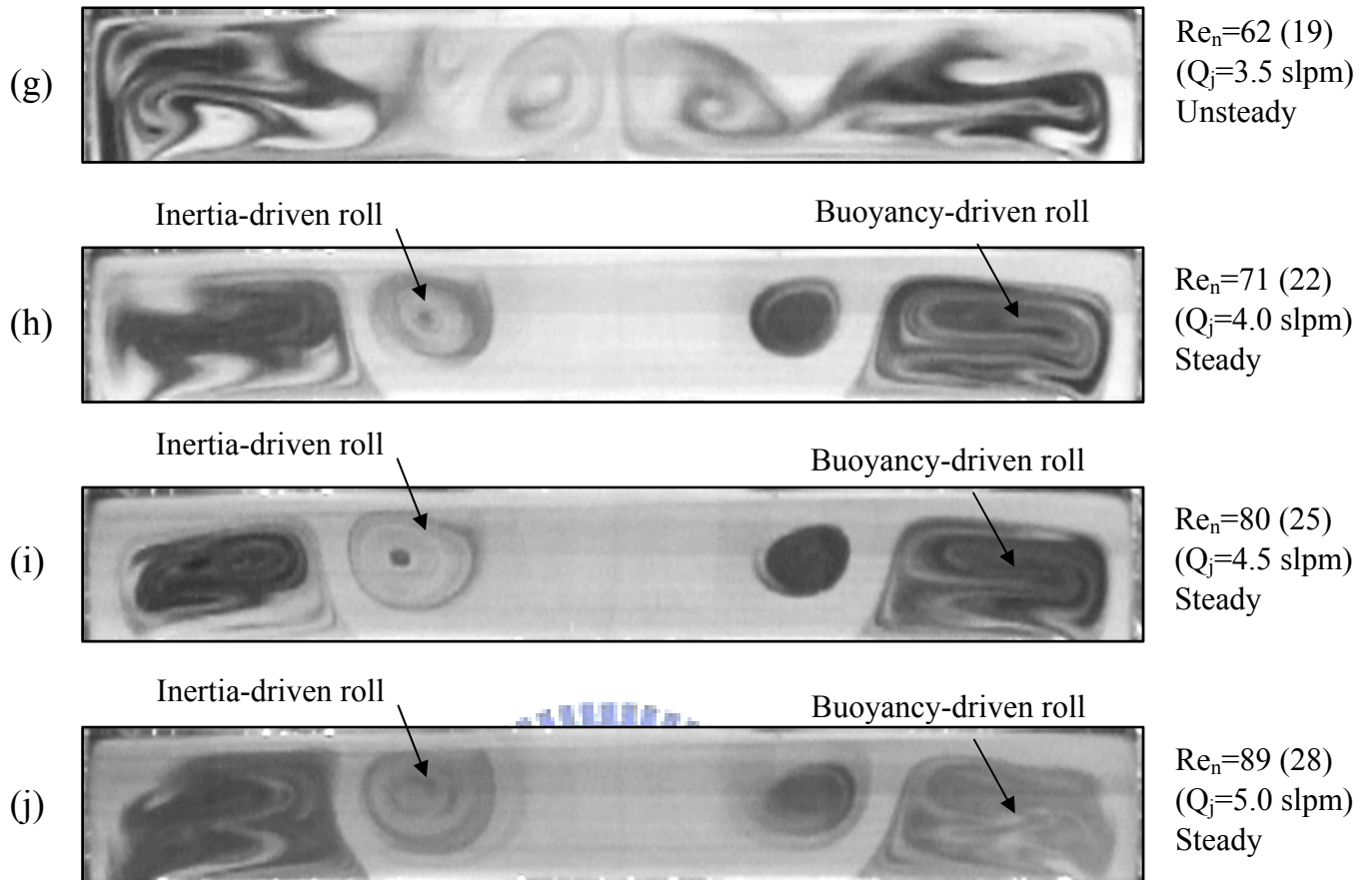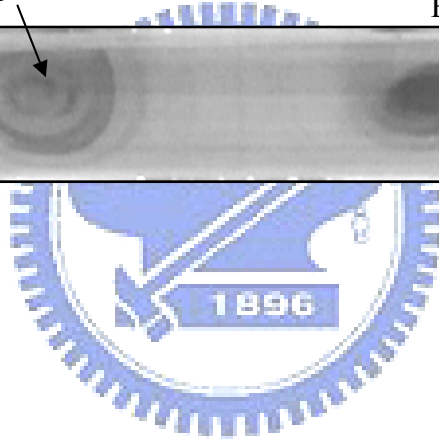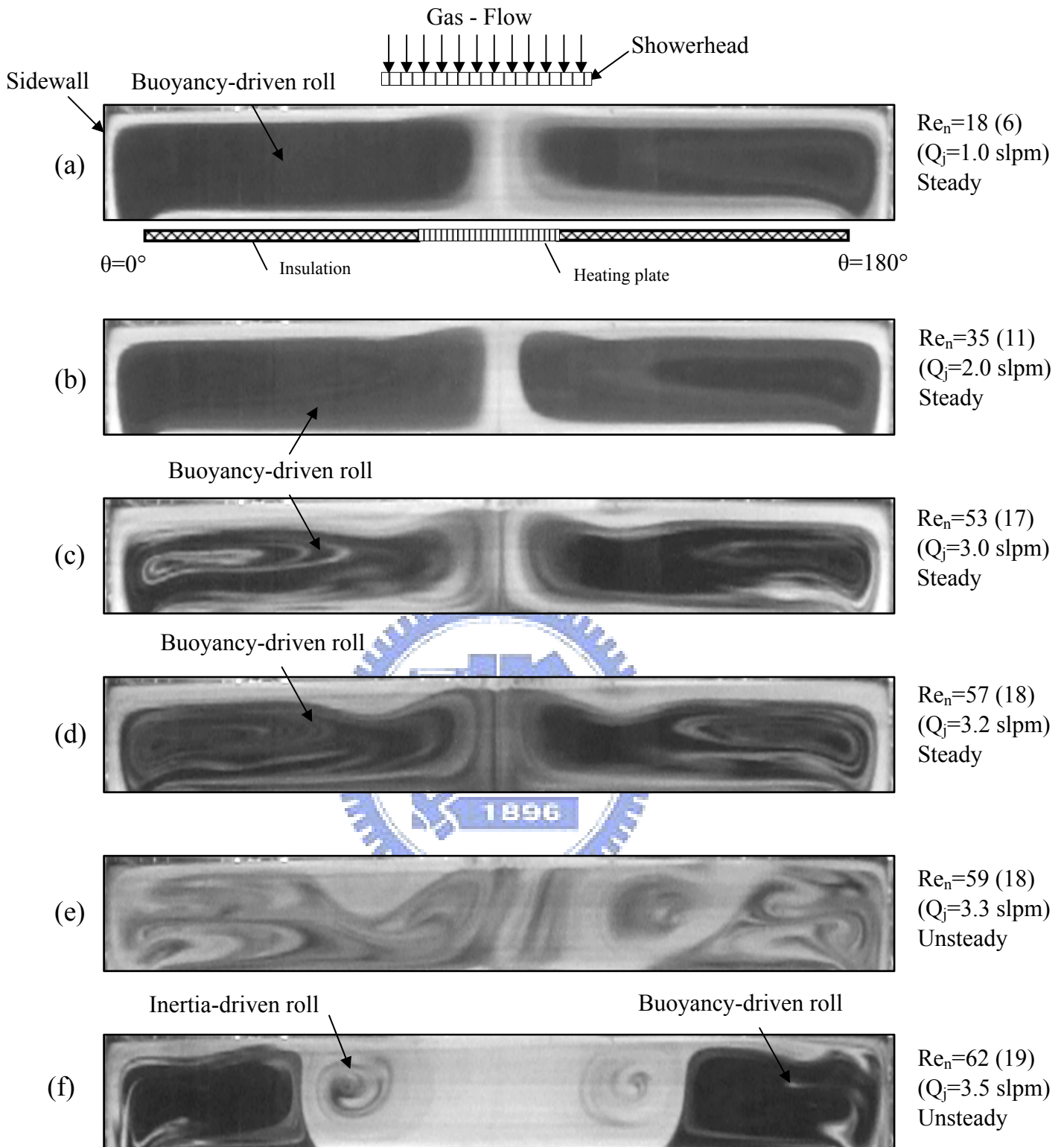
Fig. 4.31   Continued.

Fig. 4.32 Side view flow photos taken at the cross plane θ = 0° & 180° for various jet Reynolds numbers at Ra = 120,260 (ΔT = 20℃) and H = 40.0 mm for Re_n = (a) 18, (b) 35, (c) 53, (d)57, (e) 59, (f) 62, (g) 71, (h) 80, (i) 87, and (j) 89.
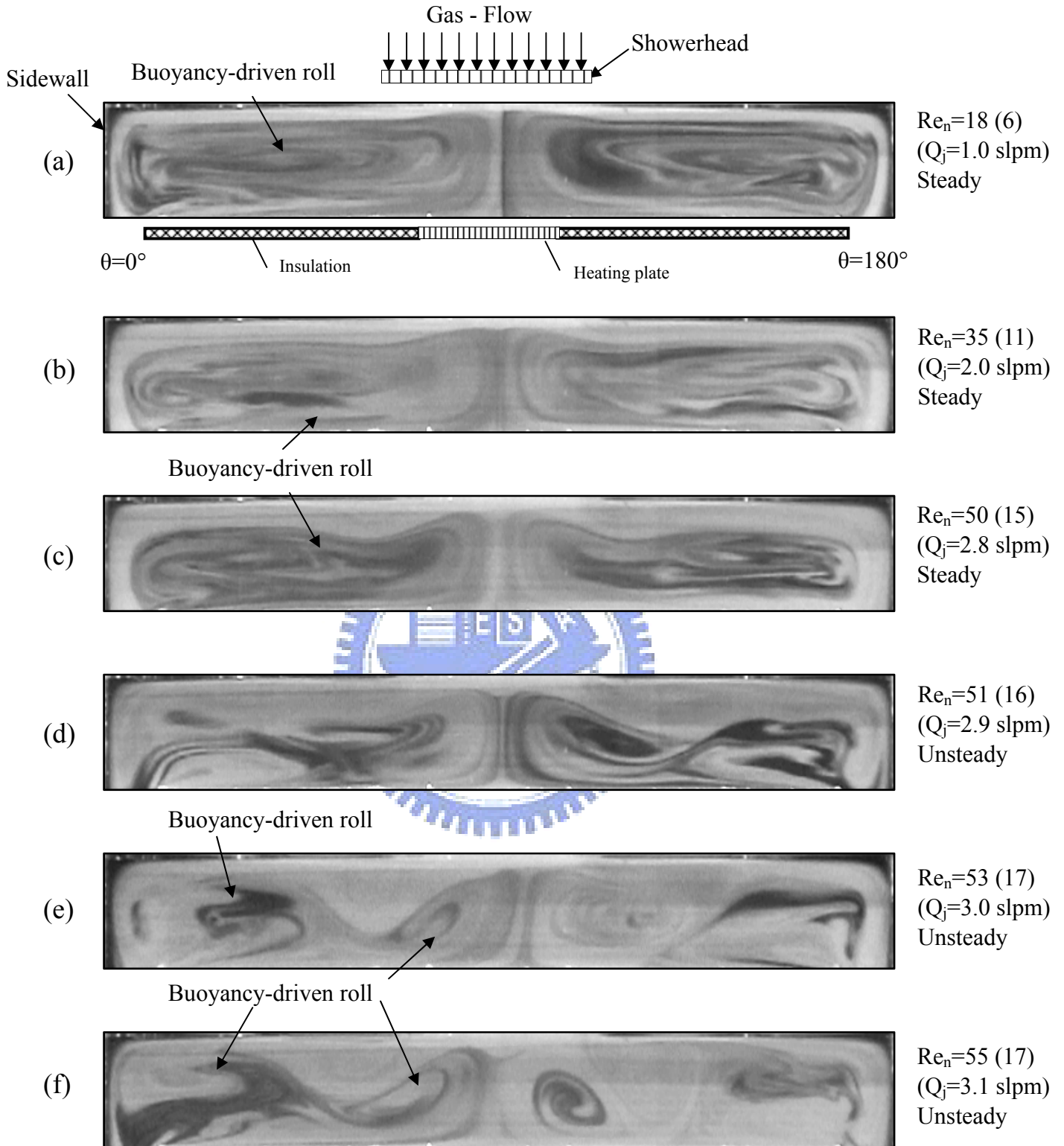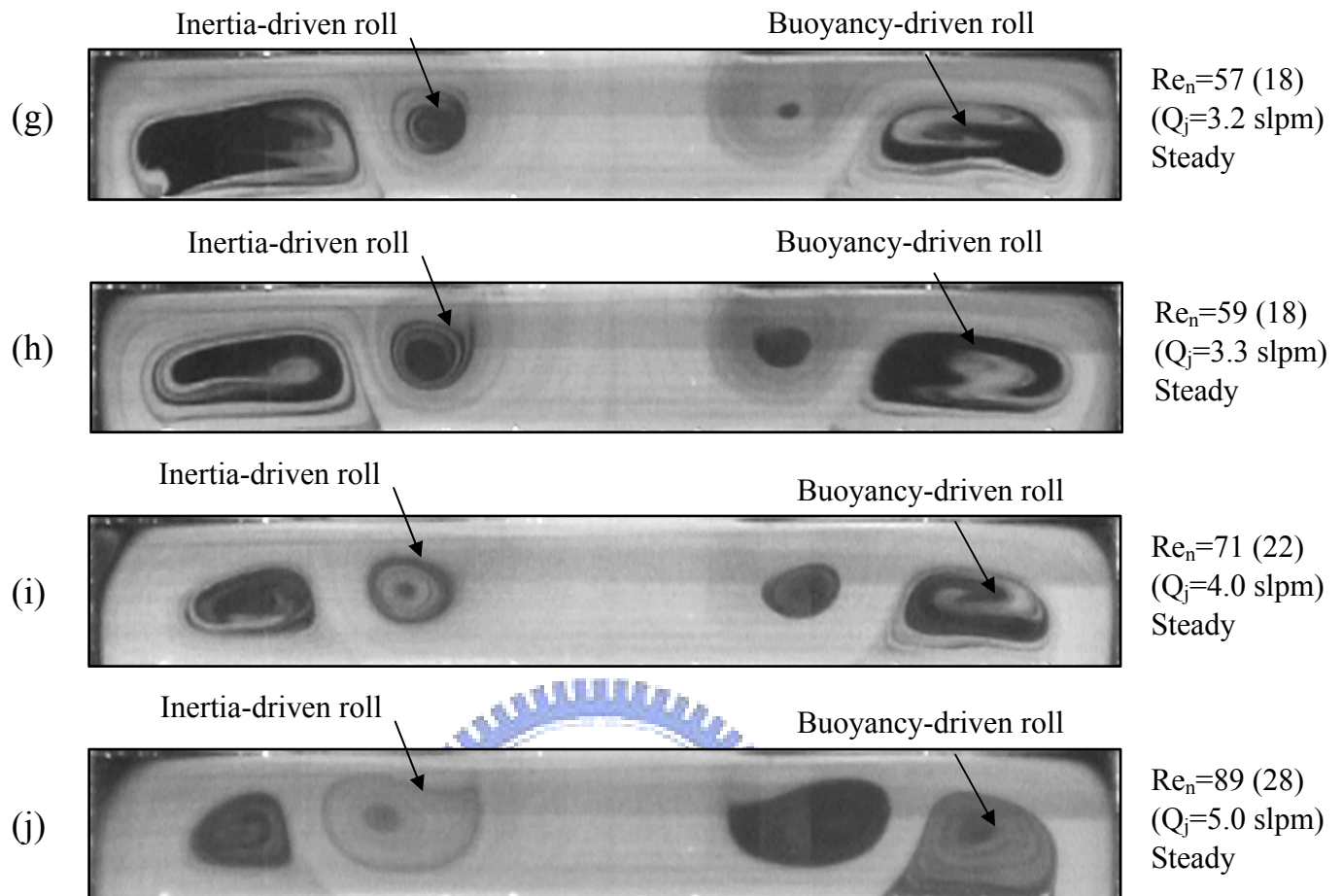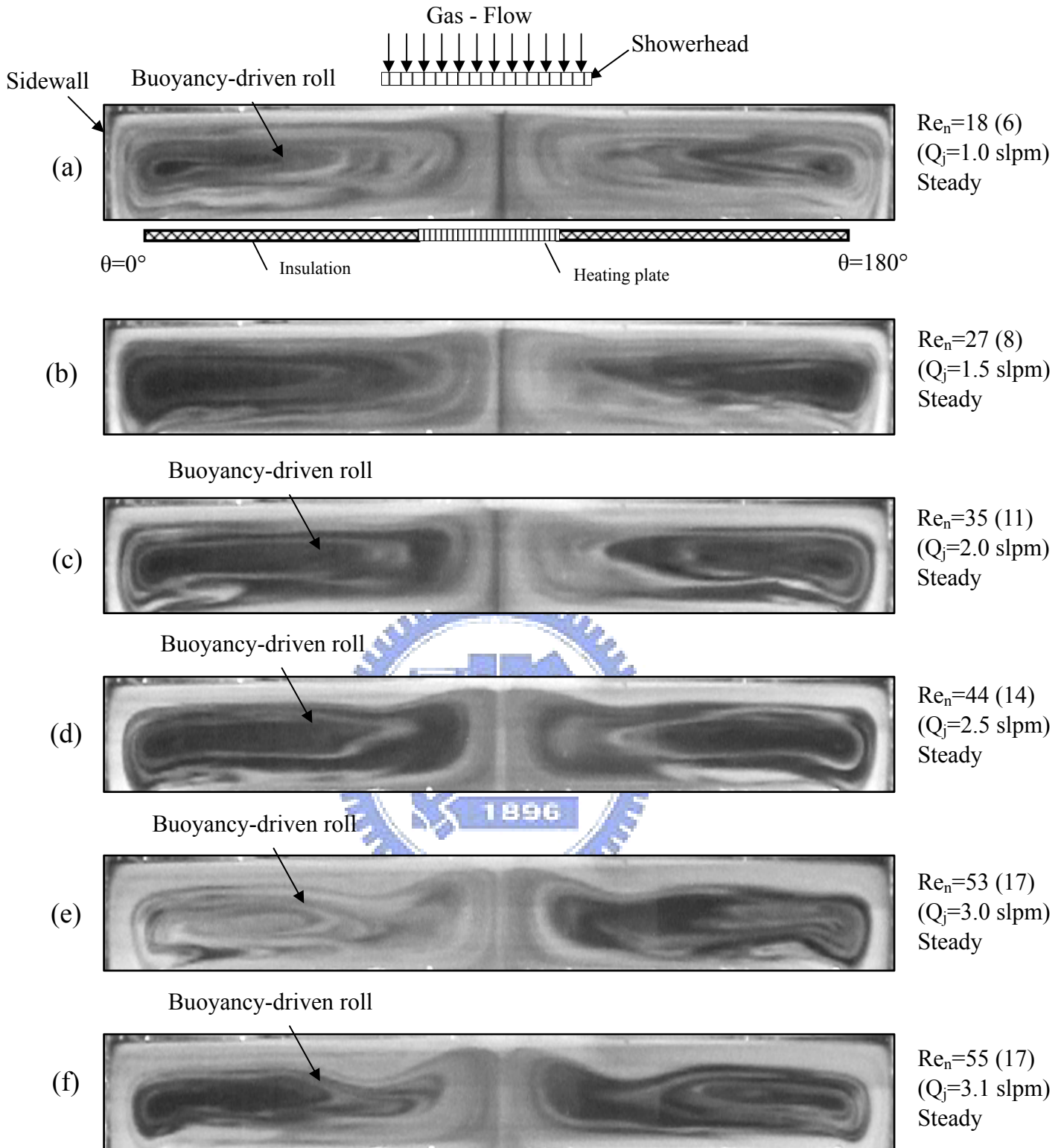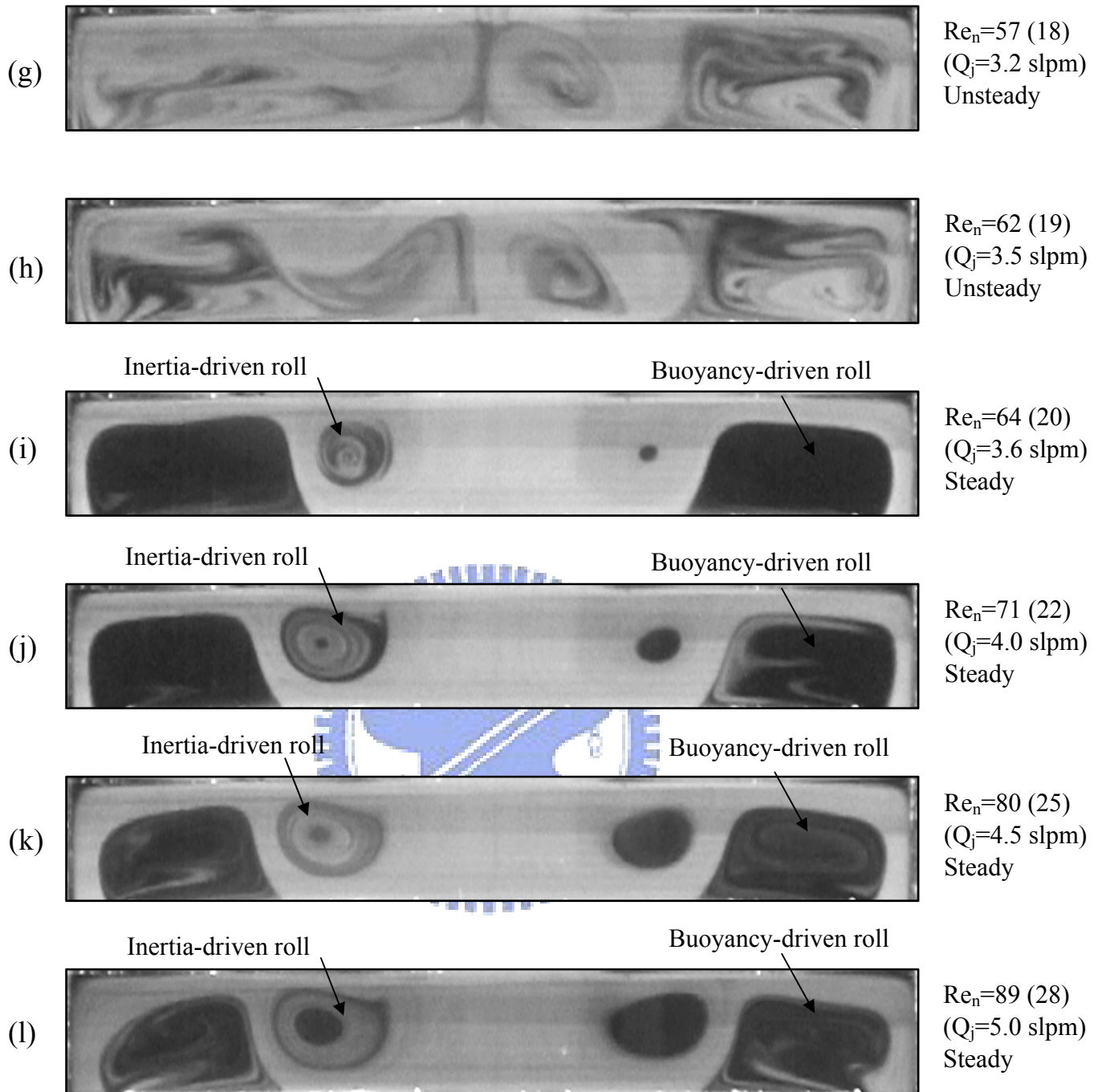( ) : The number in the ( ) is the jet Reynolds number.
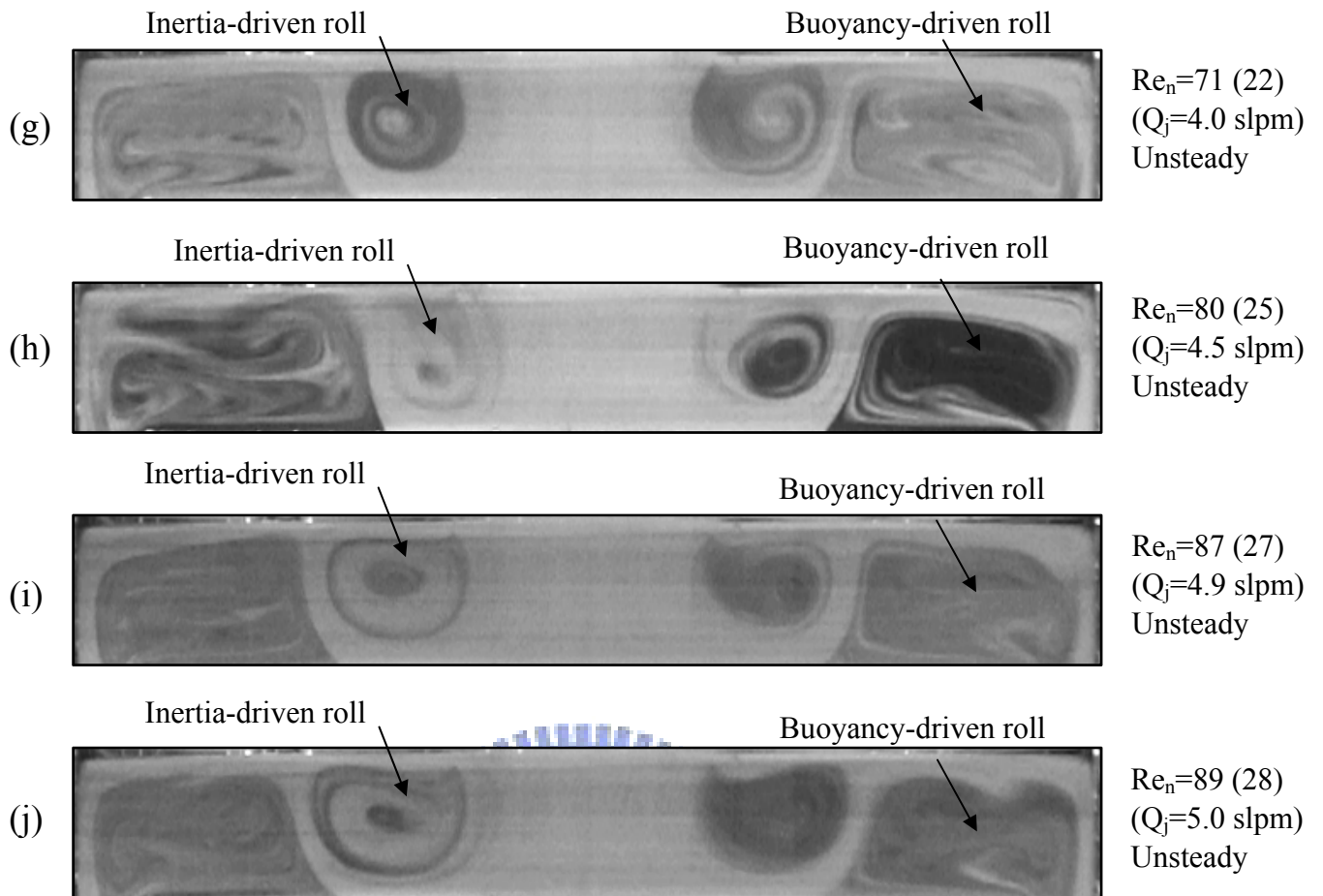
Fig. 4.32 Continued.
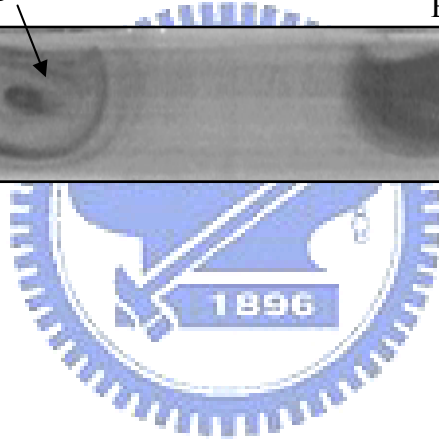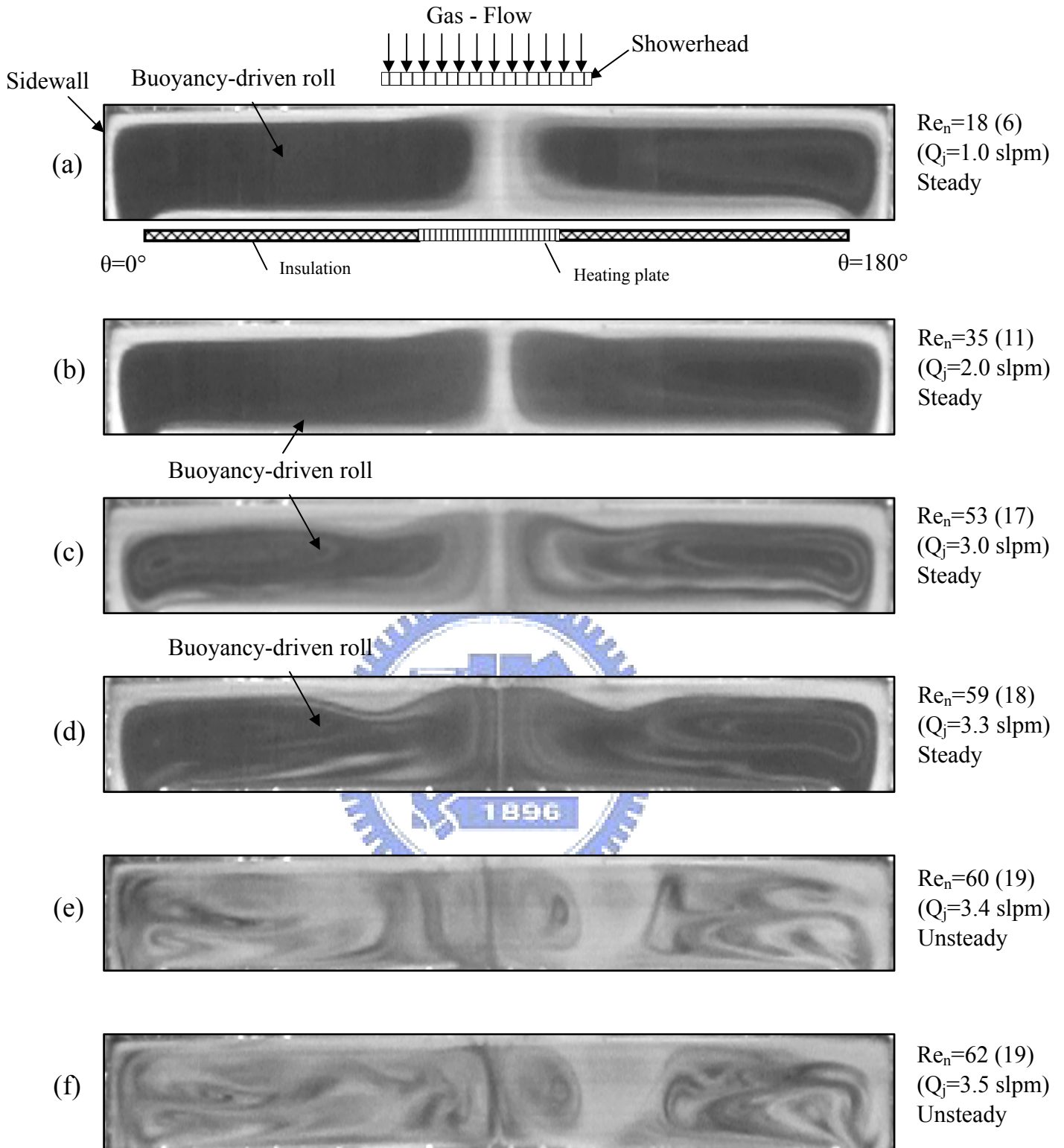
Fig. 4.33 Side view flow photos taken at the cross plane $\theta = 0°$ & $180°$ for various jet Reynolds numbers at Ra = 150,325 ($\Delta T = 25℃$) and H = 40.0 mm for Re_n = (a) 18, (b) 35, (c) 53, (d)59, (e) 60, (f) 62, (g) 71, (h) 80, (i) 89, (j) 98, and (k) 106. ( ) : The number in the ( ) is the jet Reynolds number.

(g) Re_n=71 (22)
(Q_j=4.0 slpm)
Unsteady

Buoyancy-driven roll

(h) Re_n=80 (25)
(Q_j=4.5 slpm)
Unsteady

Inertia-driven roll   Buoyancy-driven roll

(i) Re_n=89 (28)
(Q_j=5.0 slpm)
Unsteady

Inertia-driven roll   Buoyancy-driven roll

(j) Re_n=98 (30)
(Q_j=5.5 slpm)
Unsteady

Inertia-driven roll   Buoyancy-driven roll

(k) Re_n=106 (33)
(Q_j=6.0 slpm)
Unsteady
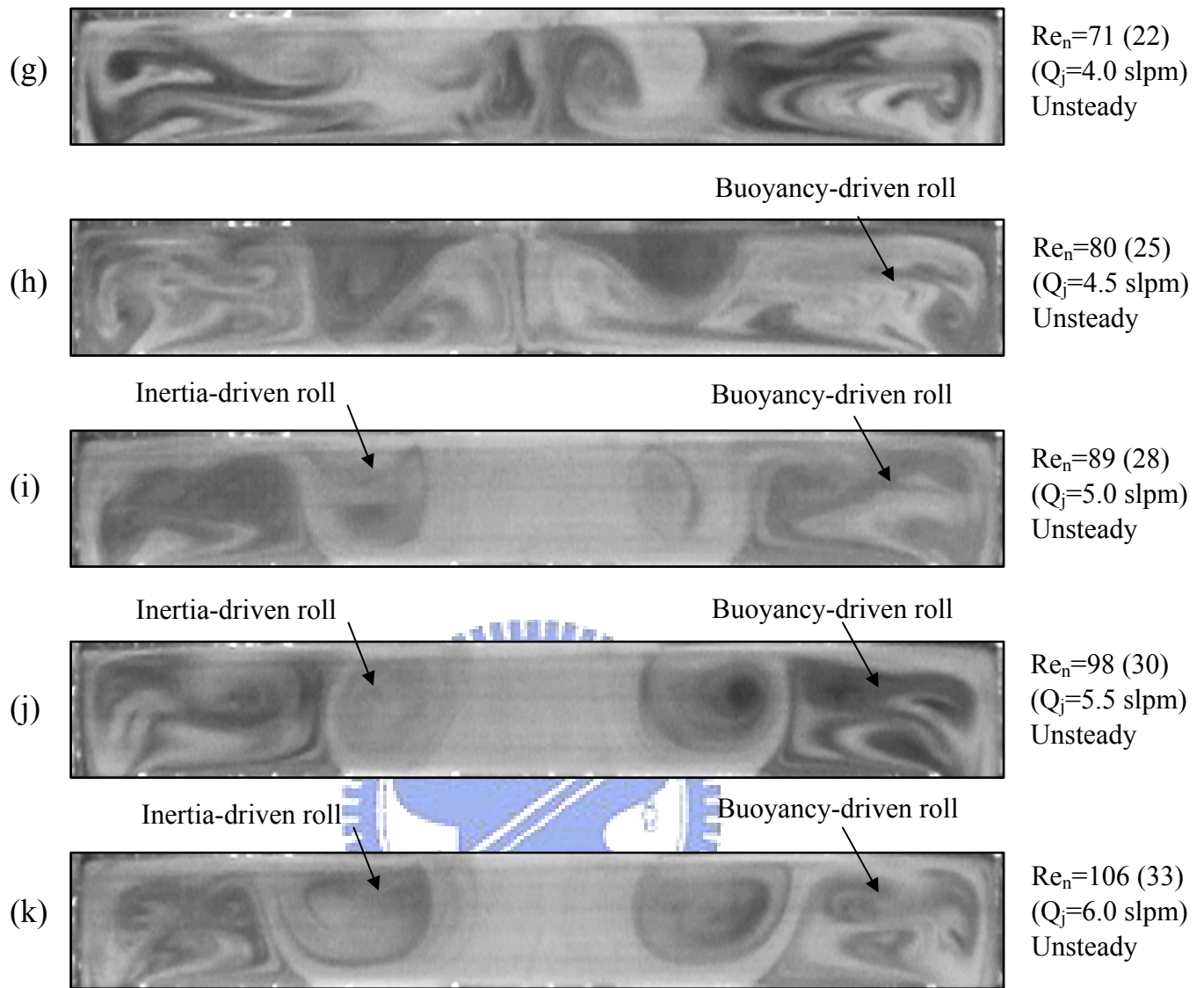
Fig. 4.33   Continued.
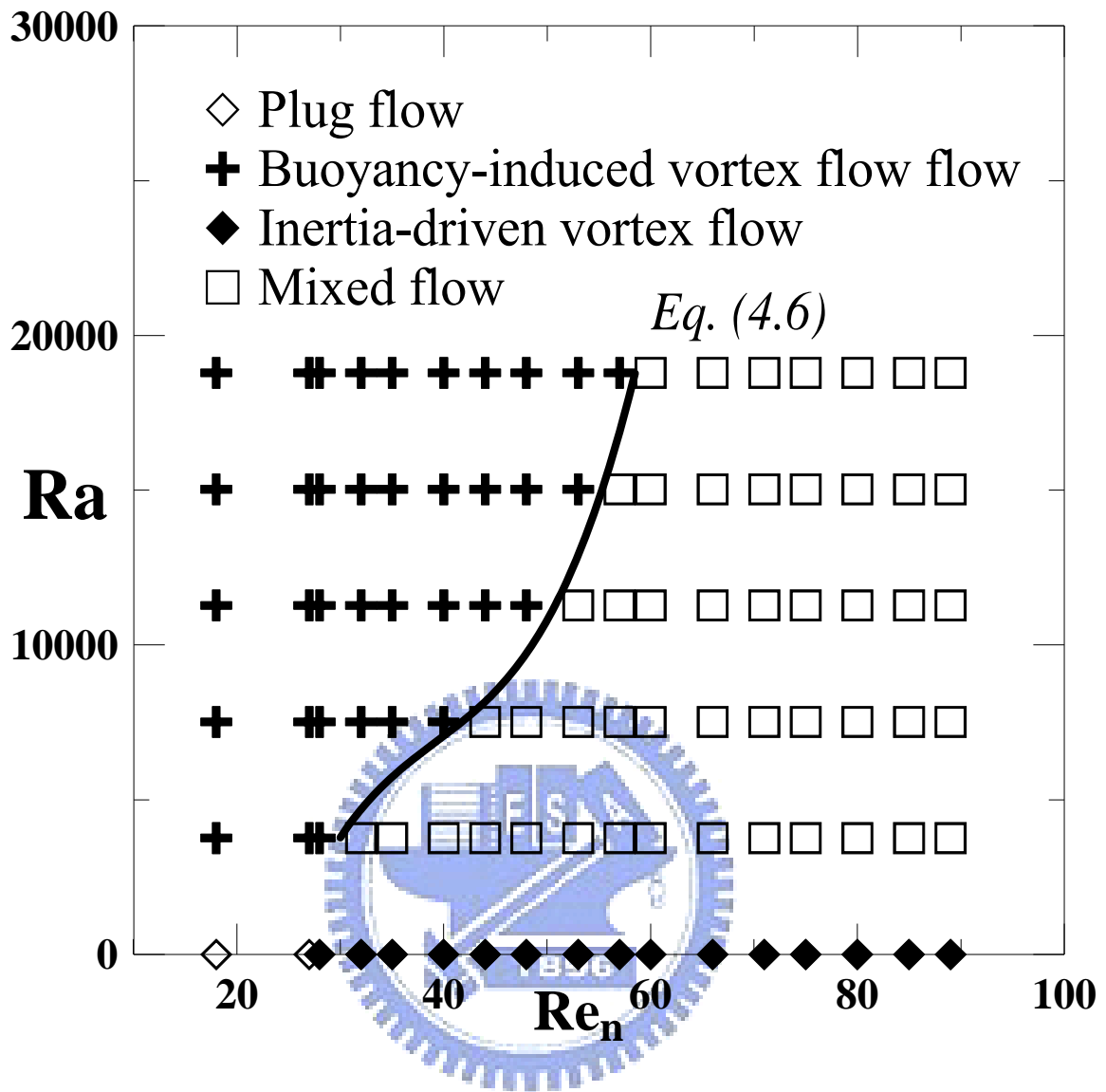
Fig. 4.34 Flow regime map delineating plug flow, buoyancy-induced vortex flow, inertia-driven vortex flow and mixed flow for $H = 20.0$ mm.
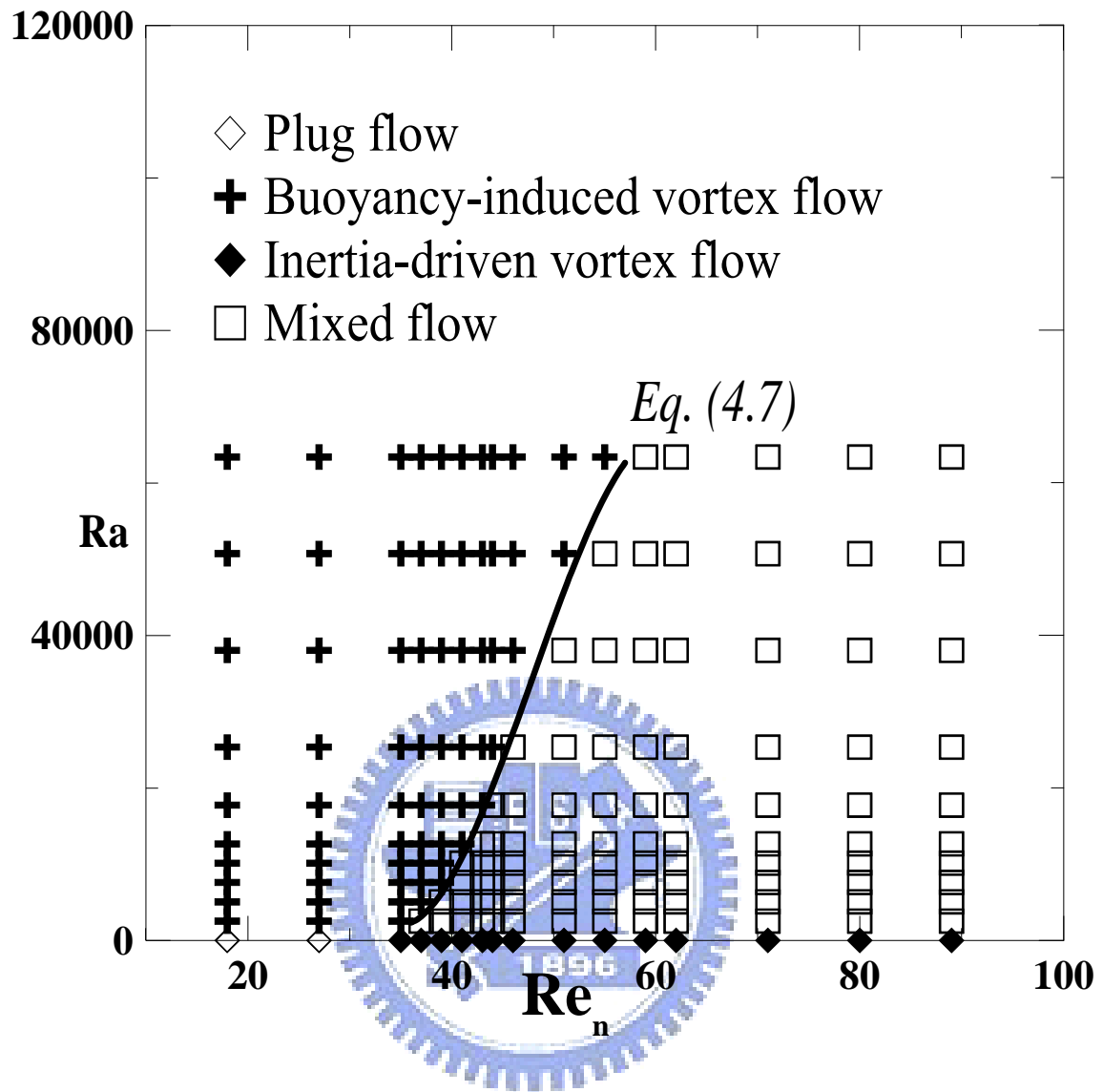
Fig. 4.35 Flow regime map delineating plug flow, buoyancy-induced vortex flow, inertia-driven vortex flow and mixed flow for H = 30.0mm.
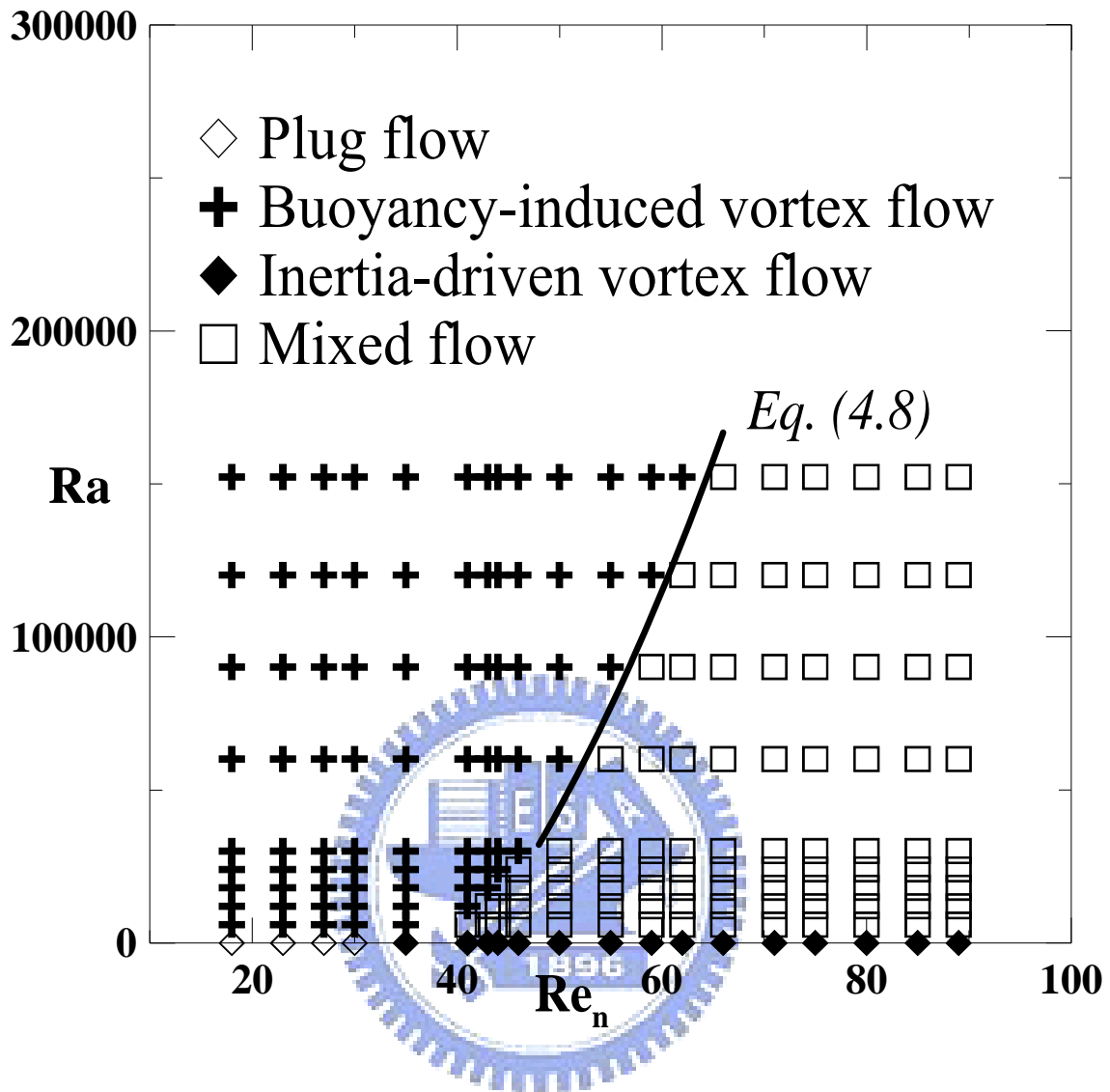
Fig. 4.36 Flow regime map delineating plug flow, buoyancy-induced vortex flow, inertia-driven vortex flow and mixed flow for H = 40.0mm.
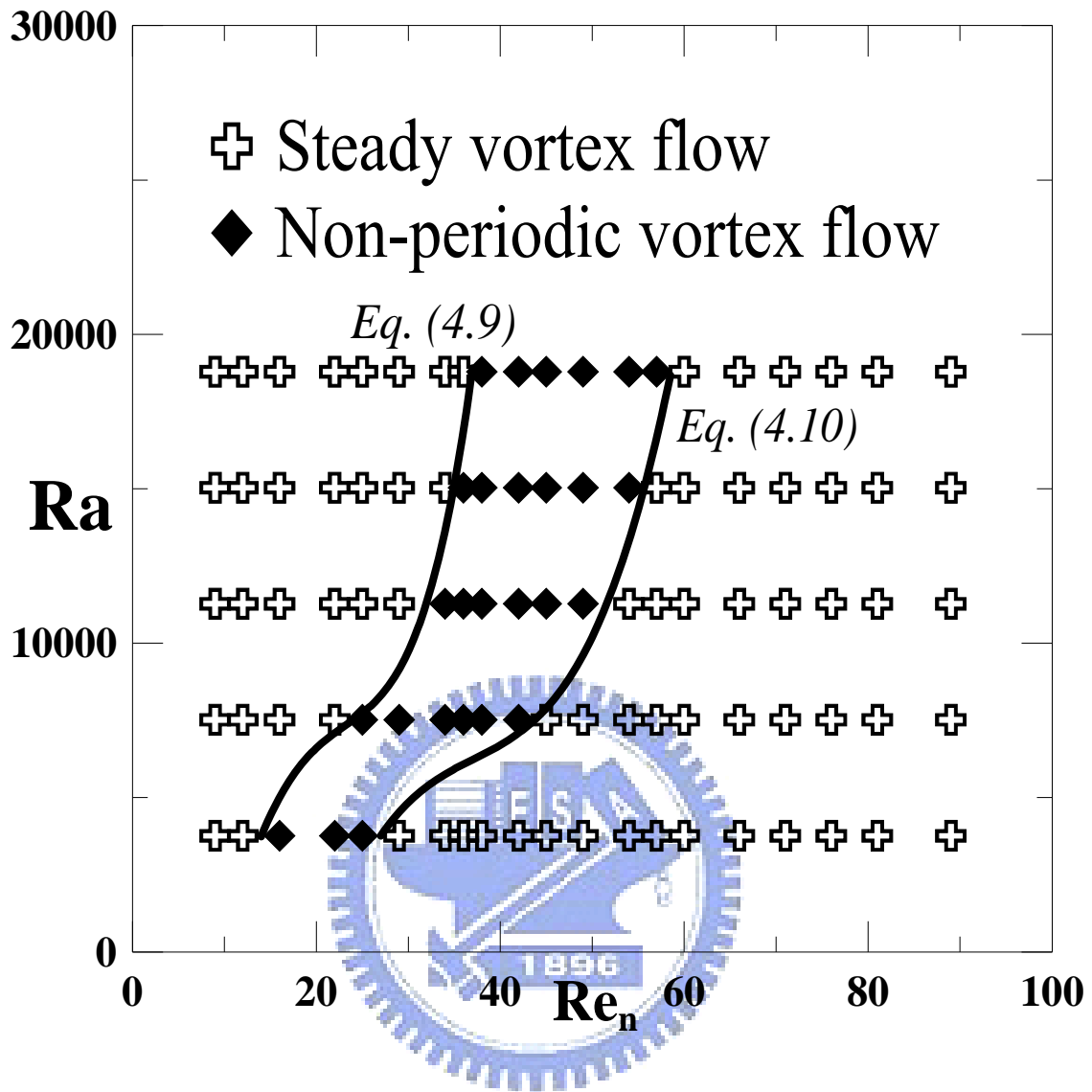
Fig. 4.37   Flow regime map delineating the temporal state of the vortex flow for H = 20.0mm.
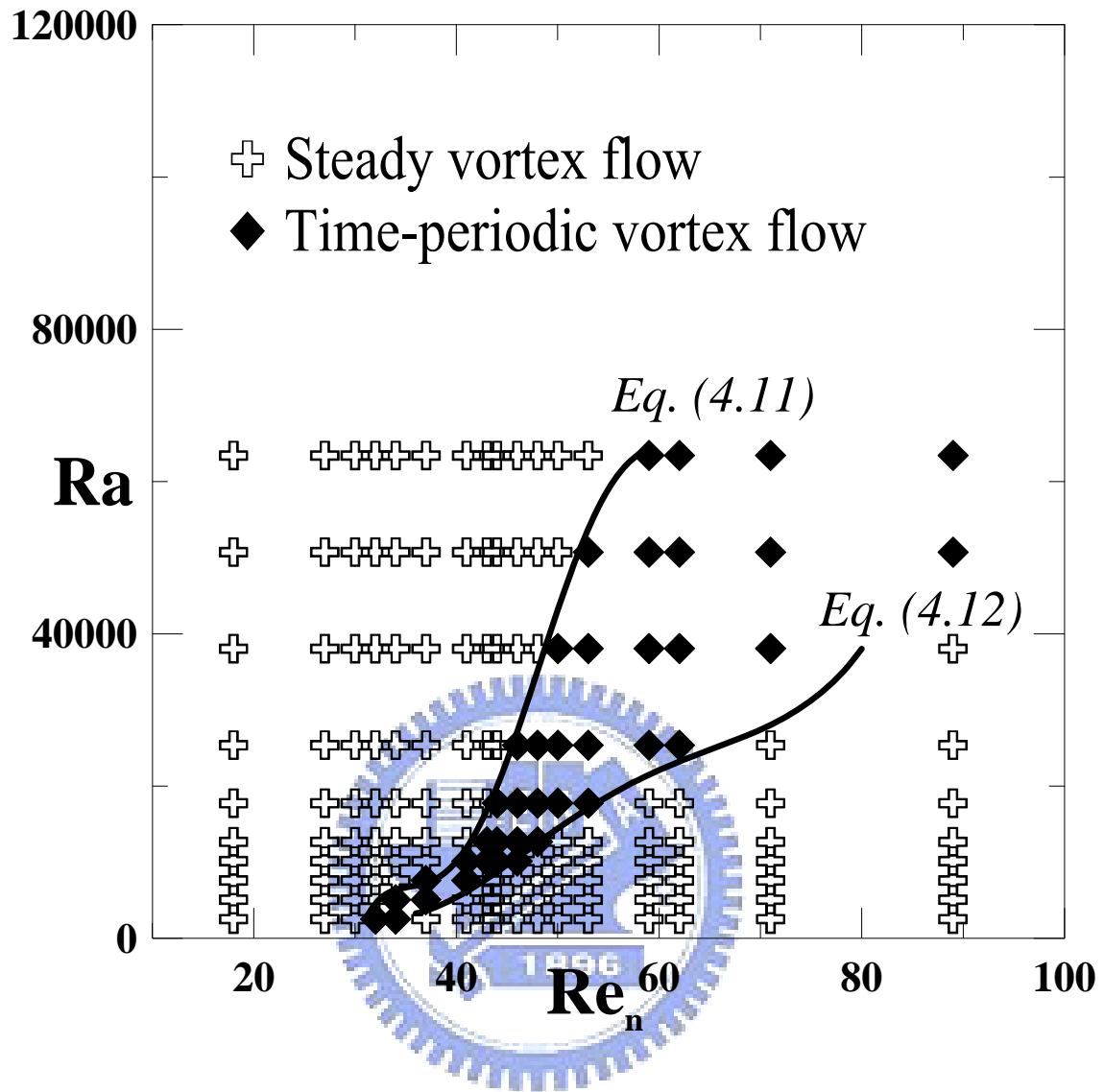
Fig. 4.38 Flow regime map delineating the temporal state of the vortex flow for H = 30.0mm.
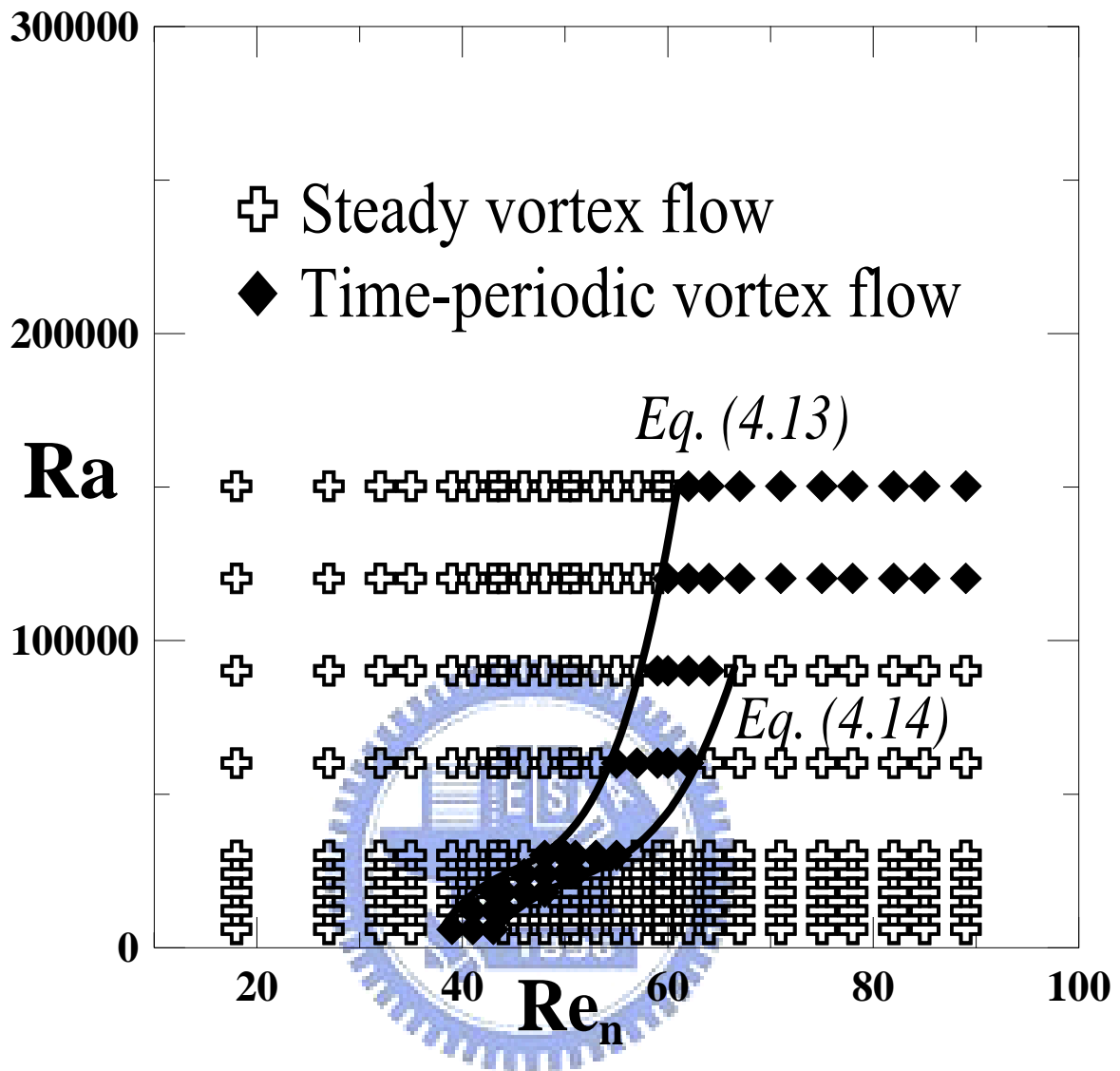
Fig. 4.39   Flow regime map delineating the temporal state of the vortex flow for H = 40.0mm.
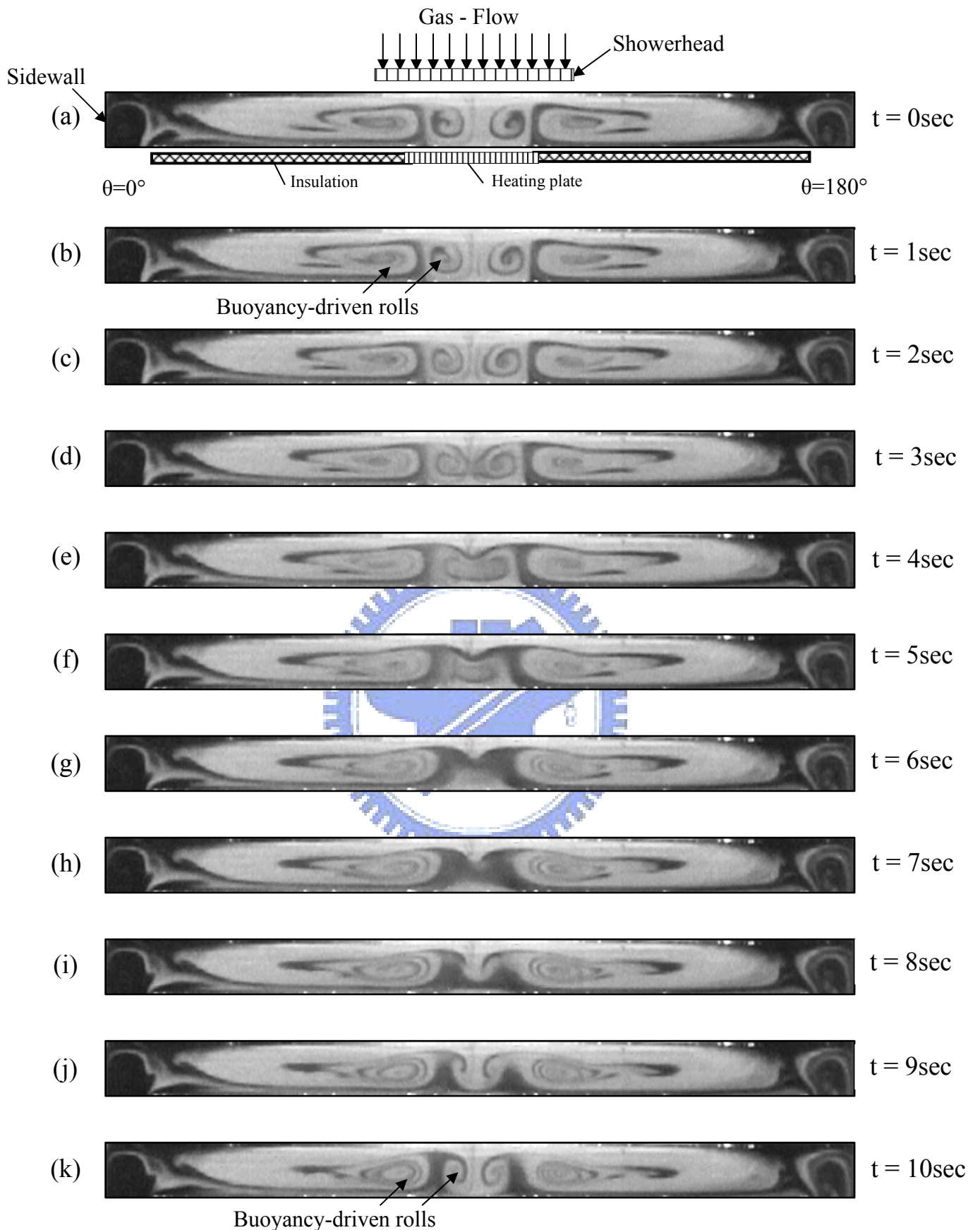
Fig. 4.40 Non-periodic vortex flow for H = 20.0 mm and Ra= 3,758 (ΔT = 5℃) at Re_n = 20 (Q$_j$ = 1.1 slpm, Re$_j$ = 6) illustrated by side view flow photos taken at the cross plane θ = 0° & 180°.

(l)   t = 11sec

Buoyancy-driven rolls

(m   t = 12sec

(n)   t = 13sec

(o)   t = 14sec

(p)   t = 15sec

(q)   t = 16sec

(r)   t = 17sec

(s)   t = 18sec

(t)   t = 19sec
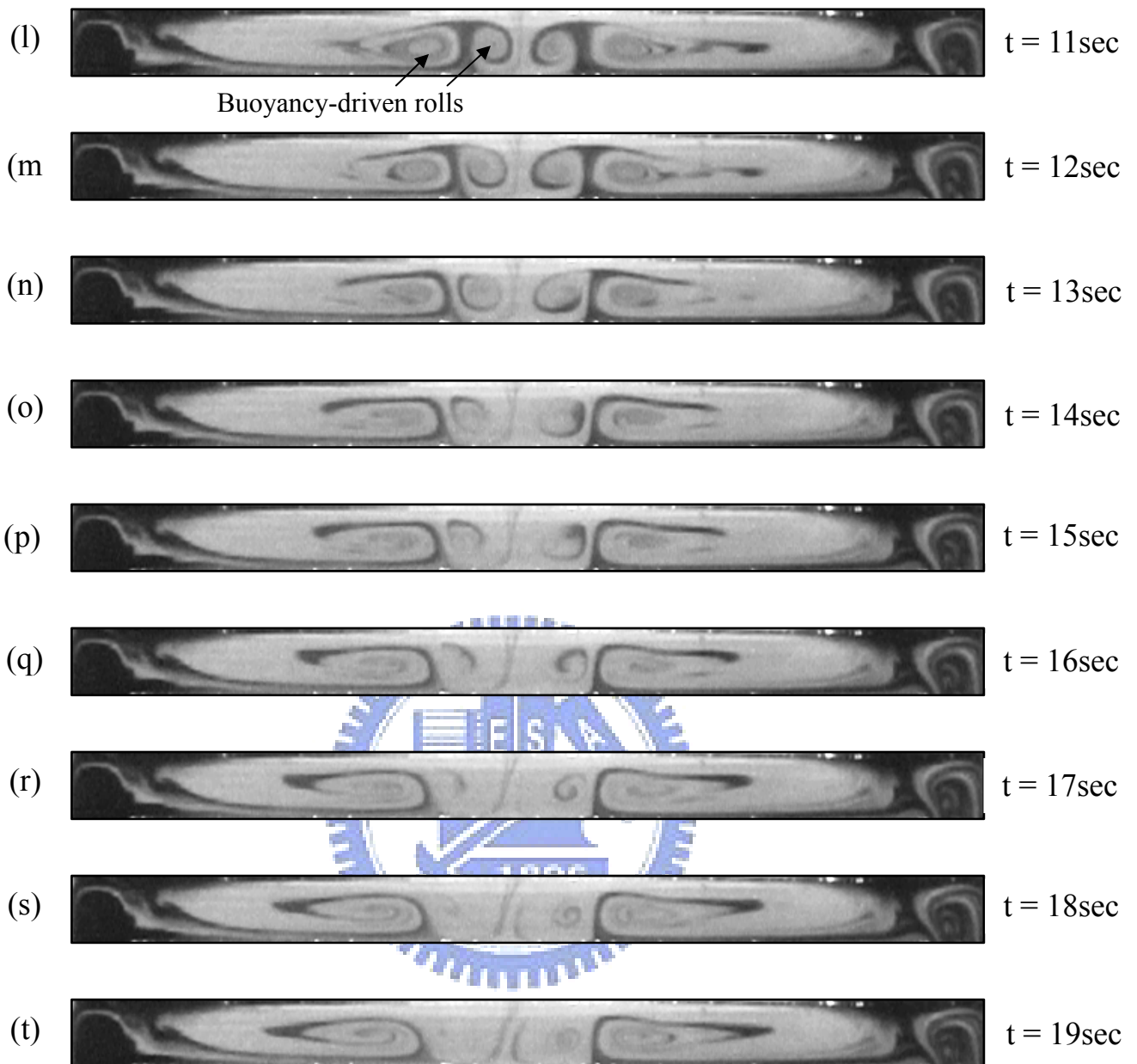
Fig. 4.40 Continued.
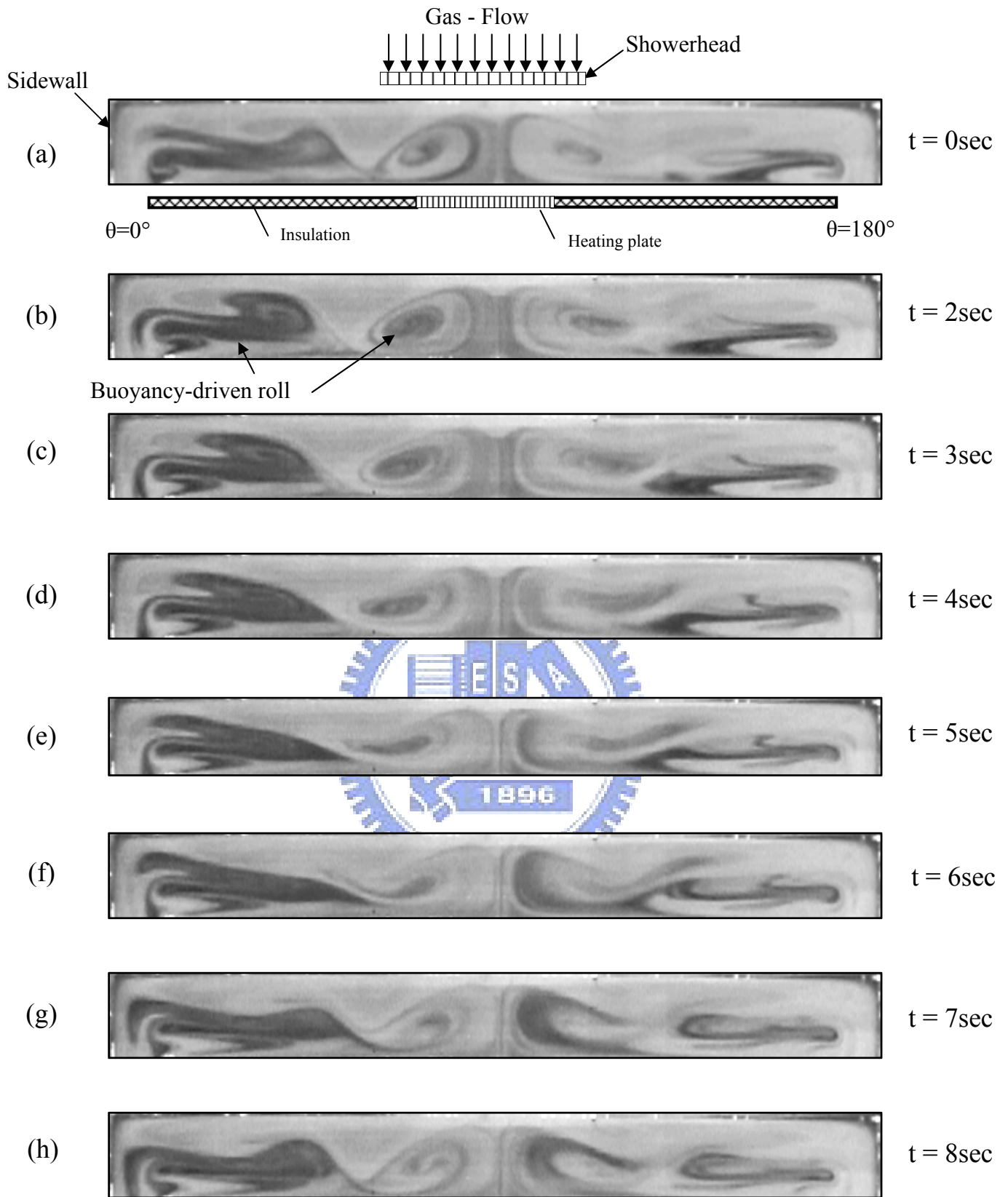
Fig. 4.41 Time-periodic vortex flow for H = 30.0 mm and Ra = 25,367 (ΔT = 10℃) at Re_n = 46 (Q_j = 2.6 slpm, Re_j = 14) illustrated by side view flow photos taken at the cross plane θ = 0° & 180° at selected time instants in a typical periodic cycle (t_p = 8.0 sec).
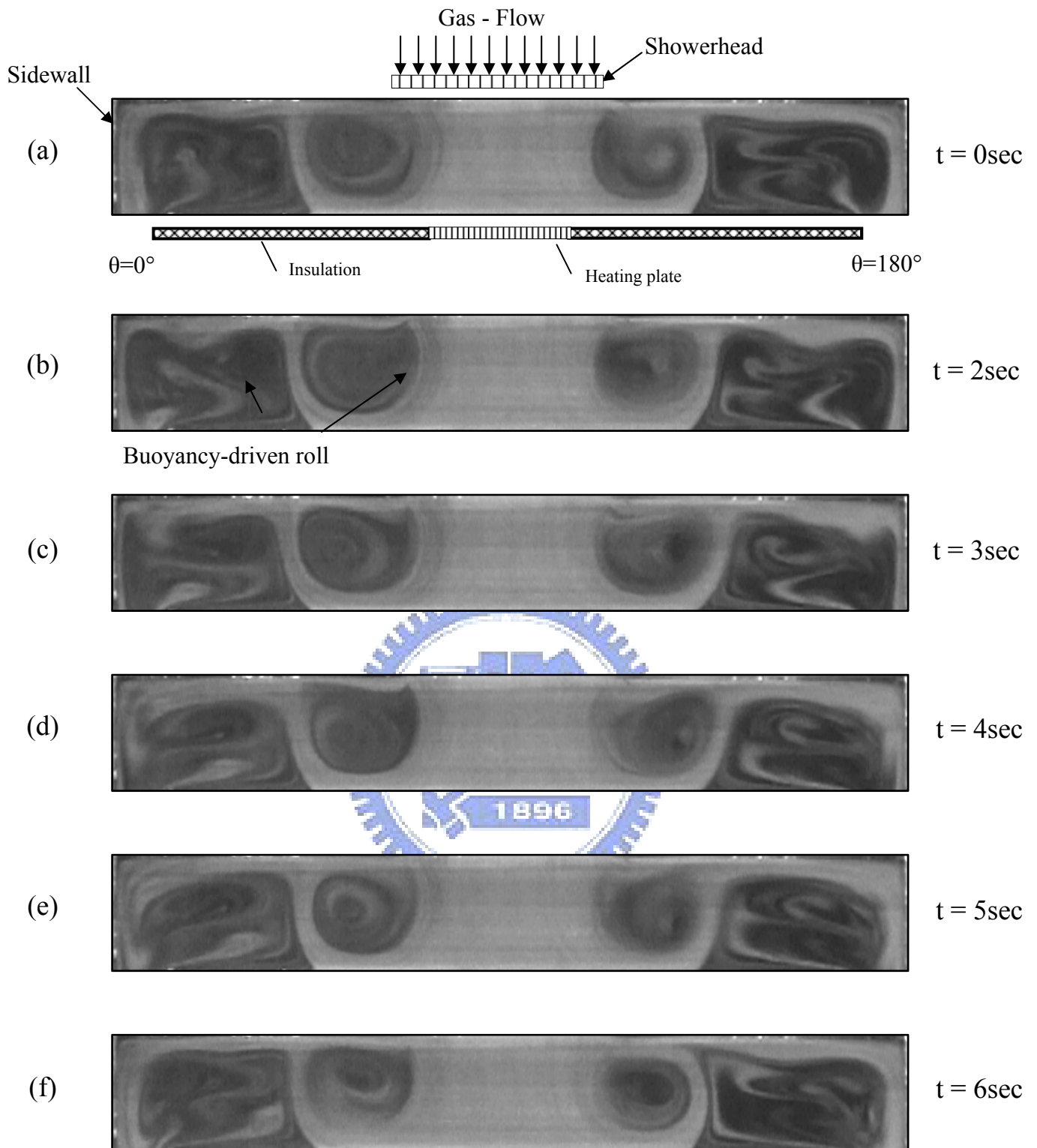
Fig. 4.42 Time-periodic vortex flow for H = 40.0 mm and Ra = 120,260 (ΔT = 20℃) at Re_n = 89 (Q_j = 5.0 slpm, Re_j = 28) illustrated by side view flow photos taken at the cross plane θ = 0° & 180° at selected time instants in a typical periodic cycle (t_p = 6.0 sec).

Without showerhead

V_n

Bakelite plate

Heated disk

(a)

With showerhead

V_j

Bakelite plate

Heated disk

(b)
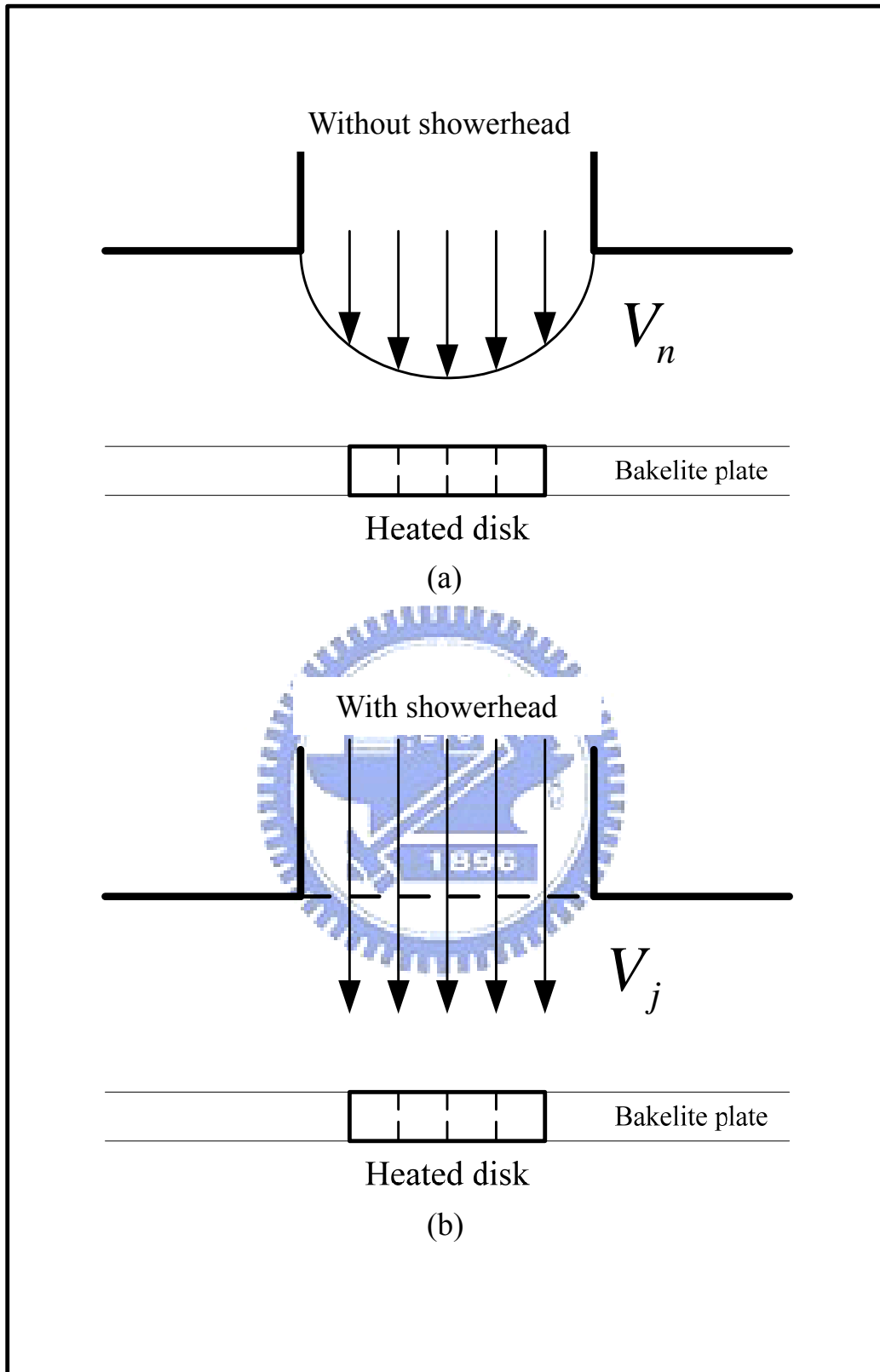
Fig. 4.43　Schematic illustration of the velocity distribution at the gas injection nozzle for the chamber without showerhead (a) and with showerhead (b).
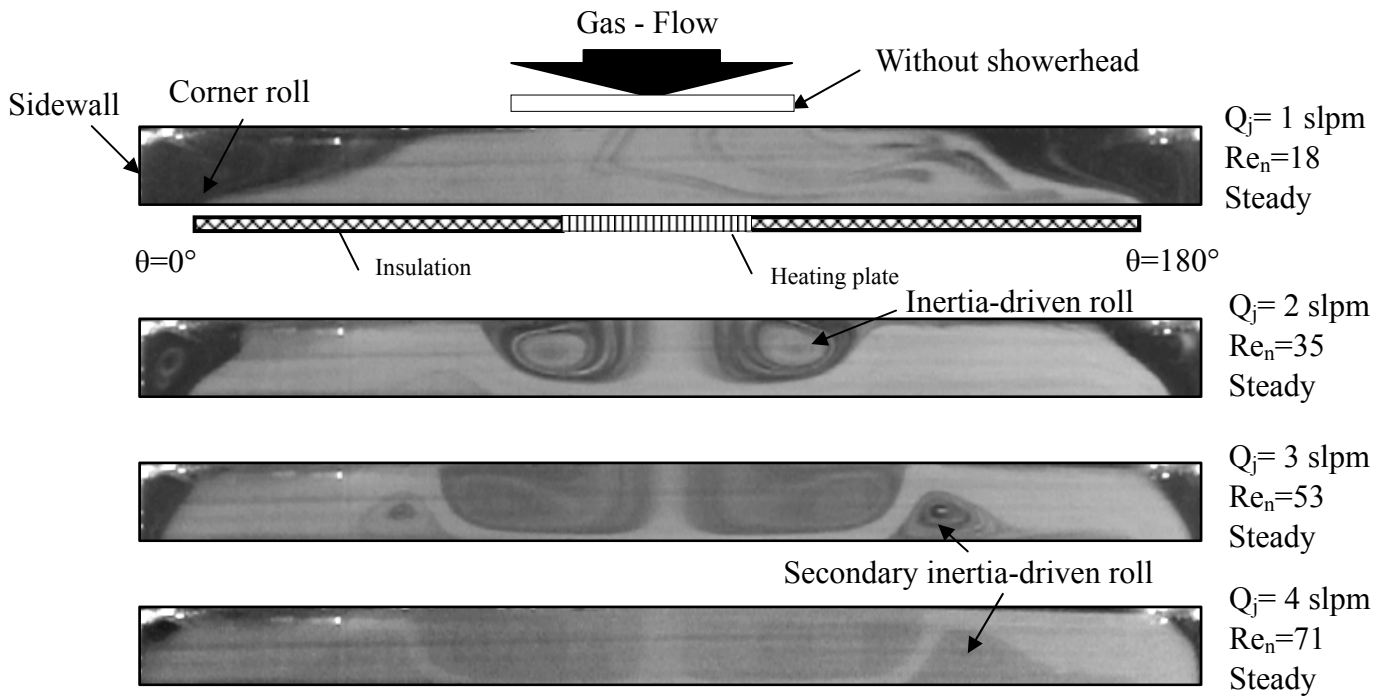
(a) Vortex flow without showerhead installation
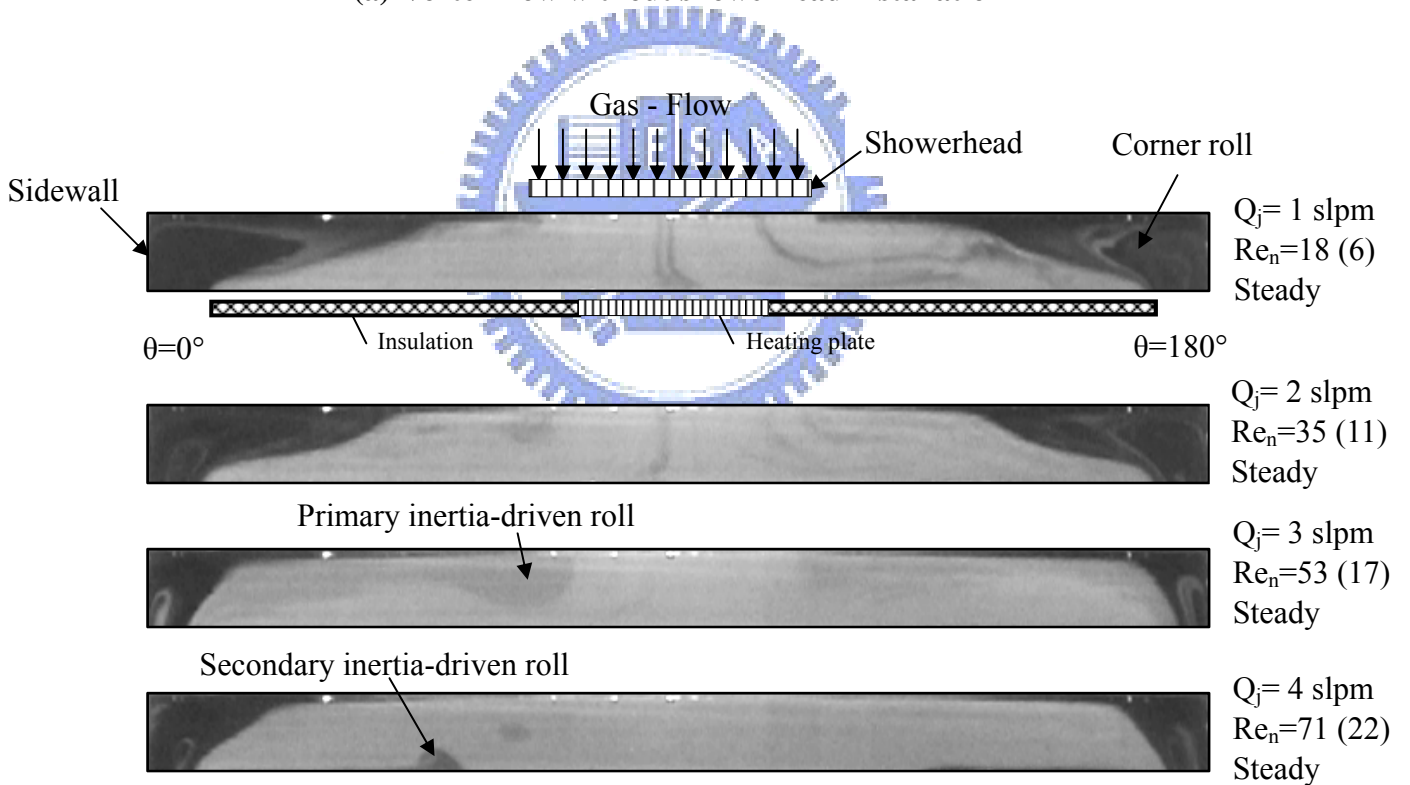
(b) Vortex flow with showerhead installation

Fig. 4.44   Side view flow photos taken at the cross plane $\theta = 0°$ & $180°$ for various Q_j at $\Delta T = 0$ (Ra = 0) and H = 20.0 mm.

( ) : The number in the ( ) is the jet Reynolds number.
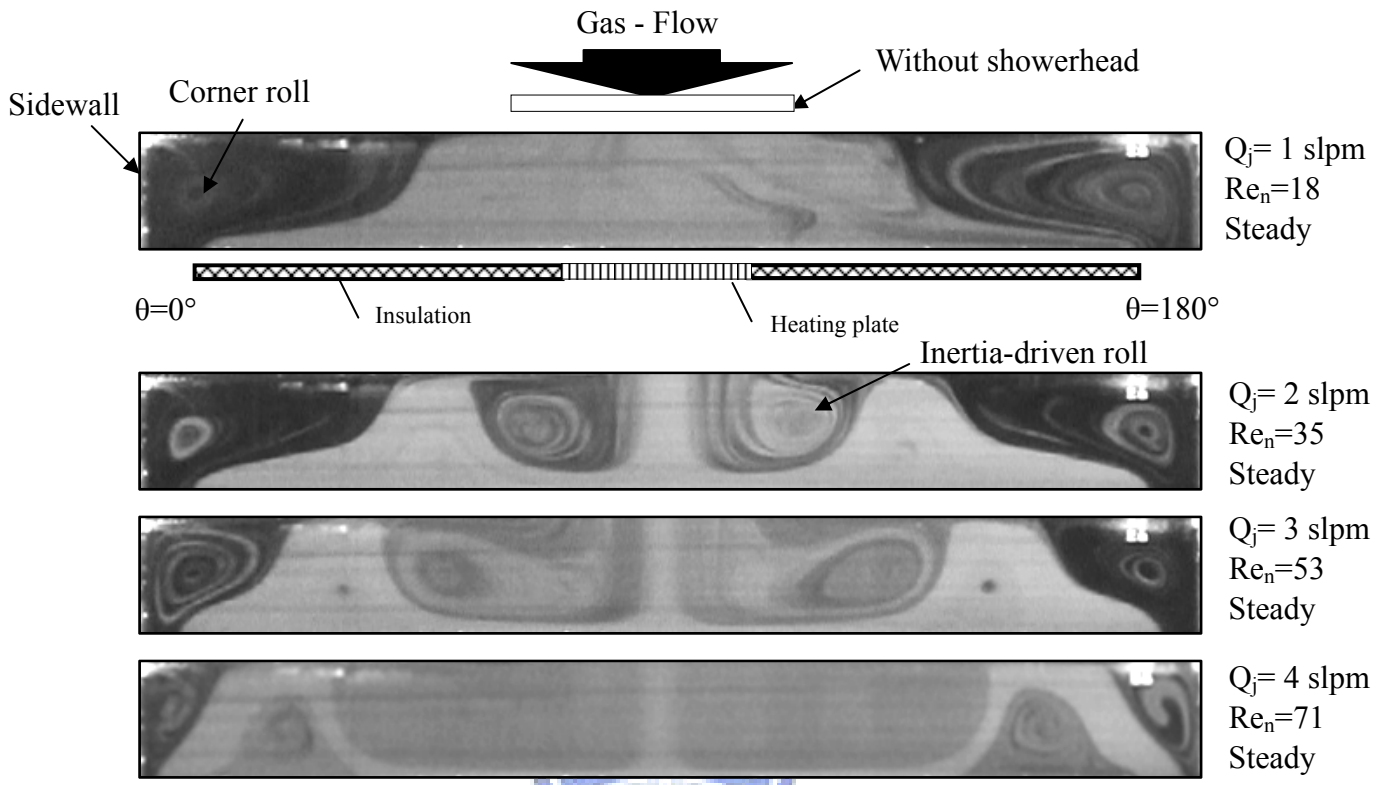
Gas - Flow

Without showerhead

Sidewall   Corner roll

θ=0°   Insulation   Heating plate   θ=180°

Q_j= 1 slpm
Re_n=18
Steady

Inertia-driven roll

Q_j= 2 slpm
Re_n=35
Steady

Q_j= 3 slpm
Re_n=53
Steady

Q_j= 4 slpm
Re_n=71
Steady

(a) Vortex flow without showerhead installation

Gas - Flow

Showerhead   Corner roll

Sidewall

θ=0°   Insulation   Heating plate   θ=180°

Q_j= 1 slpm
Re_n=18 (6)
Steady

Q_j= 2 slpm
Re_n=35 (11)
Steady

Q_j= 3 slpm
Re_n=53 (17)
Steady

Q_j= 4 slpm
Re_n=71 (22)
Steady

(b) Vortex flow with showerhead installation

Fig. 4.45   Side view flow photos taken at the cross plane θ = 0° & 180° for various Q_j at ΔT =
0 (Ra = 0) and H = 30.0 mm.

( ) : The number in the ( ) is the jet Reynolds number.

(a) Vortex flow without showerhead installation

(b) Vortex flow with showerhead installation
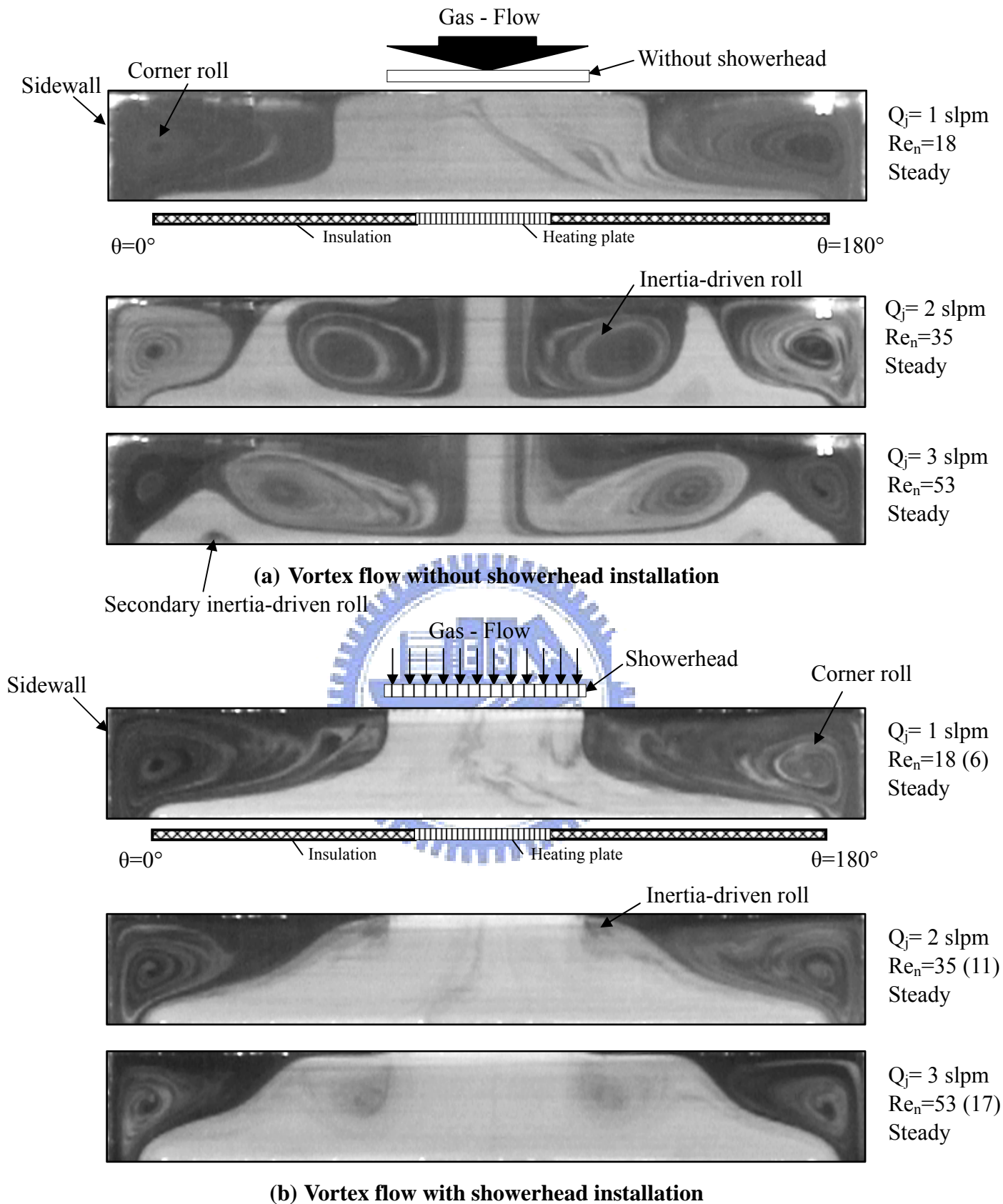
Fig. 4.46   Side view flow photos taken at the cross plane $\theta = 0°$ & $180°$ for various Q_j at $\Delta T =$
0 (Ra = 0) and H = 40.0 mm.

( ) : The number in the ( ) is the jet Reynolds number.
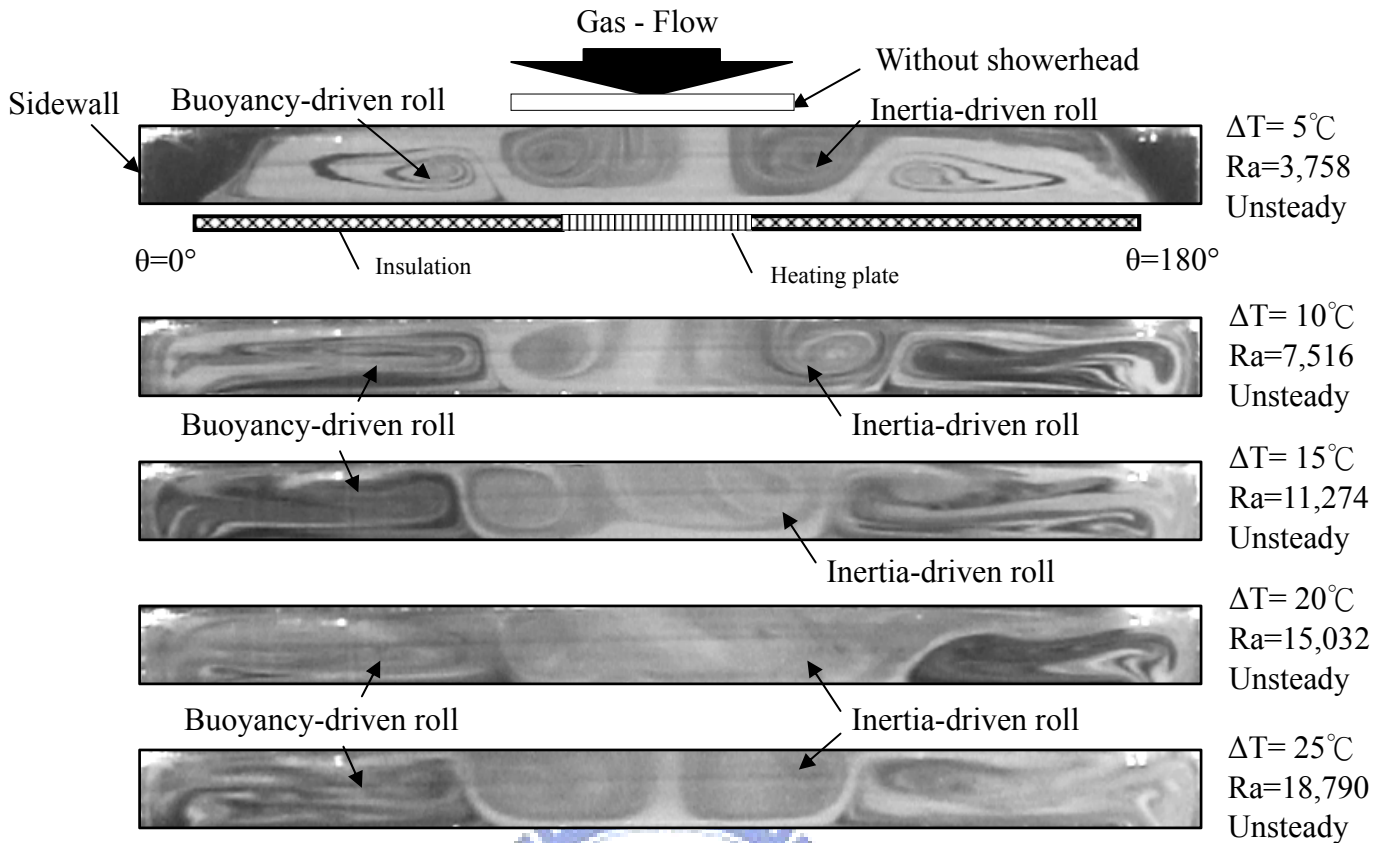
(a) Vortex flow without showerhead installation
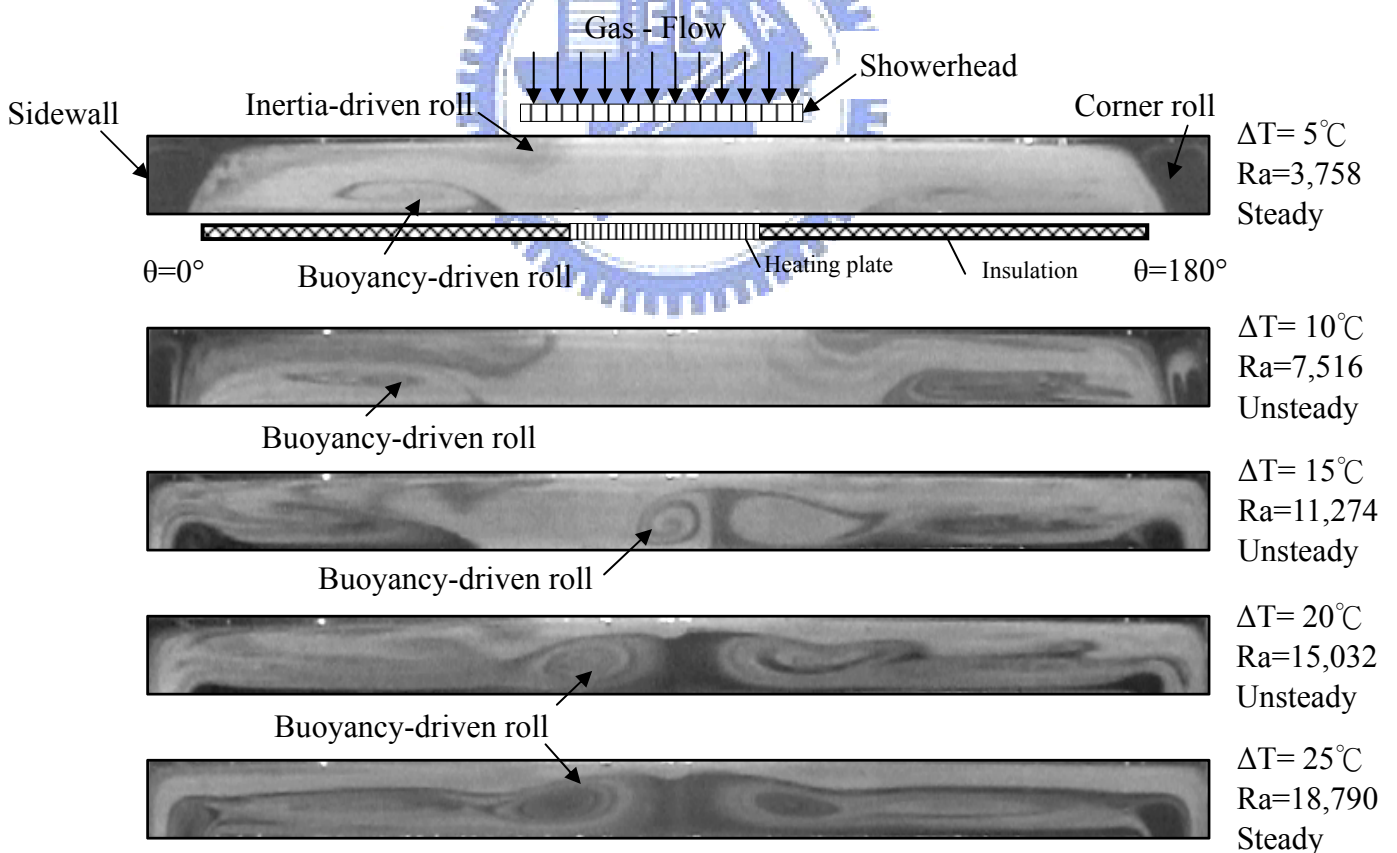
(b) Vortex flow with showerhead installation

Fig. 4.47 Side view flow photos taken at the cross plane θ = 0° & 180° for various ΔT at Q_j = 2 slpm (Re_n = 35, Re_j = 11) and H = 20.0 mm.
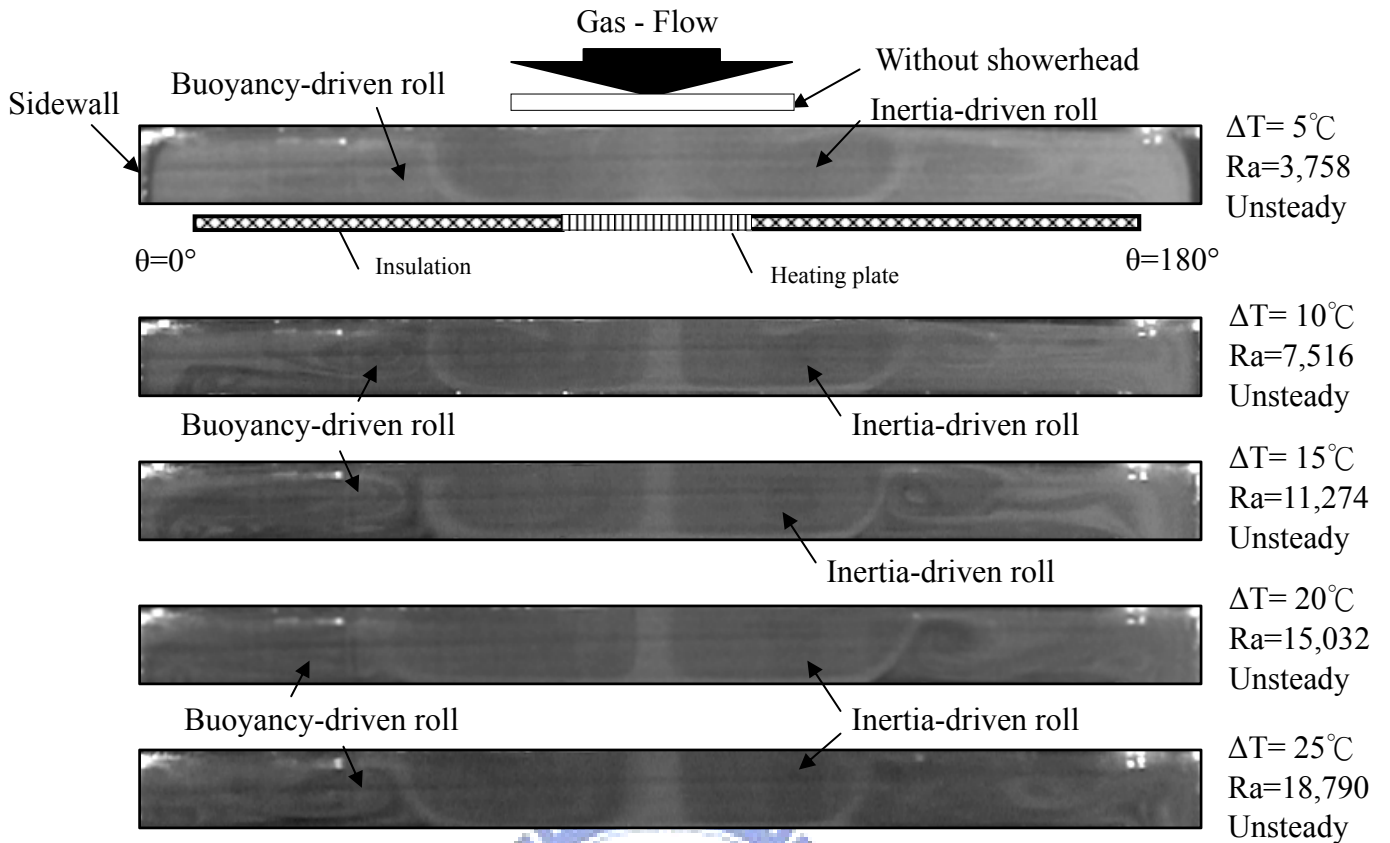
(a) Vortex flow without showerhead installation
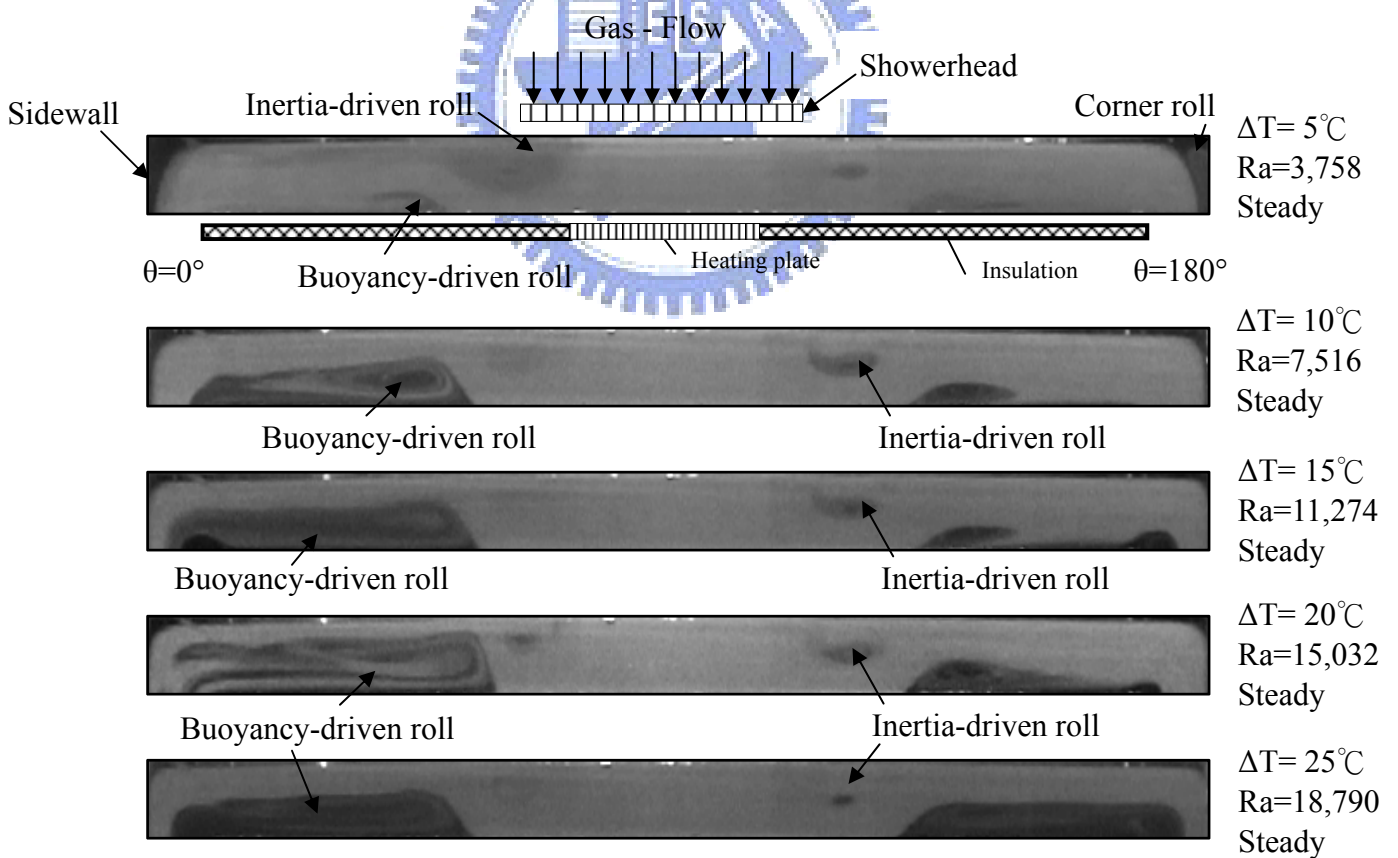
(b) Vortex flow with showerhead installation

Fig. 4.48   Side view flow photos taken at the cross plane $\theta = 0°$ & $180°$ for various ΔT at $Q_j =$ 4 slpm ($Re_n = 71$, $Re_j = 22$) and H = 20.0 mm.
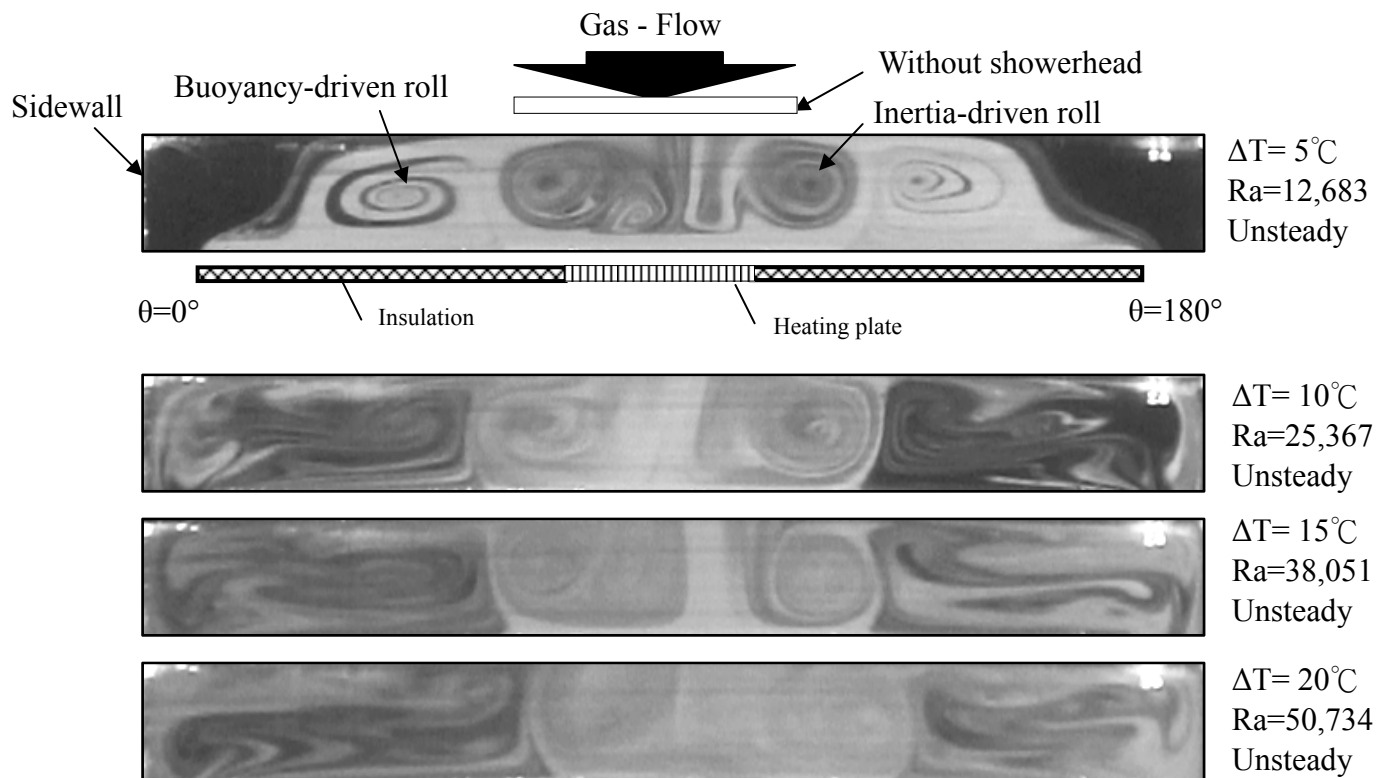
(a) Vortex flow without showerhead installation
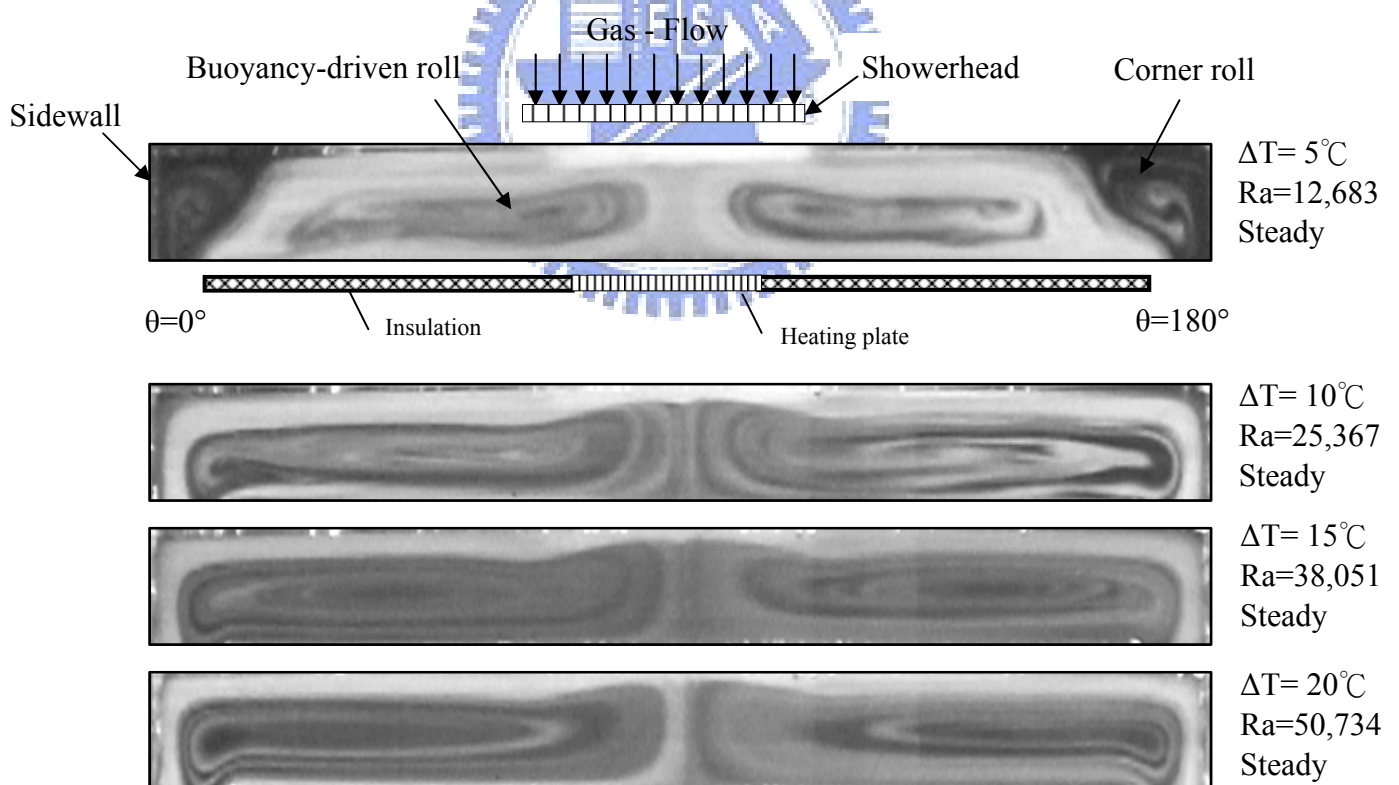
(b) Vortex flow with showerhead installation

Fig. 4.49 Side view flow photos taken at the cross plane $\theta = 0°$ & $180°$ for various ΔT at $Q_j =$ 2 slpm ($Re_n = 35$, $Re_j = 11$) and $H = 30.0$ mm.
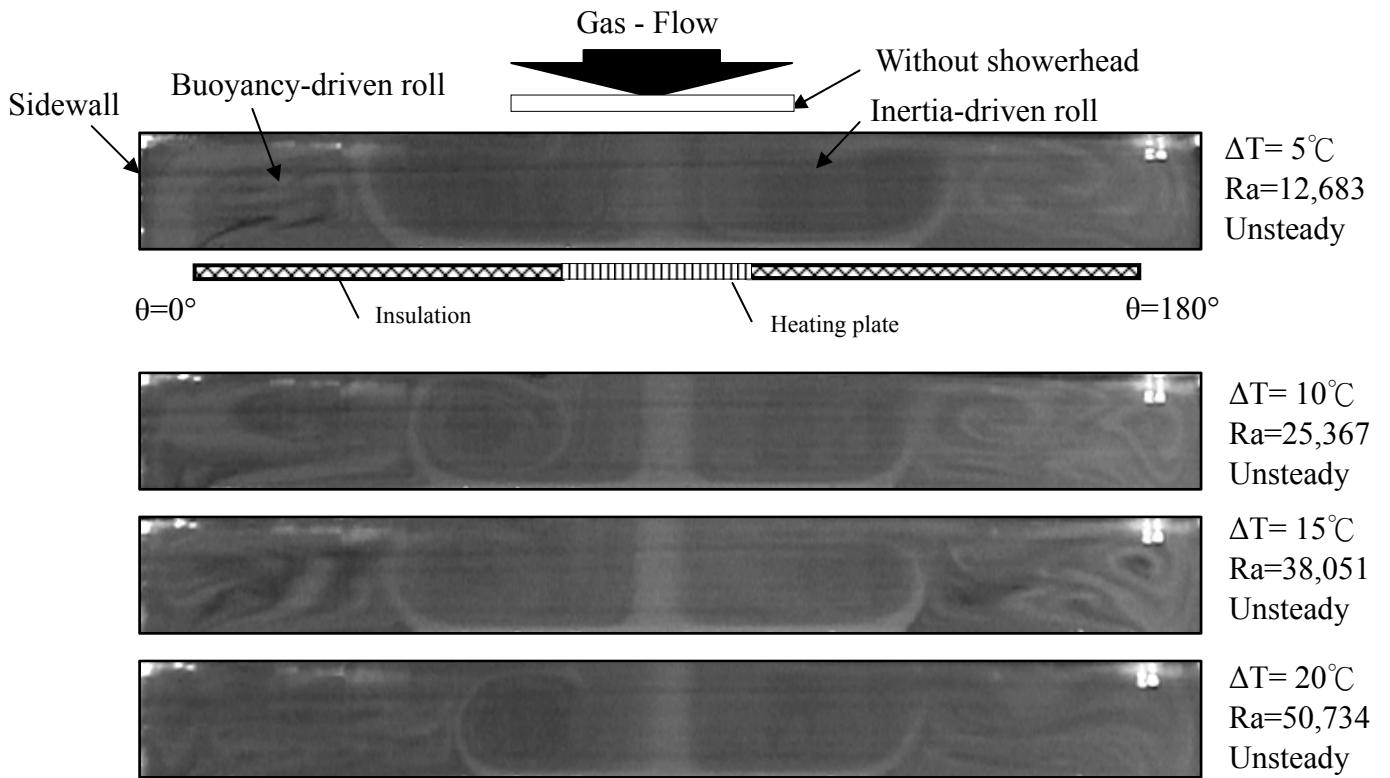
(a) Vortex flow without showerhead installation
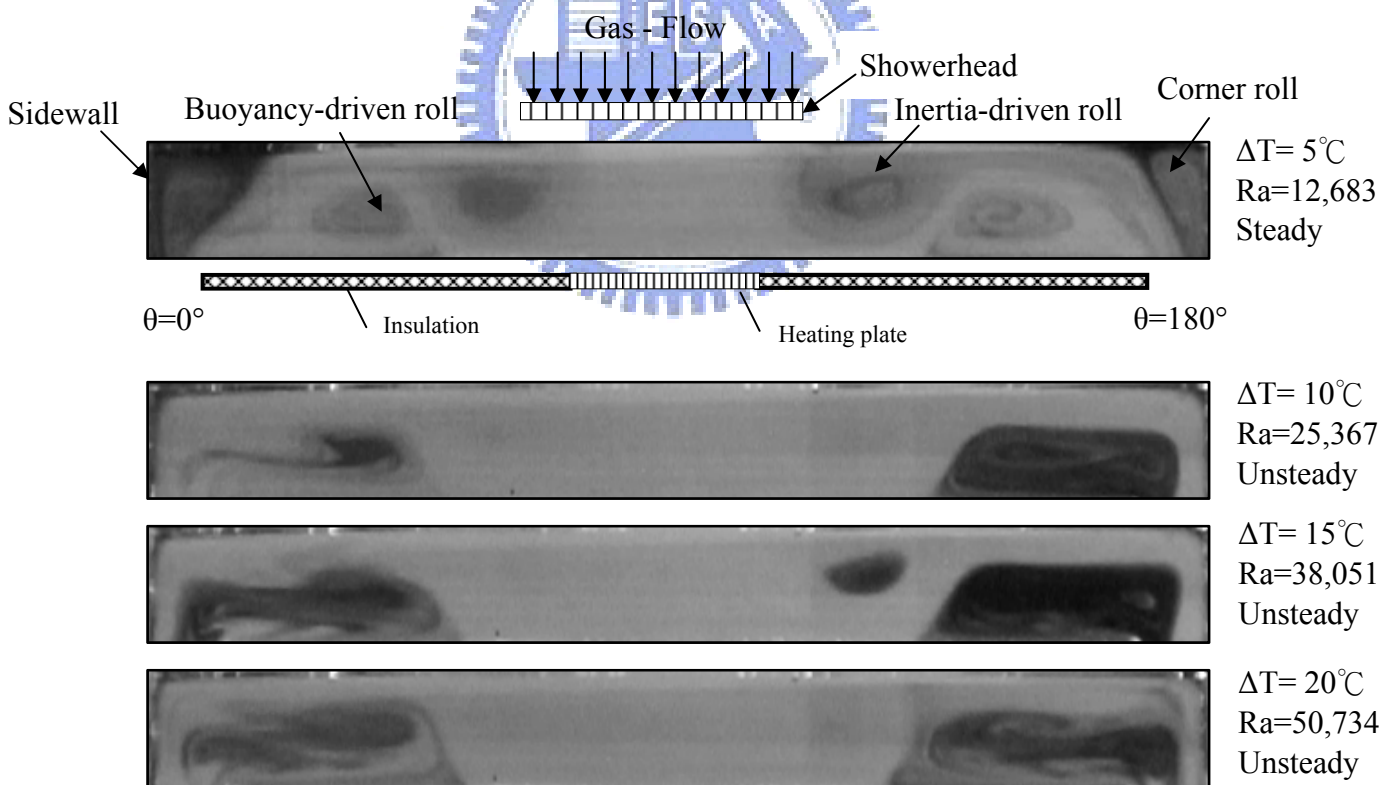
(b) Vortex flow with showerhead installation

Fig. 4.50 Side view flow photos taken at the cross plane $\theta = 0°$ & $180°$ for various ΔT at $Q_j =$ 4 slpm ($Re_n = 71$, $Re_j = 22$) and $H = 30.0$ mm.

Gas - Flow

Sidewall   Buoyancy-driven roll   Without showerhead   Inertia-driven roll

θ=0°   Insulation   Heating plate   θ=180°

ΔT= 5℃
Ra=30,065
Unsteady

ΔT= 10℃
Ra=60,130
Unsteady

ΔT= 15℃
Ra=90,195
Unsteady

ΔT= 20℃
Ra=120,260
Unsteady

ΔT= 25℃
Ra=150,325
Unsteady
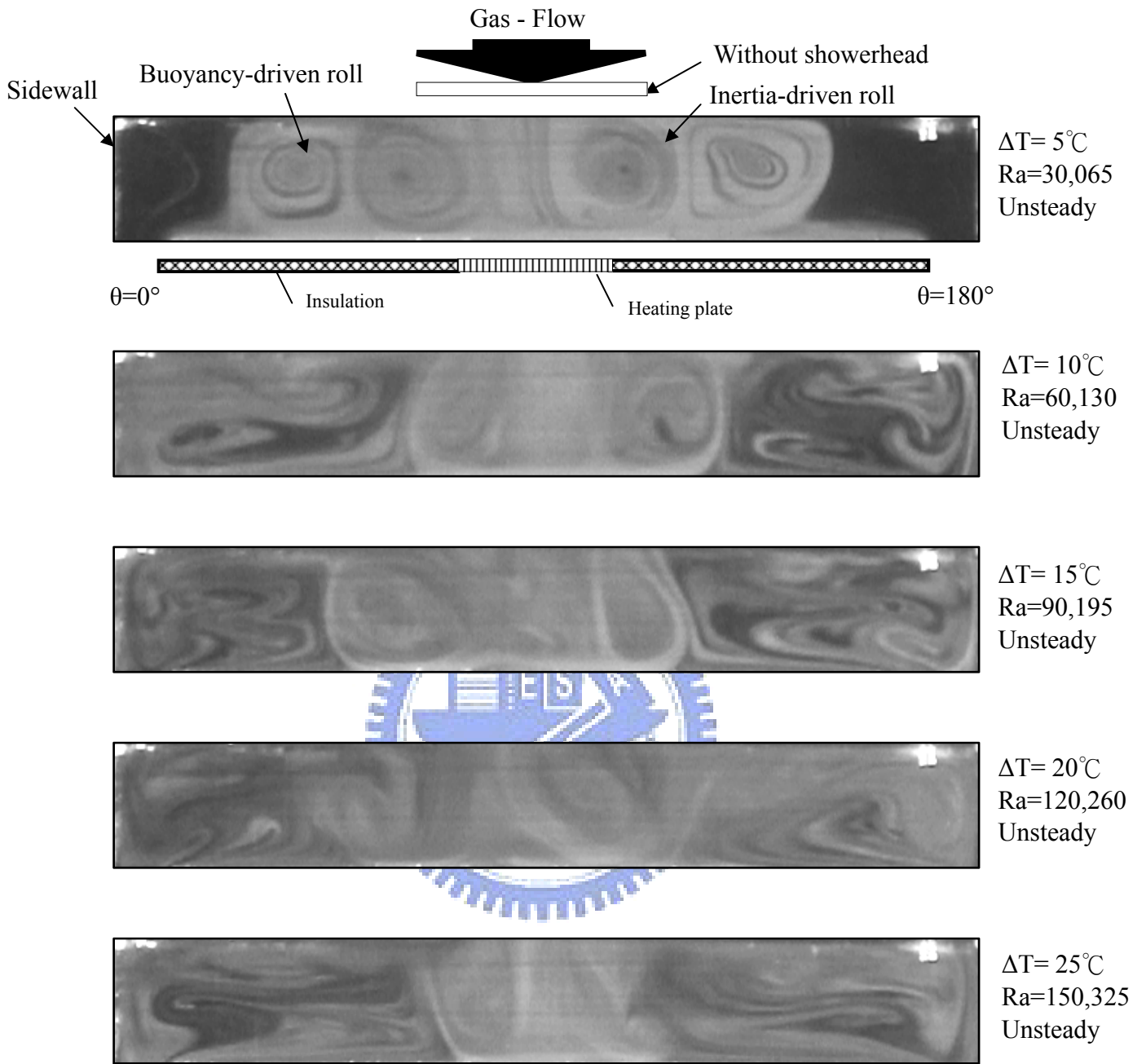
(a) Vortex flow without showerhead installation

Fig. 4.51   Side view flow photos taken at the cross plane θ = 0° & 180° for various ΔT at Q_j = 2 slpm (Re_n = 35, Re_j = 11) and H = 40.0 mm.

Gas - Flow

Sidewall

Buoyancy-driven roll

Showerhead

ΔT= 5℃
Ra=30,065
Steady

θ=0°　　Insulation　　Heating plate　　θ=180°

ΔT= 10℃
Ra=60,130
Steady

Buoyancy-driven roll

ΔT= 15℃
Ra=90,195
Steady

ΔT= 20℃
Ra=120,260
Steady

Buoyancy-driven roll

ΔT= 25℃
Ra=150,325
Steady
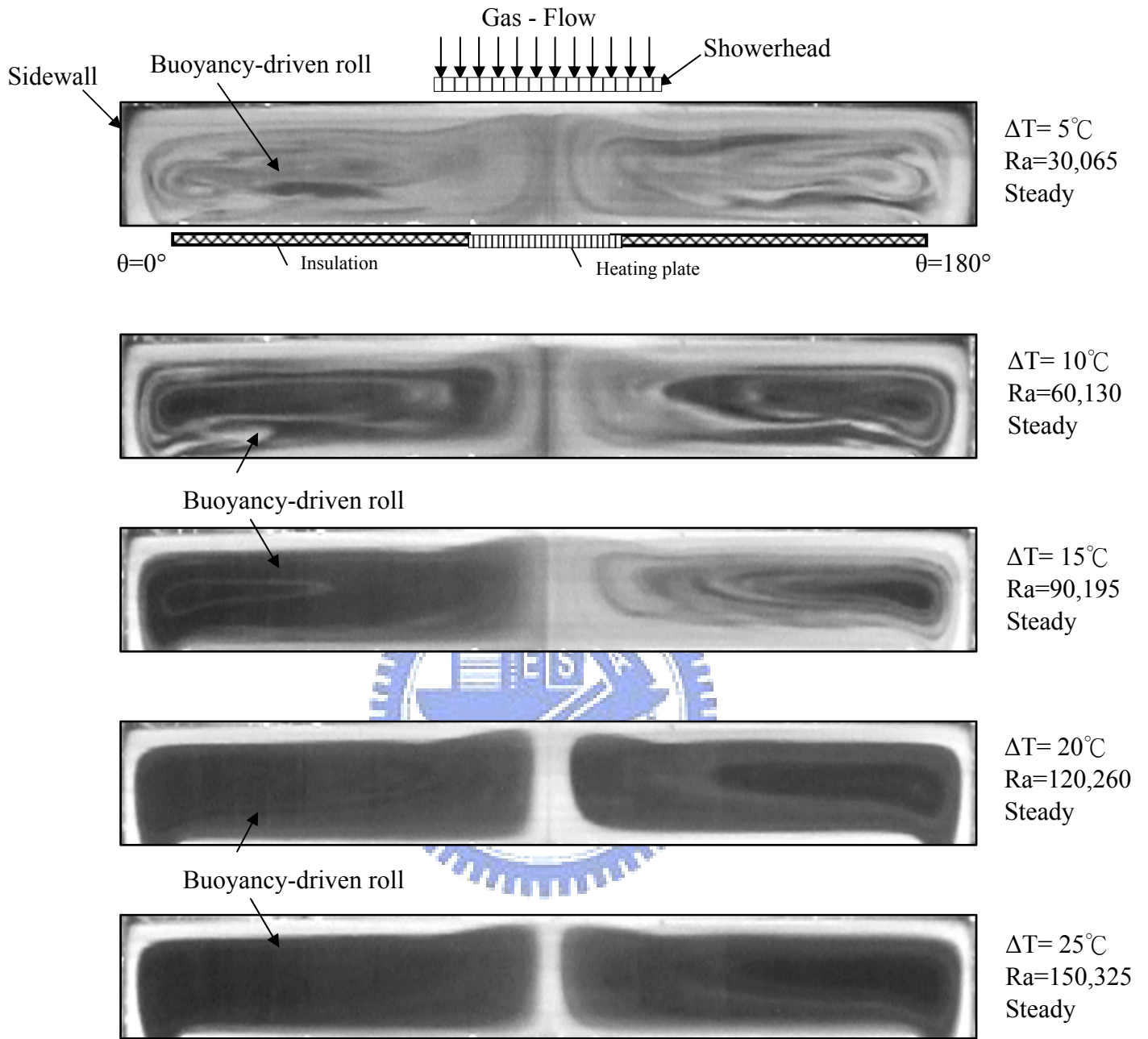
(b) Vortex flow with showerhead installation

Fig. 4.51　Continued.

Gas - Flow

Sidewall   Buoyancy-driven roll   Without showerhead   Inertia-driven roll

$\theta=0°$ Insulation   Heating plate $\theta=180°$

$\Delta T= 5℃$
Ra=30,065
Unsteady

$\Delta T= 10℃$
Ra=60,130
Unsteady

$\Delta T= 15℃$
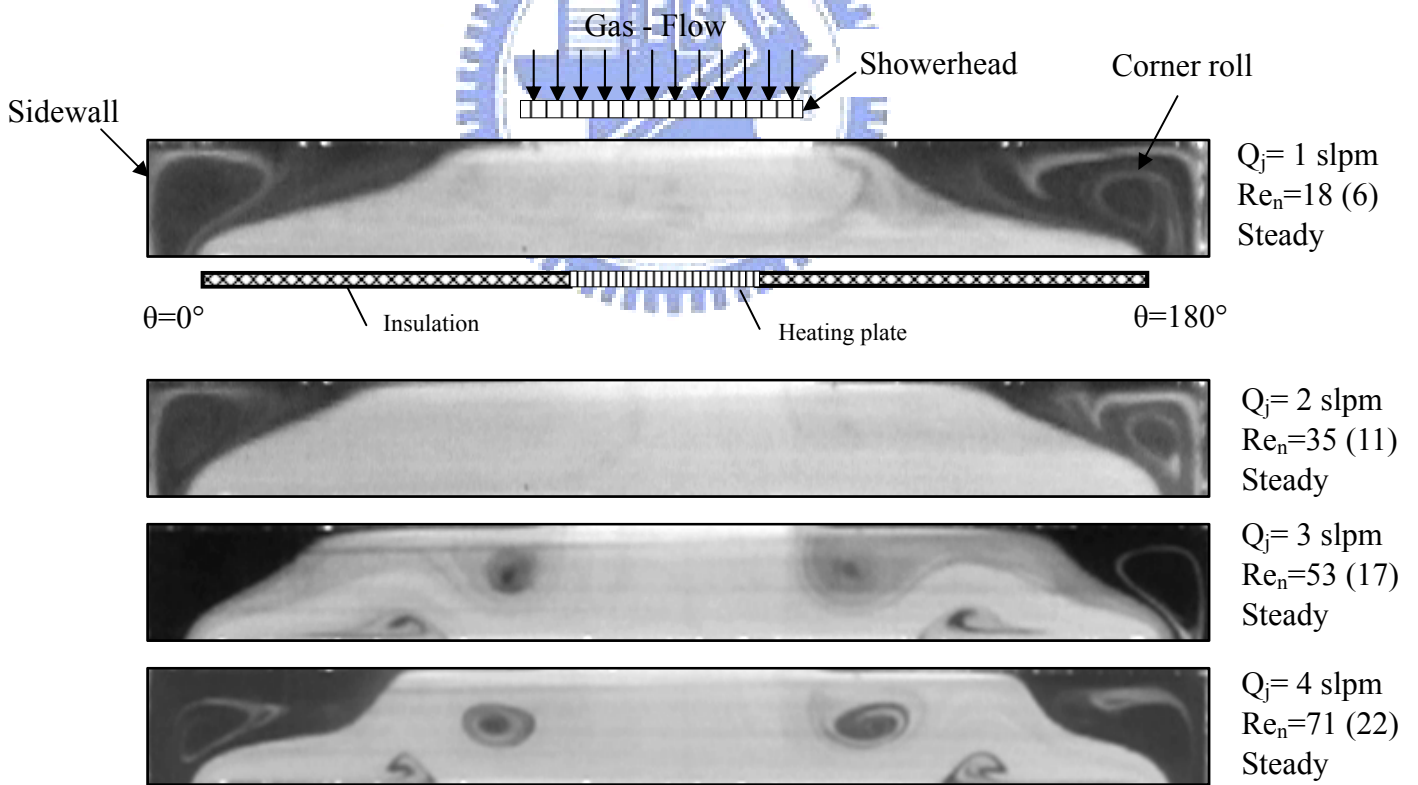Ra=90,195
Unsteady

$\Delta T= 20℃$
Ra=120,260
Unsteady

(a) Vortex flow without showerhead installation
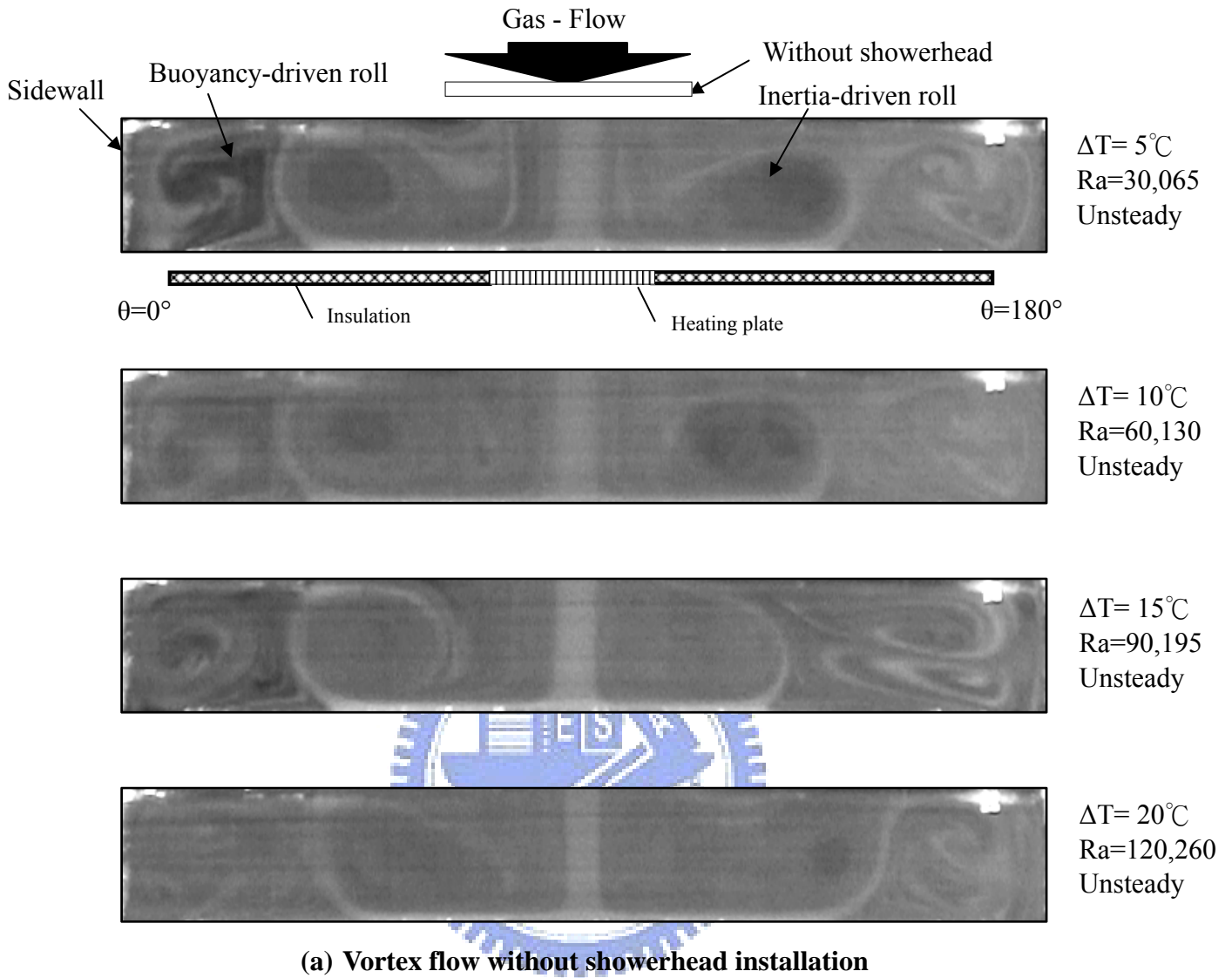
Fig. 4.52   Side view flow photos taken at the cross plane $\theta = 0°$ & $180°$ for various ΔT at $Q_j =$ 4 slpm ($Re_n = 71$, $Re_j = 22$) and H = 40.0 mm.

Gas - Flow

Sidewall   Buoyancy-driven roll   Showerhead   Inertia-driven roll

θ=0°   Insulation   Heating plate   θ=180°

ΔT= 5℃
Ra=30,065
Steady

ΔT= 10℃
Ra=60,130
Steady

Buoyancy-driven roll   Inertia-driven roll

ΔT= 15℃
Ra=90,195
Steady

ΔT= 20℃
Ra=120,260
Unsteady

Buoyancy-driven roll   Inertia-driven roll
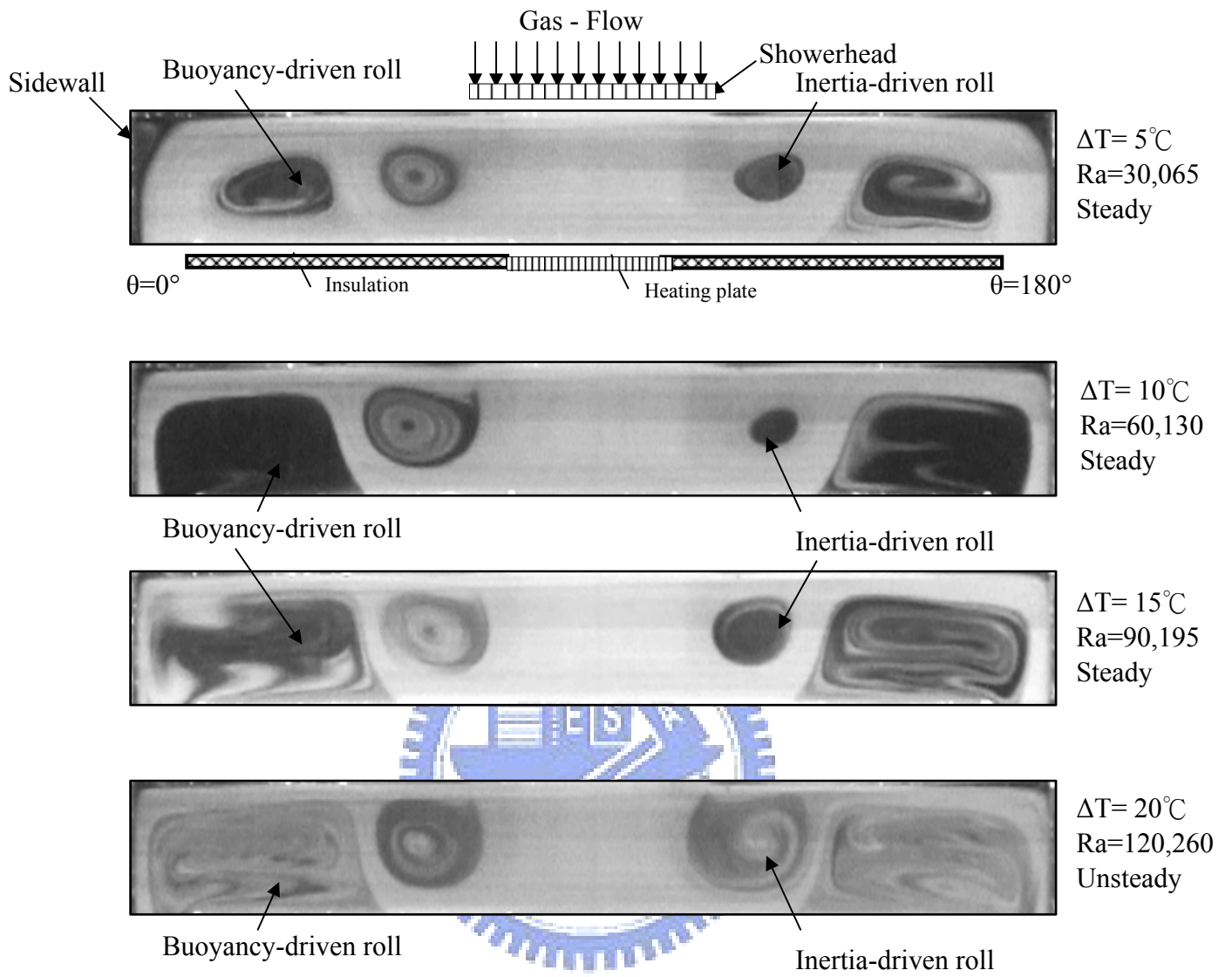
(b) Vortex flow with showerhead installation

Fig. 4.52   Continued.

CHAPTER 5

CONCLUDING REMARKS

AND RECOMMENDATIONS FOR FUTURE WORK

5.1 Concluding Remarks

Experimental flow visualization is conducted in the present study to explore how the showerhead installation affects the vortex flow resulting from a large number of tiny multiple-air jets impinging onto a heated horizontal circular disk confined in a vertical cylindrical chamber. Particular attention is paid to examining the effects of the showerhead on the onsets and characteristics of the inertia- and buoyancy-driven vortex flows. In this experiment the jet-disk separation distance is varied from 20.0 to 40.0 mm, the overall jet Reynolds number from 0 to 89, the jet Reynolds number from 0 to 28, and the Rayleigh number from 0 to 150,325. The major results obtained in the present study can be briefly summarized in the following:

1. For HD_n raised from 0.26 to 0.52 with the disk unheated (Ra=0) the critical Re_j for the onset of the primary and secondary inertia-driven roll is delayed by the showerhead installation.

2. For HD_n = 0.26 to 0.52 the plug flow only occurs at very small Re_j with the disk unheated.

3. The buoyancy-driven roll always appears for HD_n = 0.39 to 0.52 even at a small ΔT of $1℃$.

4. For HD_n = 0.26 to 0.52 with the heated disk at low Re_j, the flow pattern is dominated by the buoyancy force. There is a big buoyancy-driven circular roll in the chamber.

5. For $HD_n = 0.26$ to 0.52 with the heated disk at high Re_j, the flow pattern is dominated by the primary inertia-driven roll and buoyancy-driven roll. The critical Re_j for the onset of primary roll with various ΔT is delayed through the installation of the showerhead.

6. In the steady vortex flow with the disk unheated, the primary, secondary, and corner rolls all grow with HD_n. But the secondary roll becomes smaller for $HD_n = 0.52$.

7. In the steady vortex flow with the disk heated, both the primary inertia-driven roll and the buoyancy-driven roll get larger at increasing HD_n, squeezing out the space available for the secondary inertia-driven roll to appear.

8. In the unsteady vortex flow with disk heated for $HD_n = 0.26$, the buoyancy-driven rolls induced in the core region of the chamber experience merging and splitting before the primary-inertia driven roll appears.

9. In the unsteady vortex flow with the disk heated for $HD_n = 0.39$ and 0.52, we have time periodic flow in the chamber after the primary inertia-driven roll appears.

10. Flow regime maps delineating the vortex flow patterns and temporal state of the flow are provided. Correlation equations for the boundaries separating different flow regimes are proposed.

11. The showerhead installation at the injection nozzle can effectively suppress the inertia-driven vortex rolls.

12. The critical Re_j for the onset of the inertia-driven rolls without the showerhead installation appears earlier than that with showerhead for the disk unheated ($Ra=0$).

5.2 Recommendations for Future Work

During the course of this investigation it is realized that the overall and jet Reynolds numbers, Rayleigh number and jet-to-disk separation distance can exhibit significant influences on the vortex flow structure. The present study only covers limited ranges of these parameters. More works need to be done. A summary of the possible future work is given in the following:

1. The effects of the hole diameter and pitch on the vortex flow need to be investigated so that we can clearly understand how the jet to jet distance affects the flow pattern in the chamber.

2. The buoyancy-driven vortex flow appearing in the chamber may be suppressed by reducing the HD_n associated with lower Rayleigh number and increasing the volume flow rate.

3. Is it possible to wipe out the vortex flow in the CVD chamber at atmospheric pressure of the normal? If we install the injection nozzle with a suitable showerhead and incline the top of the chamber or rotation the susceptor, we may be able to have plug flow in the chamber.
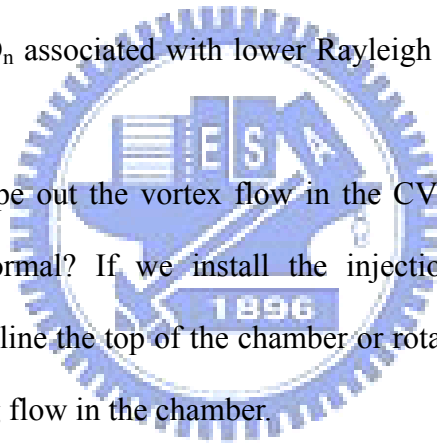
Reference

1. J. R. Guarino and V. P. Manno, Characterization of laminar jet impingement cooling in portable computer applications, IEEE Transactions on Components and Packaging Technologies 25 (2002) 337-346.

2. Klavs F. Jensen, Erik O. Einset and Dimitrios I. Fotiadis, Flow Phenomena in Chemical Vapor Deposition of Thin Films, Annu. Rev. Fluid Mech. 23 (1991) 19~232.

3. J. C. Hsieh, Experimental study of mixed convective vortex flow structure in a low speed air impinging on a heated disk in a vertical cylindrical chamber, Ph. D , Thesis ,National Chiao Tung Univ,Hsinchu,Taiwan,R.O.C.2004.

4. C. R. Biber, C. A. Wang, S. Motakef, Flow regime map and deposition rate uniformity in vertical rotating disk OMVPE reactors, Journal of Crystal Growth 123 (1992) 545-554.

5. K. J. McNaughton, C. G. Sinclair, Submerged jets in short cylindrical flow vessels, J. Fluid Mech., 25 (1966) 367-375.

6. Frnank. P. Incropera, Liquid cooling of electronic devices by single-phase convection, John Wiley & Sons, Inc, New York, 1999 (Chapter 2).

7. S. Polat, B. Huang, A.S. Mujumdar, and W.J.M. Douglas, Numerical flow and heat transfer under impinging jets: a review, in C. L. Tien and T. C. Chawla(eds.), Annular Review of Numerical Fluid Mechanics and Heat Transfer 2, pp.157-197, Hemisphere, Washington, D. C. (1989).

8. K. Jambunathan, E. Lai, M. A. Moss and B. L. Button, A review of heat transfer data for single circular jet impingement, Int. J. Heat and fluid Flow 13 (1992) 106-115.

9. R. Viskanta, Heat transfer to impinging isothermal gas and flame jets, Experimental Thermal and Fluid Science, 6 (1993) 111-134.

10. A.I. Behbahani, P.J. Disimile, S. Aydore, Flow visualization in an impinging circular air jet heat transfer measurements, ASME. HTD 112 (1989) 143-148.

11. C. O. Popiel and O. Trass, Visualization of a free and impinging round jet, Experimental Thermal and Fluid Science 4 (1991) 253-264.

12. J. A. Fitzgerald and S. V. Garimella, A study of the flow field of a confined and submerged impinging jet, International Journal of Heat and Mass Transfer 41 (1998) 1025-1034.

13. G. K. Morris, and S.V. Garimella, Orifice and impingement flow fields in confined jet impingement, J. Electronic Packaging 120 (1998) 68-72.

14. G. K. Morris, S. V. Garimella and J. A. Fitizgerald, Flow-field prediction in submerged and confined jet impingement using the Reynolds Stress Model, J. Electronic Packaging 121 (1999) 255-262.

15. J. C. Hsieh, T. C. Cheng and T. F. Lin, Characteristics of vortex flow in a low speed air jet impinging onto a heated disk in a vertical cylindrical chamber, International Journal of Heat and Mass Transfer 46 (2003) 4639-4656.

16. H. S. Law and J. H. Masliyah, Mass transfer due to a confined laminar impinging axisymmetric jet, Int. Eng. Chem. Fundam. 23 (1984) 446-454.

17. D. Sahoo and M. A. R. Sharif, Numerical modeling of slot-jet impingement cooling of a constant heat flux surface confined by a parallel wall, International Journal of Thermal Sciences 43 (2004) 877-887.

18. J. C. Hsieh and T. F. Lin, Effects of jet-to-disk separation distance on the characteristics of mixed convective vortex flow in an impinging air jet confined in a cylindrical chamber, International Journal of Heat and Mass Transfer 48

(2005) 511-525.

19. V. A. Chiriac and A. Ortega, A numerical study of the unsteady flow and heat transfer in a transitional confined slot jet impinging on an isothermal surface, International Journal of Heat and Mass Transfer 45 (2002) 1237-1248.

20. H. V. Santen, C. R. Kleijn and H. E. A. Van Den Akker, Mixed convection in radial flow between horizontal plates- I. Numerical simulations, International Journal of Heat and Mass Transfer 43 (2000) 1523-1535.

21. H. V. Santen, C. R. Kleijn and H. E. A. Van Den Akker, Mixed convection in radial flow between horizontal plates- II. Experiments, International Journal of Heat and Mass Transfer 43 (2000) 1537-1546.

22. Y. M. Chung and K. H. Luo, Unsteady heat transfer analysis of an impinging jet, ASME Transac. C, J. Heat Transfer 124 (2002) 1039-1048.

23. H. J. Poh, K. Kumar, and A. S. Mujumdar, Heat transfer from a pulsed laminar impinging jet, International Communicatios in Heat and Mass Transfer 32 (2005) 1317-1324.

24. J. C. Hsieh, C. W. Cheng and T. F. Lin, Suppression of buoyancy-driven vortex flow resulting from a low speed jet impinging onto a heated disk in a vertical cylinder by cylinder top tilting, International Journal of Heat and Mass Transfer 47 (2004) 3031-3045.

25. H. S. Law and J. H. Masliyah, Numerical prediction of the flow field due to a confined laminar two-dimensional submerged jet, Computers & Fluids 12 (1984) 199-215.

26. D. W. Colucci and R. Viskanta, Effect of nozzle geometry on local convective heat transfer to a confined impinging air jet, Experimental Thermal and Fluid Science 13 (1996) 71-80.

27. N. Gao and D. Ewing, Investigation of the effect of confinement on the heat transfer to round impinging jets existing a lone pipe, International J. Heat and Fluid Flow 27 (2006) 33-41.

28. V. Narayanan, J. Seyed-Yagoobi, and R. H. Page, An experimental study of fluid mechanics and heat transfer in an impinging slot jet flow, International Journal of Heat and Mass Transfer 47 (2004) 1827-1845.

29. M. Angioletti, R. M. Di Tommaso, E. Nino, and G. Ruocco, Simultaneous visualization of flow field and evaluation of local heat transfer by transitional impinging jets, International Journal of Heat and Mass Transfer 46 (2003) 1703-1713.

30. T. H. Park, H. G. Choi, J. Y. Yoo and S. J. Kim, Streamline upwind numerical simulation of two-dimensional confined impinging slot jets, International Journal of Heat and Mass Transfer 46 (2003) 251-262.

31. P. Y. Lin, Transient liquid crystal measurement of local heat transfer in a low air speed air jet impinging onto a disk in a vertical cylindrical chamber, M. S.thesis. National Sun Yat-sen University, Kaohsiung, Taiwan, R. O. C., 2004.

32. L. B. Y. Aldabbagh and I. Sezai, Numerical simulation of three-dimensional laminar multiple impinging square jets, International Journal of Heat and Fluid Flow 23 (2002) 509-518.

33. A. M. Huber and R. Viskanta, Effect of jet-jet spacing on convective heat transfer to confined impinging arrays of axisymmetric air jets, International Journal of Heat and Mass Transfer 37 (1994) 2859-2869.

34. B. R. Hollworth and R. D. Berry, Heat transfer from arrays of impinging jets with large jet-to-jet spacing, Journal of Heat Transfer 100 (1978) 352-357.

35. A. I. Behbahabi and R. J. Goldstein, Local heat transfer to staggered arrays of

impinging circular air jets, Journal of Engineering for Power 105 (1983) 354-360.

36. D. M. Kercher and W. Tabakoff, Heat transfer by a square array of round air jets impinging perpendicular to a flat surface including the effect of spent air, Journal of Engineering for Power 92 (1970) 73-82.

37. J. Y. San and M. D. Lai, Optimum jet-to-jet spacing of heat transfer for staggered arrays of impinging air jets, International Journal of Heat and Mass Transfer 44 (2001) 3997-4007.

38. F. C. Hsieh, Steady and Unstable Vortex Flow Characteristics Affected by Disk Rotation in an Air Jet Impinging onto a Confined Heated Horizontal Disk, Ph. D, Thesis, National Chiao Tung Univ,Hsinchu,Taiwan,R.O.C.2008.

39. H. V. Santen, C. R. Kleijb, H.E. A. Van Den Akker, On turbulent flows in cold-wall CVD reactors, Journal of Crystal Growth 212 (2000) 299-310.

40. H. V. Santen, C. R. Kleijb, H.E. A. Van Den Akker, Symmetry breaking in a stagnation-flow CVD reactor, Journal of Crystal Growth 212 (2000) 311-323.

41. C. Y. Soong, C. S. Jou and C. H. Chyuan, Flow visualization in an epitaxial growth CVD reactor with a rotating-disk, The 1st Pacific Symposium on Flow Visualization and Image Processing, Hononlulu (1997) 23-26.

42. C. Y. Soong, C. H. Chyuan and R. Y. Tzong, Thermo-flow structure and epitaxial uniformity in large-scale metalorganic chemical vapor deposition reactors with rotating susceptor and inlet flow control, Jpn. J. Appl. Phys. 37 (1998) 5823-5834.

43. S. P. Vanka, G. Luo, and N. G. Glumac, Parametric effects on thin film growth and uniformity in an atmospheric pressure impinging jet CVD reactor, Journal of Crystal Growth 267 (2004) 22-34.

44. S. P. Vanka, G. Luo, and N. G. Glumac, Numerical study of mixed convection flow in an impinging jet CVD reactor for atmospheric pressure deposition of thin films, ASME Transac, J. Heat Transfer 126 (2004) 764-775.

45. G. Luo, S. P. Vanka, and N. G. Glumac, Fluid flow and transport processes in a large area atmospheric pressure stagnation flow CVD reactor for deposition of thin films, Int. J. Heat Mass Transfer 18 (2004) 4979-4994.

46. D. I. Fotiadis, A. M. Kremer, D. R. Mckenna and K. F. Jensen, Complex flow phenomena in vertical MOCVD reactors: effects on deposition uniformity and interface abruptness, Journal of Crystal Growth 85 (1987) 154-164.

47. D. I. Fotiadis, S. Kieda and K. F. Jensen, Transport phenomena in vertical reactor for metalorganic vapor phase epitaxy I. Effects of heat transfer characteristics, reactor geometry, and operating conditions, Journal of Crystal Growth 102 (1990) 441-470.

48. Prasad N. Gadgil, Optimization of a stagnation point flow reactor design for metalorganic chemical vapor deposition by flow visualization, Journal of Crystal Growth 134 (1993) 302-312.

49. Prasad N. Gadgil, Single wafer processing in stagnation point flow CVD reactor : prospect, constraints and reactor design, Journal of electronic materials 22 (1993) 171-177.

50. B. Phillips, R. G. Rodriguez, L. D. Lau, and S. D. Steidley, Effect of showerhead configuration on coherent Raman spectroscopically monitored pulsed radio frequency plasma enhanced chemical vapor deposited silicon nitride thin film, plasma chemistry and plasma processing 24 (2004) 307-323.

51. S. J. Kline and F. A. McClintock, Describing Uncertainties in Single-Sample Experiment, Mechanical Engineering 75 (1953) 3-8.

52. R. J. Moffat, Contributions to the Theory of Single-Sample Uncertainty Analysis, ASME Transac, J. Fluids Engineering 104 (1982) 250-260.